A comparative study between the simulated and measured cathodoluminescence generated in ZnS phosphor powder

By

Sheng-Hui Chen

A thesis submitted in fulfillment of the requirement for the degree

Magister Scientiae

in the
Faculty of Natural and Agricultural Sciences
Department of Physics
at the
University of the Free State
Republic of South Africa

Study leader: Dr. A.P. Greeff
Co-study leader: Prof. H.C. Swart
Date: 13 August 2003

Acknowledgements:

I deeply appreciate the following people:

- My entire family for their support and understanding throughout the duration of my study.
- The National Research Foundation (NRF) for the financial assistance.
- My study leader Dr. A.P. Greeff for his teaching, professional leadership, proof reading and editing.
- Prof. H.C Swart, my co-study leader, for his professional suggestions and wisdom.
- Dr. K.T. Hillie for his kind explanations when I faced difficulties.
- Mr. O.M. Ntwaeaborwa for spending his time with me during the experiments and proof reading and editing.
- And lastly, to all the Physics Department staff who have helped and assisted me during my study.

Summary

In the past few decades cathode ray tubes (CRTs) have dominated the display market because of their excellent image quality, ease and economy of manufacture. However their bulky packaging and high power consumption make them unsuitable for portable electronic devices.

Field emission displays (FEDs) show the most potential amongst all other types of flat panel displays (FPDs). These FEDs have several advantages over the FPD market, which is currently dominated by active matrix liquid crystal displays (AMLCDs) and plasma displays (PDPs). FEDs generate their own light by a process referred to as cathodoluminescence (CL) in which phosphor powders inside the screen are excited in a similar manner to those used in CRTs. However, in contrast to CRTs, the accelerating voltage of electrons in FEDs is lowered in order to reduce the bulky packaging and the power consumption. Electrons with the reduced accelerating voltage have a shallower penetration depth and therefore the surface condition of the phosphor powder is critical in order to ensure proper functioning of the display.

During the prolonged exposure of the phosphors to an electron beam, the phosphor surface is oxidised to form a non-luminescent layer. This electron stimulated oxide formation is due a chemical reaction between the phosphor and the residual gases in the sealed vacuum, e.g. oxygen and water vapour. Since the CL is dependent upon the energy loss of electrons in the phosphors, the CL decreases with the growth of the oxide layer on the phosphor surface. For high acceleration voltages, this oxide layer has little effect on the brightness of the CL, but as the accelerating voltage decreases as for FEDs, the layer has a much more profound effect.

The ZnS:Cu,Al,Au (P22G) is a standard green phosphor commonly found in CRTs. In this study the P22G phosphor powder was bombarded by an electron beam in an oxygen ambient, argon ambient and other mixture of gases. These mixtures consisted of varying concentrations of oxygen, carbon monoxide and argon gas. Auger electron

spectroscopy (AES) and cathodoluminescence spectroscopy were used to monitor changes in surface composition and luminescent properties of the P22G phosphor during electron bombardment.

When the P22G phosphor powder was exposed to an electron beam in water-rich oxygen gas, a chemically-limited ZnO layer was formed on the surface. The CL intensity generated from carbon free P22G phosphor decreased linearly with the thickness of the ZnO layer. The experimentally measured thickness of the ZnO layer agrees very well with the calculated value of the theoretical simulation. The theoretical simulation of electron trajectories into the ZnO/ZnS powders was based on a Monte Carlo simulation and the CL intensity was quantified from the electron energy loss profile generated during the simulation. According to the results of the simulation, the effect of a ZnO layer on the CL is minimised by the use of a high energy electron beam at a low incident angle.

The electron exposure of P22G phosphor powder was also performed in dry oxygen gas. A layer of $ZnSO_4$ was formed on the surface after electron exposure. The sulphate formation decayed exponentially with time and it is postulated that this was due to the diffusion of the charge reactants through the sulfate film to reaction interfaces. The P22G phosphor exposed to the electron beam in argon gas and gas mixtures degraded more slowly than in oxygen gas. Argon gas and carbon monoxide gas may suppress the degradation of the P22G phosphor powder.

Keywords

Phosphor: A wide band gap semiconductor that is intentionally doped with impurities to emit the desired frequency of light.

Cathodoluminescence: The phenomenon of the emission of light from phosphors by electron beam irradiation.

Monte Carlo simulation: A powerful simulation technique frequently used to emulate real-world phenomena that can be properly described statistically by probability density functions and random number generators.

Phosphor degradation: Reduction of the efficiency of a phosphor material through

prolonged electron bombardment.

Contents

Chapter 1

A background to current display technologies

The global display market reached a value of over $51 billion in 2000 and it is expected to grow to almost $100 billion by 2005. Flat panel displays (FPDs) currently comprise about 45 percent of the total display market, with $24 billion in 2000, and an expected growth to $70 billion in 2005. From these projections, it is evident that FPD market is a fast growing segment for display technologies [1]. In this chapter a background to current display technologies are given.

1.1 Current display technology

In the 20th century cathode ray tube (CRT) displays were the most important component used in home entertainment. In the 21st century FPDs will continue to play an important role in our daily life. In the following paragraphs a brief description of the conventional CRT and some of the modern FPDs are given.

1.1.1 Conventional display technology

Televisions and computer monitors rely on a device known as a cathode ray tube (CRT) to display an image on its screen. A CRT is a specialised vacuum tube that produces images when an electron beam strikes a screen coated with phosphor powders. Phosphor powders are classified as a semiconductor material in which electrons are excited from the valence band (VB) to the conduction band (CB) when an energetic electron beam strikes them. The excited electron in the unstable conduction band eventually falls back to the valence band and emits a photon in the process. The method in which CRTs produce light is called cathodoluminescence (CL). The basic principle of CL is discussed in detail in Section 2.1.

A cathode ray tube consists of several basic components, as illustrated in Figure 1.1.

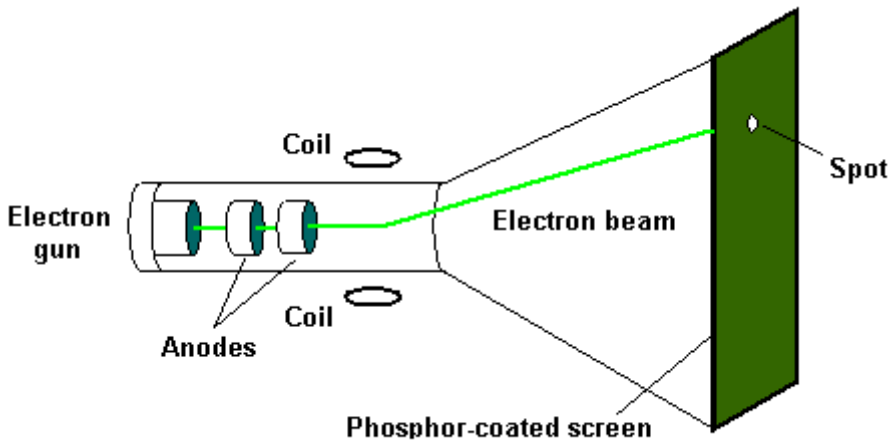

Figure 1.1: A diagram illustrating the basic components of a CRT. Illustration courtesy of [2].

The electron gun generates a narrow, focused beam of electrons which are accelerated by the set of anodes. Two sets of deflecting coils produce an electromagnetic field that allows for horizontal and vertical deflection of the electron beam. Through the CL process the electron beam produces a tiny, bright visible spot when it strikes the phosphor coated screen.

To produce an image on the screen, complex signals are applied to the deflecting coils and also to the apparatus that controls the intensity of the electron beam. High electron beam intensities generate high CL or light intensities. The complex signals scan the spot across the screen with varying brightness in a sequence of horizontal lines resulting in a monochromatic image.

However, virtually all modern CRTs today offer full colour images. Instead of one electron gun, a full colour image is achieved by three electron guns – one each for red, green and blue phosphors that is arranged as small dots on the screen. Behind the phosphor-coated screen there is also a thin perforated metal screen called a shadow mask. The small holes are aligned with the phosphor dots to ensure that the electron beam for each colour strikes only those dots intended for use for that colour on the screen as illustrated in Figure 1.2.

For example, when a CRT needs to create a red dot, the electron gun associated with the red colour fires a beam at the red phosphor. The same applies for the generation of blue and green dots. To create a white dot, red, green and blue beams are fired

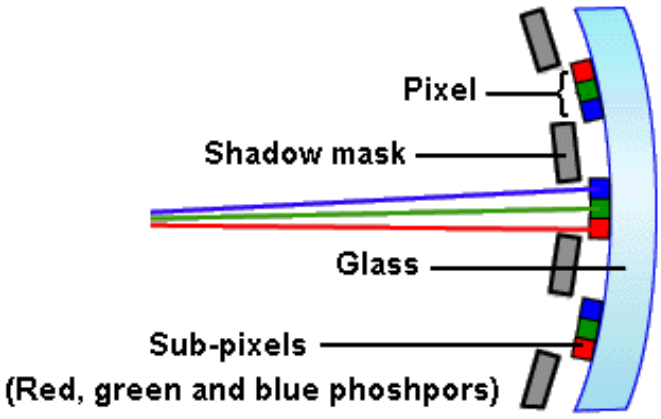

Figure 1.2: A diagram showing the shadow mask in CRTs. Illustration courtesy of [3].

simultaneously at similar intensities. To create a black dot, all three beams are turned off as they scan past the dot. All the other colours on the screen are combinations of different intensities of red, green and blue. Thus, each full colour image on a CRT is produced by three overlapping images: one in red, one in green and one in blue.

1.1.2 Modern flat panel display technologies

Although CRTs have been popular for many years, their main disadvantages are their high power consumption and large footprint. As the display increases in size, the depth of the CRT also increases. For more than thirty years the display industry has attempted to create a thin, flat, low power version of the highly successful cathode ray tube. Therefore FPDs are becoming increasingly popular in today's commercial electronic devices and have widespread use in products such as cellular phones, personal digital assistants (PDAs), video recorders, and notebook PCs. In the following section an overview of the currently available FEDs is given.

1.1.2.1 Liquid crystal displays (LCDs)

Liquid crystal is neither solid nor liquid and was discovered by an Austrian botanist, Fredreich Rheinizer in 1888. In the mid-1960s, scientists showed that liquid crystals could change the properties of light passing through the crystals when stimulated by an external electrical charge.

Liquid crystal acts either as a solid or liquid, depending on the conditions. This is also

the reason for its contradictory name. At any time liquid crystals can be in one of several distinct phases where the nematic phase is responsible for LCD working. A particular sort of nematic liquid crystal, called twisted nematics is in a naturally twisted state. When an electric current is applied, these liquid crystals untwist to varying degrees, depending on the voltage. LCDs use these crystals because they react predictably to an electric current in such a way that it successfully controls the passage of light.

LCDs come in two variants: passive and active matrix. The passive matrix LCD consists of a layer of liquid crystal materials sandwiched between two glass plates. On the inner surfaces of the glass plates there are transparent electrodes coated with a polymer resulting in the liquid crystal material adjacent to one surface lying perpendicular to the liquid crystal material at the other surface. Across the thin film of liquid crystal, the molecules are twisted by 90°. On the outer surface of the glass plates, polarisers are placed so that they are parallel to the liquid crystal orientation and perpendicular to each other. When no voltage is applied to the liquid crystals, light entering the front polariser is guided by the liquid crystal layer and twisted towards the rear polariser, through which it is transmitted. The light is then reflected back to the viewer by a reflector situated underneath the bottom glass plates. When a voltage is applied, the liquid crystals are untwisted and light transmitted through the front polariser is blocked by the rear polariser, forming a dark image as shown in Figure 1.3. The passive matrix LCD is widely used in watches and calculator displays.

The active matrix type is used in full colour notebook displays. The active matrix liquid crystal display (AMLCD) is constructed in a similar way to the passive matrix, except for an additional plane between the transparent electrodes. This plane consists of thin film transistors (TFTs) located at each pixel to control the pixel's on-off state in the case of monochrome displays. In full colour display there are three TFTs per pixel. For example, a 640×480 colour VGA screen requires 921,600 transistors. Figure 1.4 illustrates the construction of an active matrix LCD.

Unlike CRTS, LCDs are non-emissive displays. Therefore these displays need a reflector (in passive matrix LCDs) or external backlight (in active matrix LCDs) to clearly display an image. In the case of AMLCDs the backlight could be a metal

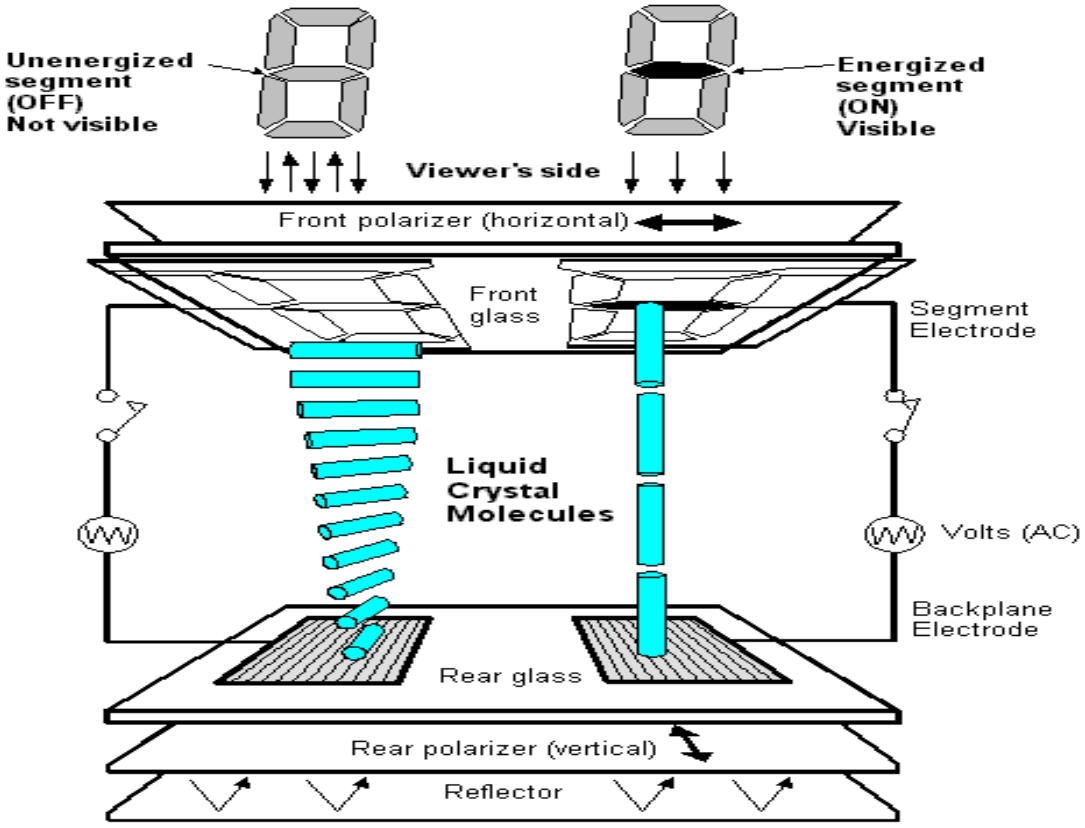

Figure 1.3: A diagram showing the construction of the passive matrix LCD.

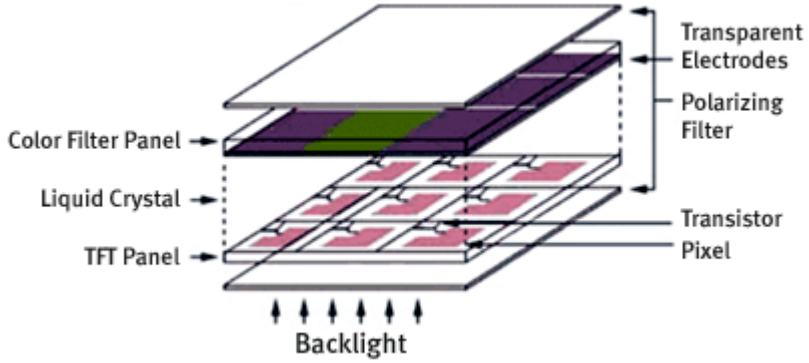

Figure 1.4: A diagram showing the construction of an AMLCD. Illustration courtesy of [4].

halide, a fluorescent or halogen bulb. For instance, the red sub-pixel is on, the backlight is guided by the liquid crystals and passes through the red colour filter resulting the output of red light. Through the variation of the voltage applied, the intensity of each sub-pixel can range over 256 shades. By combining different intensities of red, green and blue light, all the other colours on the screen can be generated.

Due to the large amount of transistors in AMLCDs the electronic driving circuits needed to address each pixel are quite complicated and have a slow response time. The other drawback is the narrow viewing angle due to the complicated design.

1.1.2.2 Electroluminescent displays (ELDs)

ELD is another modern flat panel display technology and is classified as an emissive display, unlike liquid crystal displays. Electroluminescence (EL) is the process used to generate light in ELDs and is similar to CL. The difference between EL and CL is the source of electrons used to excite the phosphor powders. In CL electrons originate from an electron gun, but in EL electrons are generated by a voltage difference between electrodes. The phosphor powders used in ELD are the same as those used in CRTs. In Figure 1.5 the construction of an ELD is shown.

The luminescent phosphor layer is sandwiched between transparent dielectric layers with a matrix of row and column electrodes at the back of the glass substrate. A circuit

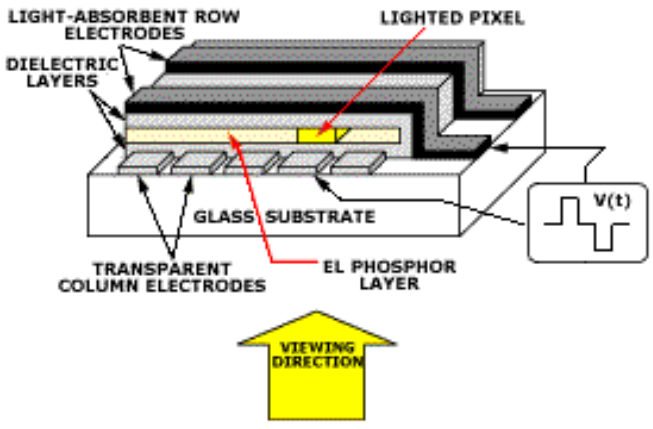

Figure 1.5: A diagram showing the construction of an ELD. Illustration courtesy of [5].

board containing the drive and control electronics is connected to the back of the glass substrate as well. To drive the display a voltage is applied to the electrodes causing electrons to accelerate in the area of intersection and a pixel to emit light from the phosphor powders.

ELDs have a few advantages over other display technologies, such as having wider viewing angles than LCDs, and also offering a more efficient packaging than CRTs. However ELDs are not a popular choice for displays due to their inefficient colour capabilities and high cost associated with their electronic driving circuits.

1.1.2.3 Plasma displays (PDPs)

Plasma display is the latest flat panel display technology. It consists of an array of closed cells, referred to as pixels, which are composed of three sub-pixels. These three sub-pixels are coated by green, red and blue phosphors respectively. The construction is shown in Figure 1.6.

In PDPs each cell is filled with xenon or neon gas and the front and rear glass plates are covered by electrodes. When a voltage is applied to the electrodes, accelerated electrons collide with the gas atoms in the cells. These gas atoms lose their electrons and form a plasma. These unstable excited positive gas atoms then combine with electrons and release invisible ultraviolet light photons. Ultimately, these ultraviolet photons excite the phosphor powder coated on the inside of the cells by a process

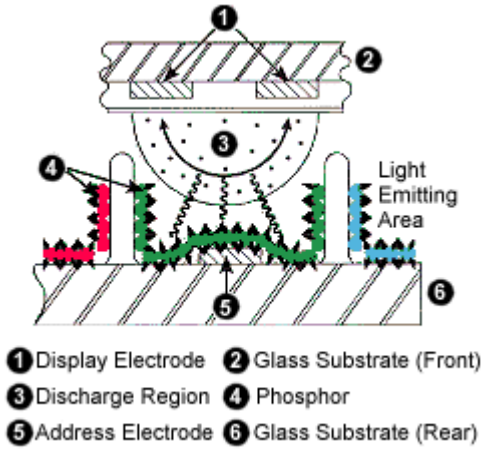

Figure 1.6: The construction of a plasma display. Illustration of courtesy of [6].

called photoluminescence (PL). In this process ultraviolet photons excite electrons from the VB to the CB and produce visible light when electrons fall back from the CB to the VB. The phosphor powders used in the cells are the same types that are used in CRT displays.

By varying the pulses of current flowing through the different cells, the control system can increase or decrease the intensity of each sub-pixel colour to create different combinations of red, green and blue light. Just as in CRT, the plasma display varies the intensities of the different monochromatic colours to produce a full range of colours.

In PDPs a large flat screen can easily be produced. Since PDPs do not use electron beams, as conventional CRT displays do, they are immune to the effects of magnetic fields. Components such as loudspeakers that contain strong magnets can distort the picture if placed too close to a CRT screen. Plasma displays can be placed in close proximity to any type of loudspeaker and not experience any image distortion. Another advantage of the plasma display is that it offers a very wide viewing angle compared to LCD. The PDP market is aimed at large area home (> 40 inch diagonal) entertainment and commercial display systems. The image quality of the plasma displays is not quite up to the standards of CRT displays, but they are satisfactory to most consumers.

1.1.2.4 Field emission displays (FEDs)

Although their use is still limited, FEDs will probably be the most popular FPD technology of the future, combining the best properties of CRTs and FPDs. FEDs are also classified as emissive displays and operate on a similar principle to CRTs. Like CRTs, FEDs also generate light by cathodoluminescence, but instead of an electron gun, FEDs use a matrix-addressed array of about 4000 cone shaped micro-tips per pixel to emit electrons [7]. This field emission array is placed in close proximity (0.2-2mm) to the phosphor face-plate. Due to the close distance between the micro-tips and the phosphor screen, as well as the absence of deflecting coils, the need for a bulky vacuum tube is eliminated. Since electrons are emitted by the cold cathode process the power consumption is also decreased considerably. In Figure 1.7

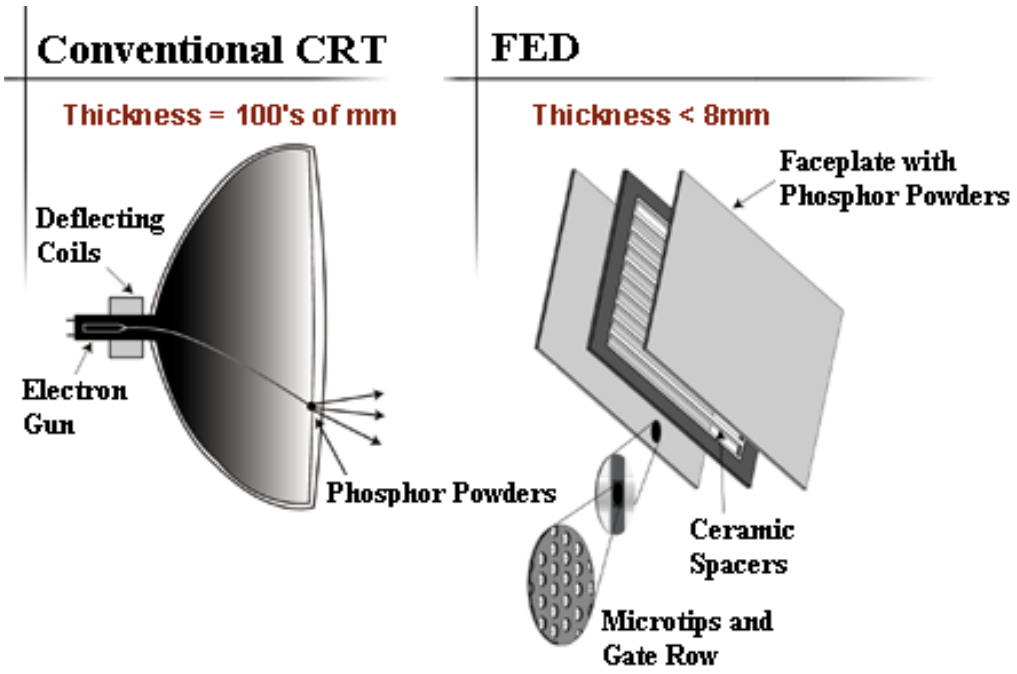

Figure 1.7: A comparison between a FED and a CRT. The drastic reduction in size for the FED is due to the use of an array of micro-tips as the cathode instead of the traditional electron guns as found in CRTs. Illustration courtesy of [7].

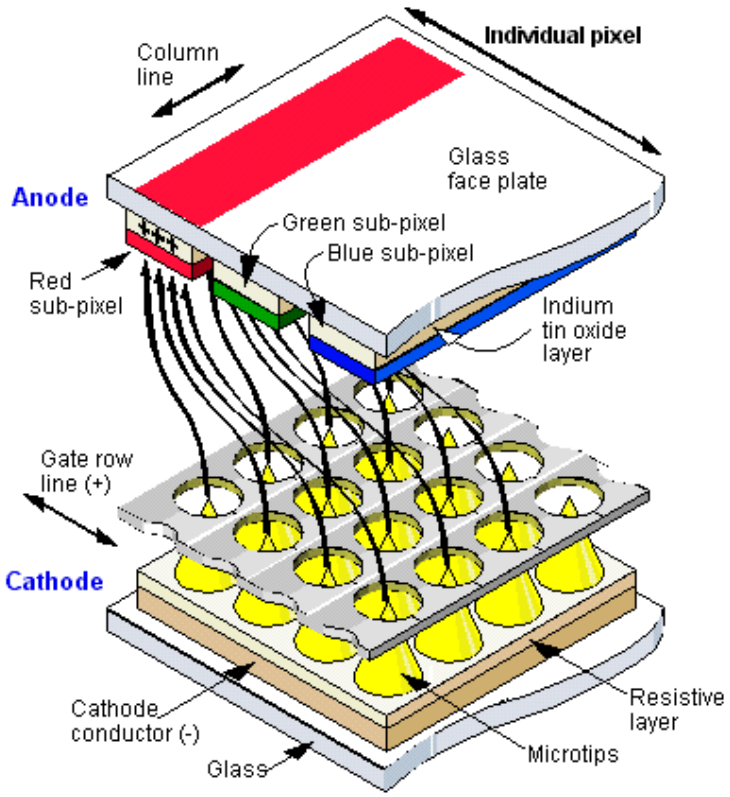

Figure 1.8: A diagram showing the construction of the FED. Illustration courtesy of [8].

an illustration is shown in which the construction of a FED is compared to that of a CRT. The ceramic spacers are used in the construction of FEDs to prevent the structure from collapsing when the volume between the face and back-plate is evacuated.

In Figure 1.8 a more detailed diagram of the FED construction is shown. Electrons from the negatively charged micro-tips are emitted when the gate row is positively charged. The electrons then flow to the phosphors that are momentarily given a larger positive charge. At each pixel there are three different colour lights emitting phosphor powders. By varying the degree of the positive charging of the phosphor powders, different amounts of electrons irradiate the phosphor powders and different intensities of red, green and blue light are generated. The desired colour is achieved from the combination of different intensities of this these primary colours.

FEDs show promise in replacing the current market leaders in FPD technology: AMLCDs and PDPs. They have a high image quality and large viewing angle like CRTs, but are lightweight and thinner. Furthermore, increased power efficiency is obtained because FEDs do not require the shadow mask as used in conventional CRTs. The shadow mask is responsible for up to 80% power wastage, since large amount of the beam current is absorbed by the mask. Also, as already mentioned, the cold cathode emission process increases the power efficiency in FEDs even further. The small form factor and low power consumption make FEDs an attractive display in battery-powered mobile applications.

1.1.3 Comparison between FEDs and other FPDs

From a marketability viewpoint, the most favorable displays must be light-weight, small in size, have low power consumption and be fair in price. According to the above-mentioned criteria, FEDs are good competitors among the different FPD technologies currently available. In Table 1.1 FEDs are compared to other display technologies on criteria such as cost, fabrication and image quality differences.

FEDs that use the same low-cost phosphor materials as ordinary CRTs are the simplest and least expensive to produce among all the current FPD technologies.

	CRT	Modern flat panel display technologies			
		AMLCD	ELD	PDP	FED
Low cost	●				●
Ease of manufacture	●				●
Wide viewing angle	●		●	●	●
Rugged			●		●
Sharpness	●			●	●
Low power		●			●
High resolution	●	●		●	●
Thin		●	●	●	●
Lightweight		●	●	●	●

Table 1.1: A comparison between the different display technologies currently available.

FEDs have a higher tolerance for defects because of the large number of redundant micro-tip emitters at each pixel. In the FED, up to 20 percent of the emitters may be defective with no affect on the image. In contrast, in AMLCDs if there is a problem with any of the transistors, it creates a bad pixel on the screen. Most AMLCDs have a few bad pixels scattered across the screen

In AMLCDs, increasing the resolution cuts down on the transmission of light coming from the screen's backlight. Turning up the backlight raises power consumption and shortens battery life. Weakening the colour filters allows more light to pass through but results in a paler image. In contrast, FEDs can easily deliver excellent 24-bit colour and high resolution images without any brightness or power trade-offs. The FEDs response time is also five times as fast as AMLCDs, enabling them to display fast-moving images without blurring. This makes them the ideal medium to use in multimedia applications.

Another advantage of FEDs is the large viewing angle extending over 160°. Images on AMLCDs become faint or invisible as the viewing angle increases above 40°. In Figure 1.9 the viewing angles of the modern commercial available displays and FEDs are compared. FEDs can also be operated in extreme environments, while some other

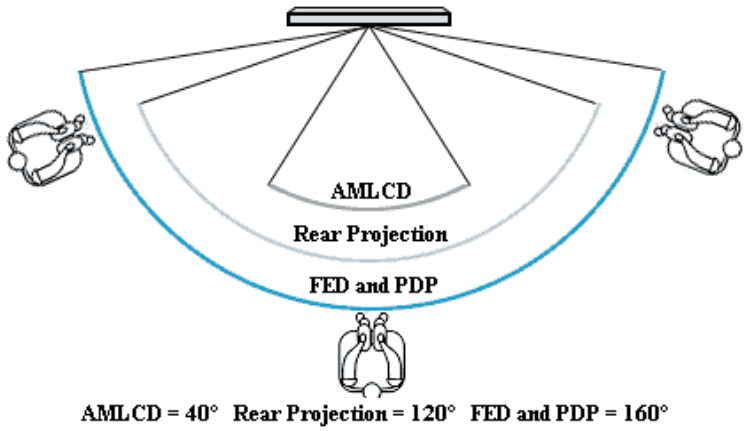

Figure 1.9: A comparison of viewing angles of different available FPDs, rear projection and. FED. Illustration courtesy [9].

FPDs have very narrow operating temperature ranges, making them impractical in very cold or hot conditions.

However, FEDs did not receive serious commercial consideration until 1985, when Robert Meyer and his team at the Laboratoire d'Electronique de Technologie et d'Instrumentation (LETI) demonstrated the first FED prototype [10]. This technological breakthrough convinced many industrial groups worldwide to invest in FED development. Presently, the French PixTech [11], Japanese based Futaba [12] and Candescent [7] are the only companies producing FEDs for commercial consumption. A full colour 12.1 inch display with a 1024×768 screen resolution was developed by PixTech for military purpose. A full colour prototype of a 13.2 inch SVGA with a 800×600 screen resolution was developed by Candescent Technologies. Futaba developed a monochromatic prototype of 5.8 inch with a 640×480 screen resolution.

Samsung Advanced Institute of Technology (SAIT), developed the worlds first 9 inch colour carbon nanotube field emission display (CNT-FED) prototype in 1999 [13]. In CNT-FED carbon nanotubes are the source of electrons instead of metal micro-tips. Production of FEDs using carbon nanotubes is expected to reduce power consumption even further, as well as lower production costs. There is a possibility that CNT-FED will also allow future substrates to be flexible, so that ultra thin screens can be rolled up or wrapped around curved surfaces.

1.2 The aim of this study

Although FEDs possess many advantages, these display are still only produced experimentally and in small commercial numbers because they are still in the research and development stage. Many of the challenges associated with producing FEDs with a desirable image quality and a competitive price were not fully appreciated. The operating lifetime of the FEDs is one of these challenges.

When the phosphor screen is exposed to prolonged electron beam irradiation, a non-luminescent oxide layer is formed on the surface of the phosphor powders. Electrons loose energy in the non-luminescent oxide layer during penetration and therefore decrease the energy loss in the phosphor bulk. Since the CL intensity is dependent upon the energy loss in the phosphor, the growth of the oxide layer significantly influences the CL intensity. In FEDs the electrons generated from the micro-tips have low energies. The fraction of energy loss in phosphor bulk therefore decreases even more. Because low energy electrons are employed, FEDs typically require 10 times more beam current than CRTs in order to have the same level of luminance. Since the phosphor life is proportional to the beam current, phosphors in FEDs age faster. As the oxide layer grows continuously during irradiation, the fraction of the electron's energy loss in the phosphor bulk decreases with a subsequent degradation in CL until all the energy loss occurs in the non-luminescent oxide layer.

In order to solve the problem of the growing oxide layer, one must first understand the oxide growing mechanism on top of the phosphor in the FED operational conditions. ZnS:Cu,Al,Cu (P22G) phosphor is a standard green phosphor. The following were investigated on P22G phosphor:

1. The effect of the water vapour on the degradation behavior in the oxygen ambient.
2. The degradation behavior in the various gas mixtures.
3. The comparison between experimental results and the Monte Carlo simulation.

1.3 The layout of the thesis

This chapter serves as a brief summary of the current display technologies and

highlights the astonishing advantages of the field emission displays. It also outlines the research carried out in this thesis.

Chapter 2 focuses on the theories involved in this study. The fundamental concepts of cathodoluminescence, the electron stimulated surface chemical reaction (ESSCR) model and the Monte Carlo simulation technique are discussed in detail.

Chapter 3 introduces the experimental instruments and AES technique used in this study. The experimental and Monte Carlo simulation procedures are also given in this chapter.

The experimental results, discussions and the comparison to the simulation result are given in Chapters 4 and 5. The thesis is concluded in Chapter 6, which also contains suggestions for future studies.

Chapter 2

Theories

In this chapter the process of cathodoluminescence (CL), principles of the degradation process of ZnS phosphors and the Monte Carlo simulation technique are discussed. The Monte Carlo method was used to simulate the electron trajectories in the phosphor powder and to determine the energy loss profile. The quantification of the CL is also discussed in this chapter.

2.1 Process of cathodoluminescence (CL)

Semiconductors include a large number of substances with widely different chemical and physical properties. Due to the wide range of properties, semiconductors are used in many kinds of electronic components, including light generation applications as is the case with phosphor powders and the cathodoluminescence process.

A typical band structure of a semiconductor is shown in Figure 2.1. The band gap of a semiconductor is small and measured in electron volt (eV). When the energy supplied to the semiconductor is larger than the energy gap, E_g, it is possible to excite electrons in the valence band (VB) to the conduction band (CB) and leave vacancies or holes in

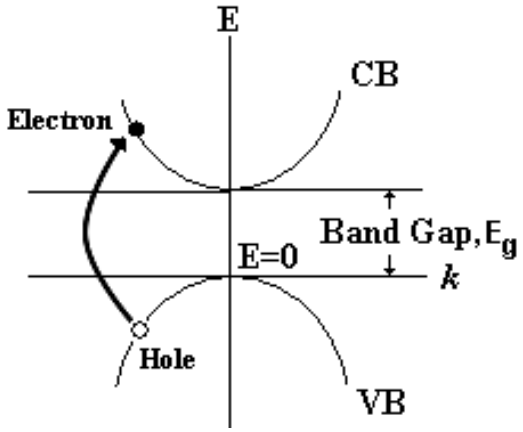

Figure 2.1: Band structure of a semiconductor.

the VB. This process is referred to as the creation of electron-hole (e-h) pairs.

When a semiconductor is doped with appropriate impurities, a sample containing either excess electrons or holes can be obtained. As an example, consider a specimen of Si which has been doped with As. The As atoms occupy some of the lattice sites formerly occupied by the Si host atoms. The distribution of the impurities is random throughout the lattice, but affects the solid in a very important aspect. The As atom is pentavalent while Si is tetravalent. Four electrons of the As atom participate in the tetrahedral bond of Si as shown in Figure 2.2 (a). The fifth electron cannot enter the bond which is now saturated and hence this electron detaches from the impurity and is free to migrate through the crystal.

The impurity is now actually a positive ion and thus it tends to capture the free electron. Because the attractive force is very weak, the free electron easily escapes to enter the CB if enough energy, E_d is gained. The energy level lies just below the CB and is called the donor level as shown in Figure 2.2 (c). These impurities are called donors.

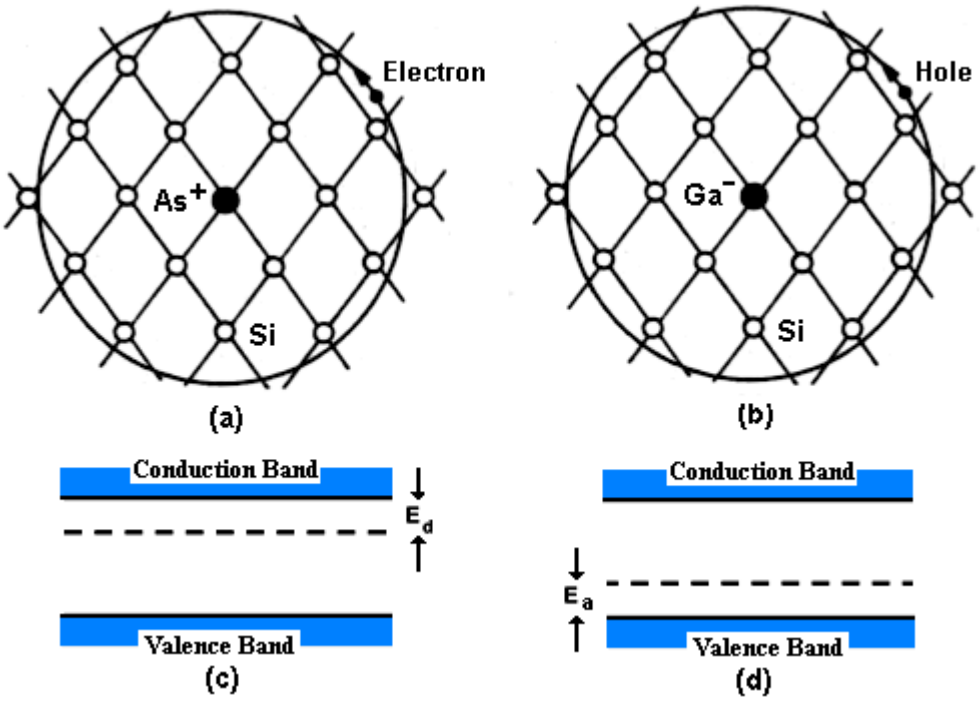

Figure 2.2: (a) An As impurity in a Si crystal. The extra electron migrates through the crystal. (b) A Ga impurity in a Si crystal. The extra hole migrates through the crystal. The donor level (c) and acceptor level (d) in a semiconductor [14].

Error! Bookmark not defined. As another example, consider the Si crystal doped with Ga impurity atoms. The Ga impurity resides at a site previously occupied by a Si atom. The Ga atom is trivalent and therefore one of the electron bonds remains vacant. This vacancy may be filled by an electron moving in from another bond, resulting in a vacancy at this latter bond. It can be considered as a hole being free to migrate through the crystal as shown in Figure 2.2 (b). Similarly, the Ga atom is negatively charged due to it accepting an electron from its surroundings and the hole is attracted by the negative Ga ion. These impurities are called acceptors and the acceptor level lies slightly above the VB as shown in Figure 2.2 (d). The electrons in the VB which gain enough energy, E_a can enter the acceptor level to fill the holes.

In the case of phosphor powders, doped with both donors and acceptors, the donor and acceptor level exist simultaneously in the band structure. Consider the standard P22G green ZnS-based phosphor: ZnS:Cu,Al,Au. Each Zn atom and S atom contribute two and six valence electrons to the bonds respectively. The ZnS compound therefore has an average of four valence electrons per atom. When the ZnS compound is doped with Al atoms that substitute Zn atoms, three valence electrons are contributed by each Al atom instead of two valence electrons from each of the Zn atoms. The extra electron does not participate in the bonds, which are saturated, and therefore migrates freely in ZnS. This creates the donor level. Similarly, Cu and Au replace Zn and contribute only one valence electron to the bonds. The vacancy or hole is produced and the acceptor level is created. The band structure of ZnS:Cu,Al,Au is shown in Figure 2.3.

When phosphors are irradiated by an energetic electron beam, electrons in the VB absorb energy and are excited across the band gap to the CB. Once electrons have been excited into the CB a transition between the CB and donor level takes places and ventually decay into lower states following the path shown in Figure 2.3. The electron then finally recombines with a hole in the VB. When the electron decays from the donor to acceptor levels, energy is released in the form of a photon with an energy of 2.34 eV. As already discussed in the previous chapter, this method of light generation is called cathodoluminescence.

According to Figure 2.3 the energy difference between the donor and acceptor level is

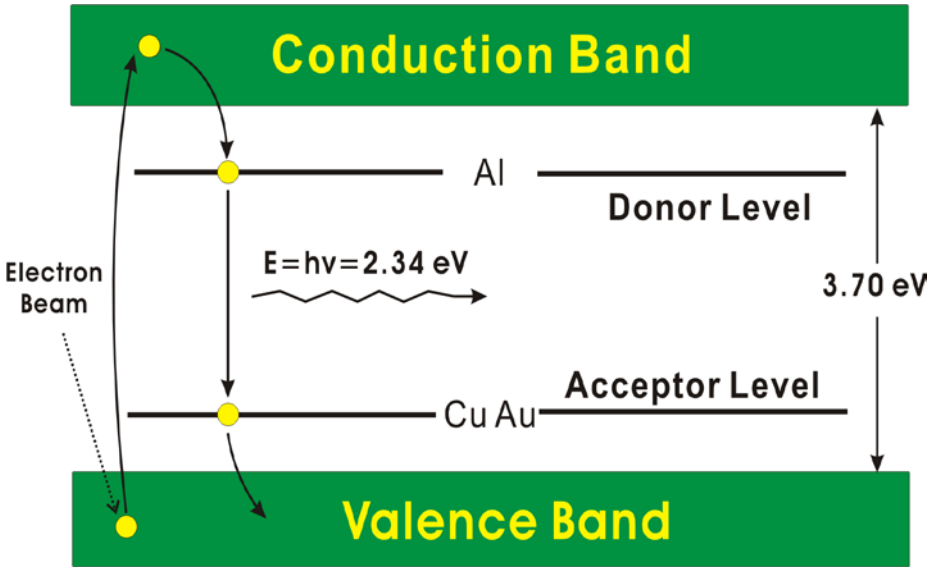

Figure 2.3: The band structure of the green ZnS-based phosphor.

about 2.34 eV, therefore the emitted photons have a similar energy. The frequency of emitted light associated with this energy is about 5.66×10^{14} Hz and the wavelength is about 530 nm, falling in the green light range. By simply doping with appropriate donors and acceptors the desired value of the energy difference between the donor and acceptor level can be varied. In other words, the colour of the light is dependent upon the dopants in the phosphors. For instance, the standard P22B blue ZnS phosphors doped with trace amounts of silver and chlorine atoms have an energy difference between the donor and acceptor level of about 2.76 eV. In this case blue photons with a frequency 6.67×10^{14} Hz and wavelength of 450 nm are emitted.

2.2 Degradation process of ZnS phosphors

The phosphor screen is a very important component of the FED. When it is irradiated by energetic electrons, energy is transferred to the phosphor powders and light is generated by the CL process. As the electron exposure time increases, there is a degradation in the CL generated in the ZnS phosphors, due to the formation of a non-luminescent ZnO layer on the surface according to the electron stimulated surface chemical reaction (ESSCR) model [15,16,17,18]. According to this model the electron beam used to irradiate the phosphor powder dissociates the ambient water vapour or oxygen gas into atomic species which then proceeds to react with carbon on the

surface to form volatile compounds and with ZnS to form a non-luminescent layer of ZnO or $ZnSO_4$ and volatile SO_2.

Itoh *et al*. [19] studied ZnS:Zn and ZnCdS:Ag,Cl powder phosphors and reported that they decomposed under electron bombardment at a background pressure of 5 x 10^{-5} Torr H_2O. Using mass spectrometry, Itoh's group reported the desorption of sulphur species from the surface. This desorption was found to be proportional to the power density of the electron beam and also the pressure of water vapour that was intentionally added to the vacuum environment. They also reported that a surface "dead layer" of $ZnSO_4$ formed after prolonged electron beam exposure.

Abrams *et al*. [18] analysed ZnS:Ag,Cl both with and without a coating of SiO_2. They reported that under high hydrogen partial pressures this SiO_2 layer acted as a catalyst for hydrogen decomposition and sulphur was removed as H_2S, leaving elemental Zn which evaporated because of a high vapour pressure. The evaporation of Zn and degradation of ZnS is accelerated by elevated temperatures caused by local electron beam heating. As found by Itoh's group, a similar result was obtained under high partial pressures of water vapour with the formation of a ZnO layer.

Similar conclusions about the study of the ZnS:Cu,Al,Au phosphor degradation were drawn by Oosthuizen *et al.* [16]. The Auger results showed that both carbon and sulphur were depleted from the near surface region of the phosphor. It was postulated that in the ESSCR model the electron beam dissociates the molecular oxygen into atomic species, which subsequently react with carbon to form volatile compounds (CO_x, CH_4, etc.) and with ZnS to form a layer of ZnO and volatile SO_2.

ZnS is a partially ionic compound of which the Zn ($[Ar]3d^{10}4s^2$) atom donates 2 electrons to the sulphur ($[Ne]3s^23p^4$) atom. The cation, Zn^{2+}, is now without any available valence electron and the highest occupied electronic level of the cation is its highest core-level. According to the Knotek-Feibelman mechanism [20] the initiating event could be the creation of a core-hole on a Zn^{2+} site at the surface by an electron beam. Since there are no valence electrons on the nearest neighbor cations, one S (3p) electron decays to fill the hole. This decay is the so-called inter-atomic Auger process and the energy released is taken up by the emission of one or two Auger electrons

from the S (3p) states, as shown in Figure 2.4. If the initial core-hole is created on the

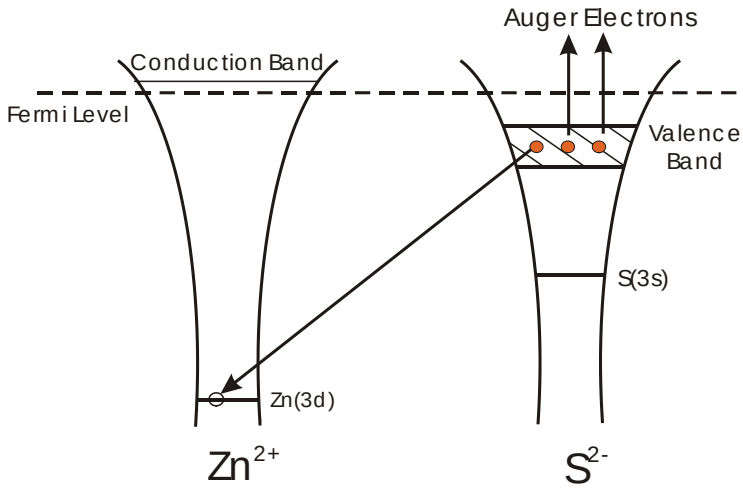

Figure 2.4: Schematic diagram of the Knotek-Feibelman mechanism.

sulphur, then an intra-atomic decay seemingly can occur with the same result. However, Knotek and Feibelman suggested that this process is inhibited by energy conservation.

The sulphur is left with a net positive charge, surrounded by positive Zn ions and therefore easily desorbed from the surface. Concurrent with the inter-atomic Auger process, molecular gas species, e.g. oxygen, are ionised by an electron beam dissociation process. The positive sulphur reacts with the negative oxygen to form SO_2 and subsequent formation of ZnO.

Swart *et al.* [15] studied the degradation of the standard ZnS:Cu,Al,Au and ZnS:Ag,Cl phosphors by Auger electron spectroscopy (AES) and CL spectroscopy. The results obtained were the same as Oosthuizen et al. The formation of a ZnO layer was demonstrated by sputter depth profiles taken after total exposures of 28 C/cm^2 and 38 C/cm^2 and found to be 1.8 nm and 3 nm thick respectively.

The same correlated AES and CL approach was used to study the effects of the electron beam on Y_2O_2S:Eu phosphor powders. Trottier *et al.* [21] reported that both sulphur and carbon leave while oxygen accumulates at the surface during electron beam exposure in residual vacuums of 10^{-8} to 10^{-6} Torr. In addition, they showed that electron bombardment in 10^{-6} Torr O_2 could result in the growth of a layer of Y_2O_3:Eu.

Electrons lose a fraction of their energy in the oxide layer during penetration, decreasing the fraction of energy loss in the phosphor bulk. The CL is dependent upon the energy loss in the phosphor and therefore the growth of the oxide layer significantly decreases the CL intensity as was shown by Kingsley and Prener [22]. They measured the CL intensity as a function of the accelerating potential of a number of powdered ZnS:Cu phosphors, each of which had a thin non-luminescent ZnS coating of known thickness deposited upon every grain. It was found that the luminescence efficiency is dominated by the power loss of the electron beam in the non-luminescent coating.

Due to the shallow excitation depth of the low energy electrons, as used in FEDs, the energy loss fraction in the phosphor bulk decreases more and therefore has a dramatic effect in FEDs. For this reason, FEDs typically require 10 times more beam current than used in CRTs to have the same level of luminance. Since the phosphor life is proportional to the beam current, phosphors in FEDs age faster. A second reason that leads to more pronounced CL degradation in FEDs is the weak vacuum conditions resulting from the large surface area to volume ratio inside the display and the subsequent extensive degassing from the surface. This degassing leads to an increase in the concentration of residual gasses with reactants facilitating the ZnO growth as predicted by ESSCR model.

2.3 Simulation techniques

Since the use of high-speed computers became widespread in the 1960s, much theoretical investigation has been undertaken and the Monte Carlo approach has been recognised as a powerful technique for performing certain calculations. In this section the Monte Carlo electron trajectory simulation, which was used to determine the electron interaction volume and energy loss profile through the ZnO layer and the ZnS bulk is briefly explained. The CL intensity calculations based on the Monte Carlo simulation techniques are also discussed.

2.3.1 Monte Carlo electron trajectory simulation

The Monte Carlo simulation of electron trajectories in a solid is based on a stochastic

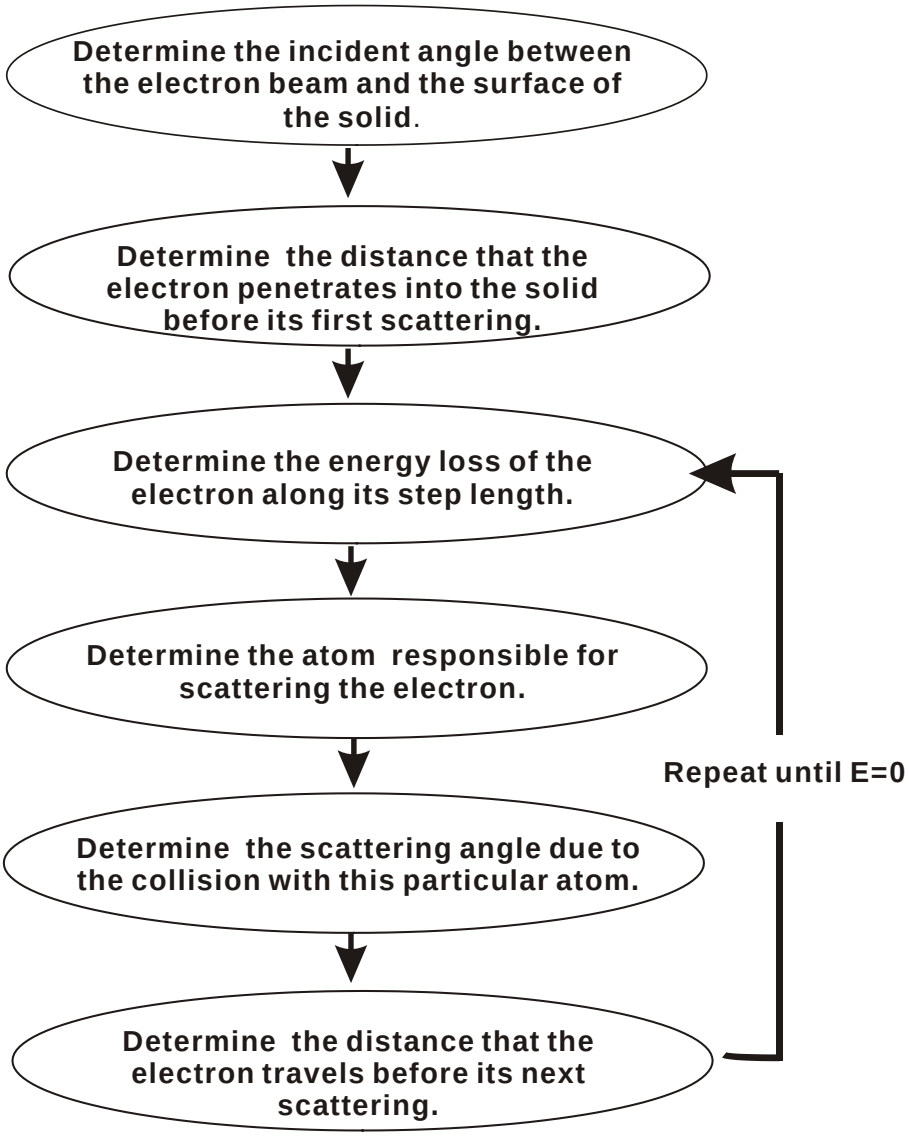

Figure 2.5: A set of the procedures summarizing the Monte Carlo method used to simulate the trajectory of a single electron in a compound.

description of the elastic scattering process. The flowchart in Figure 2.5 shows the procedures for determining the electron trajectories in the solid during the Monte Carlo simulation.

When an electron impinges on a solid at an incident angle α, it penetrates a certain distance S into the solid before it is scattered by an atom. During this step length the electron loses a certain amount of energy ΔE and changes the travelling direction when it is scattered by an atom. The electron then travels another distance before it is scattered again as shown in Figure 2.6. The process continues until the electron has

lost all its energy to the solid.

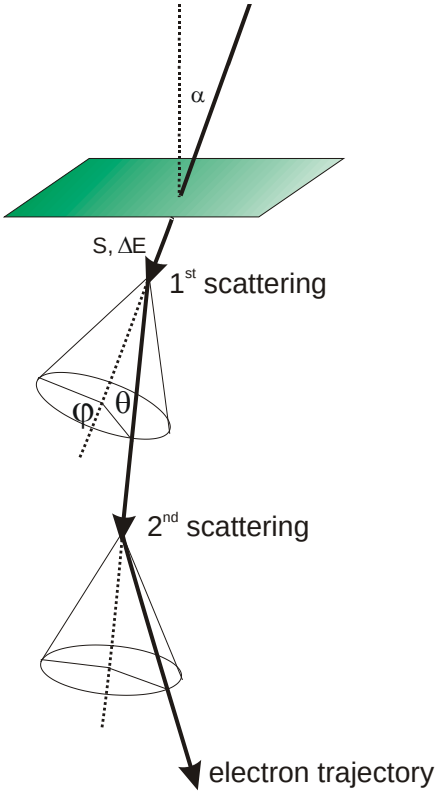

Figure 2.6: A graphical representation of the change in an electron's trajectory as it penetrates a solid at an incident angle and is scattered by the atoms of the solid [23].

The model used here is a single scattering Monte Carlo simulation and the secondary electron effect is neglected since these electrons have a relative short step length and limited energy loss. The particular values of the scattering angle, the electron energy loss and the atom responsible for the scattering in an individual event are realised by random numbers, according to certain formulae describing the scattering behavior. The accuracy of the simulation depends entirely on the correctness of the scattering models. A large number of electron trajectories statistically and dynamically replicates the combination of these scattering formulae and one can extract the information required by summing up the data derived from the history of each electron trajectory. In the following sections the models and formulae used in these procedures illustrated in Figure 2.5 are discussed in detail.

2.3.1.1 Determination of the electron's incident angle

The electron's incident angle is the angle between the direction of incident electron

beam and the normal of the surface of the solid. In the simulation this angle can be

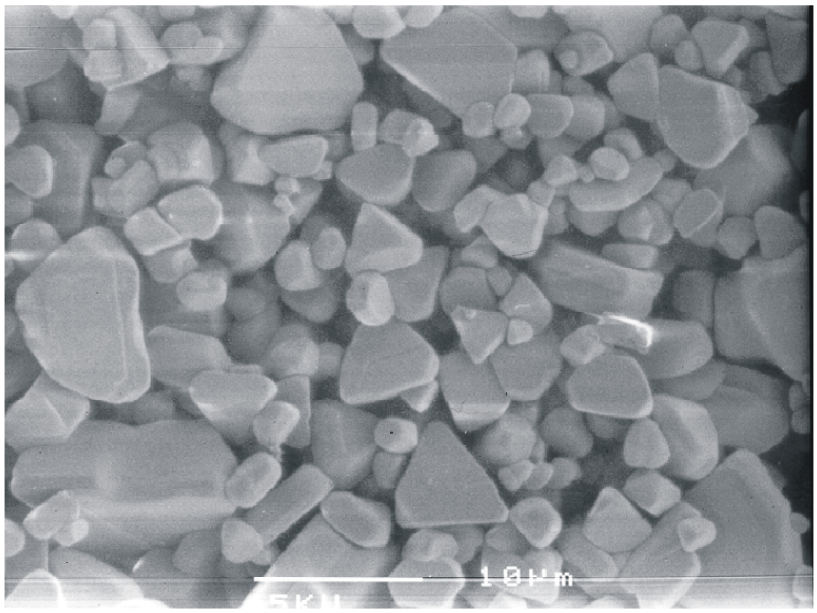

Figure 2.7: A 49×36 µm SEM image showing the phosphor powder at higher magnification. Two groups of particles can be identified in the image: flat and spherical particles, both randomly distributed over the surface.

fixed to any desired value during each new electron trajectory simulation. In reality the ZnS surface is not perfectly flat, but consists of a distribution of flat and spherical shaped particles (see Figure 2.7). Greeff and Swart [24] determined a distribution of electron beam incident angles using a Monte Carlo method. During the simulation of the electron trajectories, the incident angle of each new electron is sampled from this angular distribution to simulate the morphology at the phosphor particle.

2.3.1.2 Determination of the electron's step length

After the electron enters the solid, the distance that it travels before its first scattering event is called the step length. According to the survival equation [25]:

$$\frac{N}{N_0} = e^{-S/\lambda} \tag{2.1}$$

the fraction of electrons N/N_0 represents the remaining electrons left after the electron beam penetrated a distance S into the solid. This fraction can be represented by a random number $R \in [0,1]$. The equation for the step length is therefore given by [26]:

$$S = -\lambda \ln(R) \tag{2.2}$$

where λ is the electron's elastic mean free path. In the conventional Monte Carlo method the scattering model often assumes a uniform material of mean atomic number and mean atomic weight for the bulk material. The electron therefore travels with an average elastic mean free path. As might be expected, these Monte Carlo simulations using a homogeneous material yield results that deviate from experimental results for complex compounds. Thus, the electron elastic mean free path in a compound should sum up all contributions from each element weighted according to their respective atomic fractions. Equation 2.3 is used to describe the elastic mean free path for a compound [27]:

$$\lambda = \frac{1\times10^{-6}}{N_A} \frac{\frac{CA}{F\rho'}}{F\sigma'} \text{ (m)} \tag{2.3}$$

where C and A are the row and column vectors containing the atomic weight fraction and the atomic weight (g/mol) of Zn, S and O respectively, F and ρ' (g/cm^3) are again the row and column vectors containing the atomic fraction and density of these three elements, σ' (m^2) is a column vector containing the total elastic scattering cross-sections and N_A is Avogadro's number. The denominator $F\sigma'$ is therefore the total elastic scattering cross-section for the compound. In the expression by Hovington *et al*. [27] a mean density instead of the expression $F\rho'$ is used for the compound and therefore Equation 2.3 accommodates any change in the stoichiometry of the solid.

The value of the total elastic scattering cross-section of the individual atom is taken from a database supplied by the National Institute of Standards and Technology (NIST) [28]. The database supplies the differential and total scattering cross-sections for elements with atomic numbers between 1 and 96 and for electron energies ranging from 50 eV to 10 keV. The elastic mean free path for ZnO and ZnS, as well as the diffusion interface between the ZnO and ZnS can be calculated using Equation 2.3. The varying concentration of these three elements will vary the elastic mean free path as a function of depth in the ZnO/ZnS bulk.

2.3.1.3 Determination of the electron's energy loss

In conventional Monte Carlo simulations Bethe's stopping power in a continuous slowing down approximation is used to describe the energy loss of electrons with a negligible direction change while they move between successive scatterings. This loss of energy is due to the inelastic scattering through an electron-electron interaction. Ritchie *et al* [29] have shown that Bethe's stopping power is obtained by summation of the theoretical stopping powers for all possible electron-electron interactions. They are core electron, plasmon and conduction electron excitations. At high energy (≥ 10 keV) the Bethe equation provides an accurate expression for the stopping power. Joy and Lou [30] derived an expression in which all the available electron-electron interactions are included:

$$\frac{dE}{dS} = -\frac{7.85\times10^{12}}{E}\frac{\rho Z}{A}\ln(\frac{1.166E}{J}) \quad \text{(eV/m)} \tag{2.4}$$

where E is the electron energy (eV), ρ the density (g/cm^3), Z the atomic number, A the atomic weight and J (eV) is the mean ionisation potential of the material. The value of J is either:

$$J = 9.76Z + \frac{58.5}{Z^{0.19}} \quad \text{(eV) for } Z \geq 13 \tag{2.5}$$

or

$$J = 11.5Z \quad \text{(eV) for } Z \leq 12. \tag{2.6}$$

However, at low energies (≤ 10 keV) some inelastic election-electron interactions, like inner shell ionisations, are no longer possible. The value of the mean ionisation potential therefore decreases accordingly and it should be regarded as energy dependent rather than constant. A modified Bethe equation subsequently suggested by Joy and Luo [30] is as follows:

$$(\frac{dE}{dS})^* = -\frac{7.85\times10^{12}}{E}\frac{\rho Z}{A}\ln(\frac{1.166E}{J^*}) \quad \text{(eV/m)} \tag{2.7}$$

of which J^* is the modified mean ionisation potential:

$$J^* = \frac{J}{1+k\frac{J}{E}}. \tag{2.8}$$

Here k is a variable whose value depends on the material and is always close to but less than unity. For the Monte Carlo simulation in this study a value of 0.85 for k was used as was suggested by Joy and Luo for compounds.

The energy loss ΔE for the electron along its step length is therefore determined by:

$$\Delta E = (\frac{dE}{dS})^{*} \times S \tag{2.9}$$

where S is the step length and dE/dS is the rate of energy loss. In order to accommodate any change in the stoichiometry of the compound, Equation 2.9 is again modified as follows [27]:

$$\Delta E = \sum_{i=1}^{n} \frac{F_i A_i}{FA} (\frac{dE}{dS}_i)^{*} \times S \quad \text{(eV)} \tag{2.10}$$

where the weight fraction in the expression by Hovington *et al* [27] is substituted by the atomic fraction term, F_iA_i/FA [31]. F and A are the row and column vectors respectively containing the atomic fraction and atomic weight of Zn, S and O, and n is the number of elements in the compound.

2.3.1.4 Determination of the atom responsible for electron scattering

In the Monte Carlo simulation the electron is scattered elastically by atoms. Howell *et al.* [32] suggested that the selection of which element is responsible for scattering the electron in any event is determined by that element's contribution to the total elastic scattering cross-section of the compound. The probability, $P_\sigma(i)$ of the electron scattering from the i th element is the ratio of its elastic cross-section to that of the whole material:

$$P_\sigma(i) = \frac{F_i \sigma_i}{F\sigma'} \tag{2.11}$$

where F_i and σ_i are the atomic fraction and total elastic scattering cross-section for element i respectively. The expression $F\sigma'$ is the total elastic scattering

cross-section for the compound as mentioned in Section 2.3.1.2.

In the ZnO/ZnS system Zn, S and O atoms are selected randomly as the scattering center according to their probabilities each time. The element with higher probability has a greater chance of being selected. The sum of these probabilities is equal to unity at each selection event as shown in Figure 2.8. Therefore, in the simulation codes of this study, the range of intervals for the random number, $R \in [0,1]$, corresponding to the specific element that acts as the scattering center, is determined as follows:

The Zn atom is chosen as a scattering center if

$$0 \leq R \leq \frac{F_{Zn}\sigma_{Zn}}{F\sigma'} \tag{2.12}$$

or the S atom if

$$\frac{F_{Zn}\sigma_{Zn}}{F\sigma'} \leq R \leq \frac{F_{Zn}\sigma_{Zn} + F_S\sigma_S}{F\sigma'} \tag{2.13}$$

or the O atom if

$$\frac{F_{Zn}\sigma_{Zn} + F_S\sigma_S}{F\sigma'} \leq R \leq 1 .$$

(2 . 1 4)

By varying the atomic fraction of Zn, S and O in the vector F according to an error function it is possible to simulate the ZnO layer on top of the ZnS bulk with a diffusion layer in between as shown in the simulated depth profile in Figure 2.9. Thus, at a particular depth the atomic fraction of the individual element contained in vector F is obtained by using this simulated depth profile.

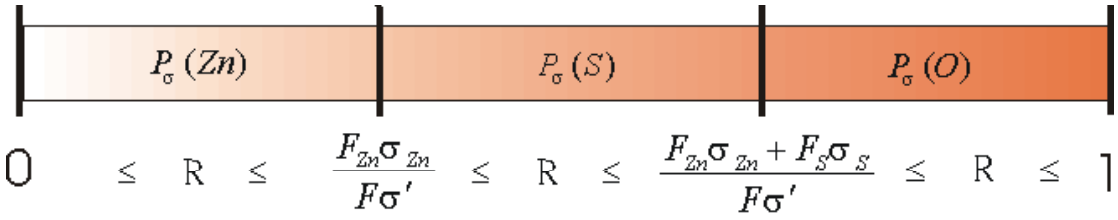

Figure 2.8: The sum of the probabilities of Zn, S and O atom being selected as a scattering center is equal to unity at each selection event. The range of intervals for the random number corresponding to a certain element acting as a scattering center can therefore easily be determined.

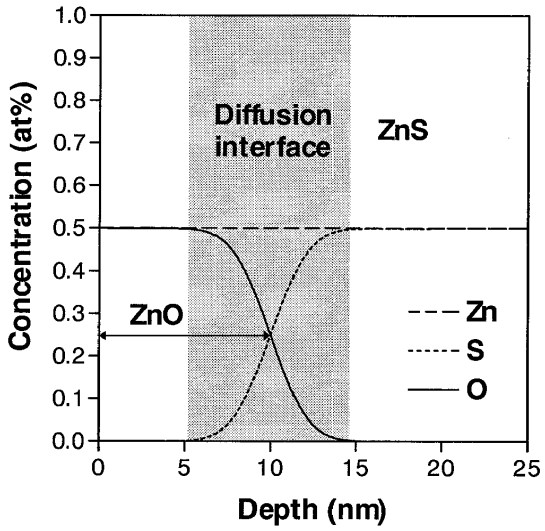

Figure 2.9: A simulated depth profile showing the atomic fraction as function of depth for a 10 mm thick ZnO layer on top of ZnS. The diffusion interface has a total width of 10nm [23].

2.3.1.5 Determination of the scattering angle

When an electron is scattered by an atom, the electron changes its direction by an angle θ, referred to as the polar scattering angle as shown in Figure 2.6. In the Monte Carlo simulation the elastic cross-section is used in two ways. Firstly the total elastic cross-section is used to define a mean free path between scattering events and secondly the polar scattering angle, θ, is a function of the differential elastic cross-section of the atom responsible for the scattering event. The most commonly used

elastic scattering cross-section is the Rutherford cross-section, which has a convenient analytical form and is straightforward to implement in a Monte Carlo calculation. However the Rutherford cross-section is a poor approximation when applied to a solid with a high atomic number and low energy electrons. Therefore the Mott scattering cross-section [33], derived by the partial wave expansion method, is used instead of the Rutherford cross-section. These values of differential Mott scattering cross-section are also available from the NIST database [28].

In Figure 2.10 the polar scattering angles are shown for Zn, S and O as function of electron energy and an interval between 0 and 1 according to values obtained from the NIST database.

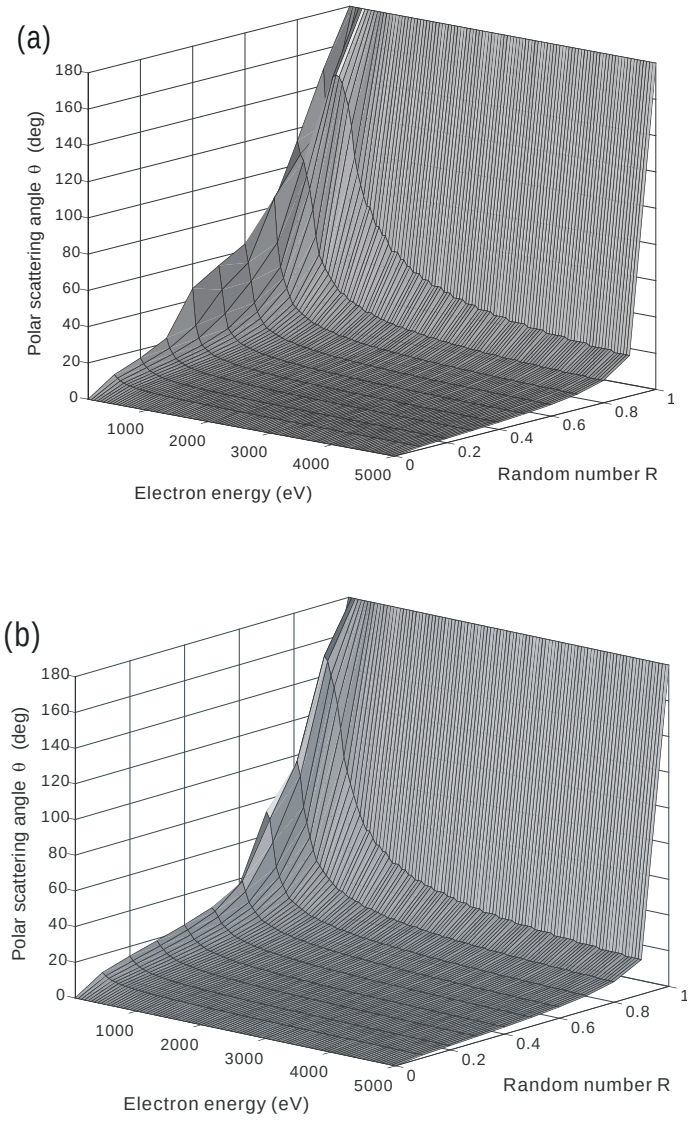

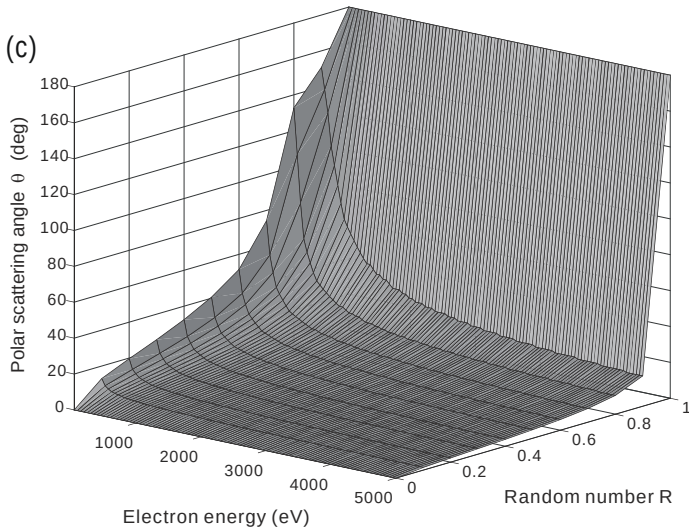

Figure 2.10: The polar scattering angles for (a) Zn atom, (b) S atom and (c) O atom as function of electron energy and a random number as provided by the NIST database [28].

2.3.1.6 Performance of the electron trajectory simulation

The Monte Carlo electron trajectory simulation codes were written according to the above mentioned models and formulae in the Matlab programming environment by Greeff and Swart [23]. In Figure 2.11 a Monte Carlo simulation is shown for the trajectories of 100 electrons, each with an initial energy of 2keV, through a 10 nm thick ZnO layer into the ZnS bulk. The layer between two shaded planes represents the diffusion interface, having a total thickness of 10 nm. The concentration of S and O above, within and below the diffusion interface varies according to the depth profile shown in Figure 2.9 with the thickness of the ZnO layer taken at depth where O decreased to 50% of its original concentration. An angular distribution of incident angles, accommodating for the powder's morphology, is used in Figure 2.11. However, a large number of electron trajectories should be simulated in order to obtain reliable information and Figure 2.11 is for illustration purposes only.

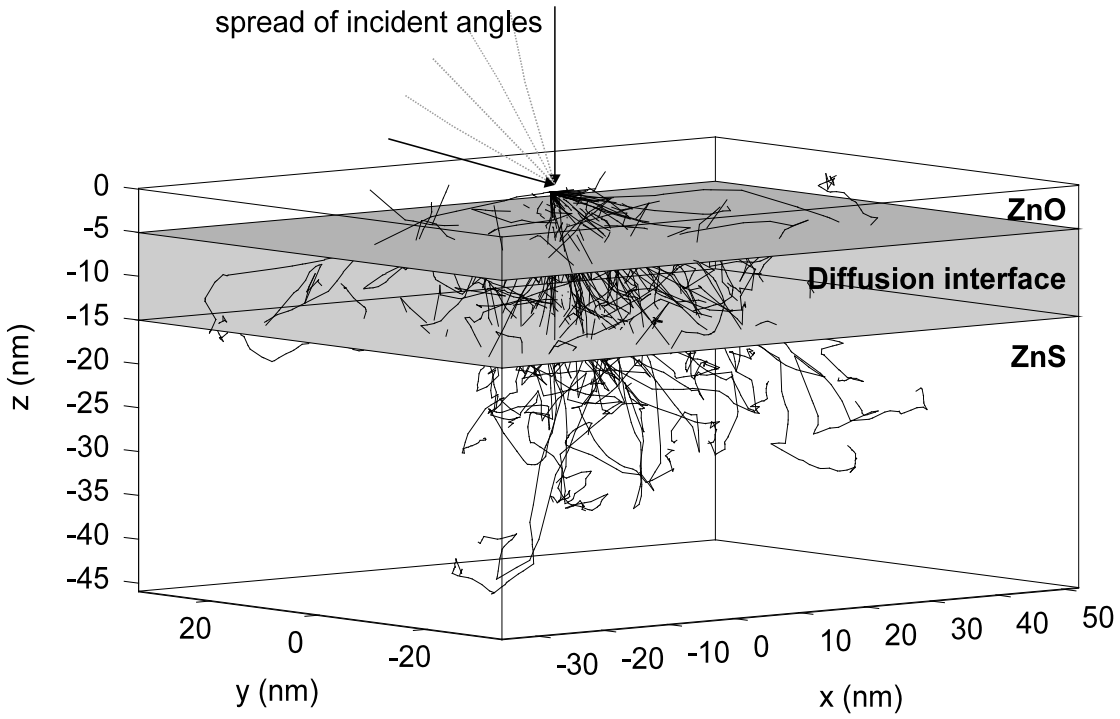

Figure 2.11: A Monte Carlo simulation of 100 electron trajectories with an initial 2 keV energy. The shaded region represents the diffusion interface between the ZnO layer and the ZnS bulk. The concentration of Zn, S and O follows that of the simulated depth profile shown in Figure 2.9 with the 50% mark of O at a depth of 10 nm [28].

The above-mentioned Monte Carlo code is applicable to both standard ZnS-based green and blue phosphors due to the very low concentration of dopants used in different phosphors. The dopant concentration can therefore be neglected for all practical purposes when the electron trajectories are simulated.

2.3.1.7 Energy loss profile

An energy loss profile that contains the details of the calculation of the energy loss as a function of the depth into the solid is necessary for the CL intensity. From the simulation results the exact position of each scattering event and the electron's associated energy at that position are known and therefore the energy loss rate $\Delta E / \Delta z$ between two subsequent scattering events at depths z_i and z_{i+1} can be determined:

$$\frac{\Delta E_z}{\Delta z} = \frac{E_i - E_{i+1}}{z_i - z_{i+1}} \tag{2.15}$$

The interaction volume between depths z_i and z_{i+1} is divided into 0.1 nm thick layers with the energy loss spread through these layers. The total energy loss of electrons in each layer is calculated and gives the total energy loss as function of the depth into the bulk [34].

In Figure 2.12 the simulated electron trajectories as shown in Figure 2.11 were used to determine an illustrative energy loss profile. Each layer is 10 nm thick, leading to a rough approximation of the energy loss profile. On the top of the energy loss profile is the fractional energy loss. This shows the fraction of the energy lost in each layer with respect to the total input energy, in this case is 200 keV (2 keV/electron $\times$ 100 electrons). The sum of all the fractional energy losses in the layers is 0.73 or 146 keV/200 keV, which is less than unity. This indicates that energetic electrons were backscattered during the simulation.

2.3.2 Quantification of the CL intensity for the ZnO/ZnS system

When the phosphor powder is irradiated by an electron beam, e-h pairs are generated

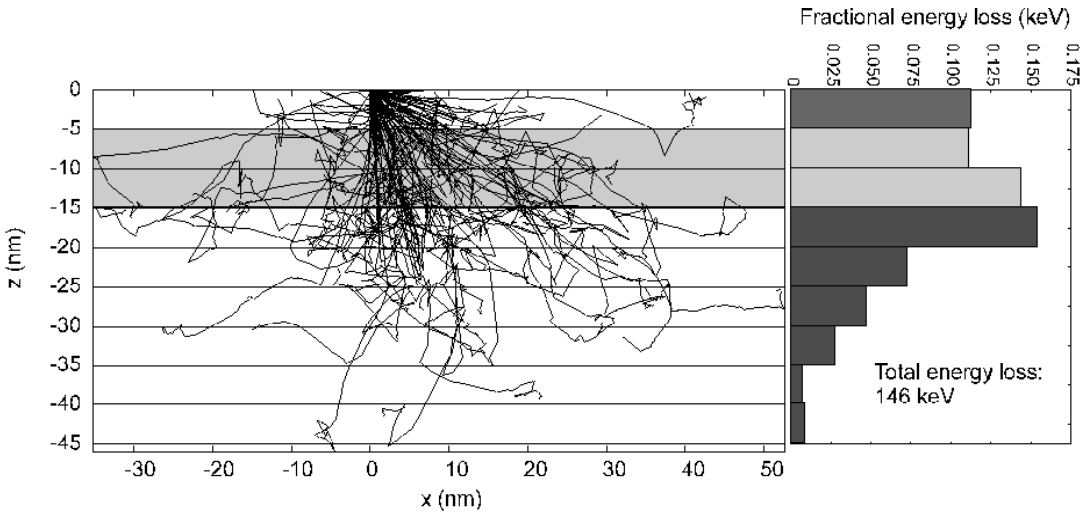

Figure 2.12: The energy loss profile of the electron trajectories shown in Figure 2.9. The interaction volume is divided into horizontal layers and the energy lost by electrons is summed up at each layer. The shaded region represents the diffusion interface [23].

in the vicinity of the point of impact. The e-h pairs recombine either radiatively or non-radiatively. In the case of radiative recombination, photons are emitted, as mentioned in Section 2.1. These photons propagate in all directions and a small fraction of these emerge from the surface, giving rise to the measured CL intensity. Therefore the e-h pair generation rate and subsequent photon generation rate is determined by the energy loss rate of incident electrons. In other words, it can be assumed that CL generation is proportional to the rate of the electron energy loss in the phosphor powder [22]. In the previous section it was shown how an energy loss profile of an electron trajectory simulation can be obtained and this will now be used to determine the CL intensity.

The photon detection rate $N(\lambda, z)$ for photons of wavelength λ at a depth z is given by [35]:

$$N(\lambda, z) = Q(\lambda, z)[1 - A(\lambda, z)]D(\lambda) \quad (\text{counts.s}^{-1}) \tag{2.16}$$

where $Q(\lambda, z)$ is the photon yield of the material that determines the number of photons of wavelength λ generated per second in the solid at depth z. The fraction of generated photons lost in the solid at depth z is due to the effect of internal optical absorption, total internal reflection losses and Fresnel losses at the surface. These losses are accommodated in the expression $A(\lambda, z)$. The overall detection efficiency of the spectrometer is given by $D(\lambda)$.

The photon yield is given by:

$$Q(\lambda, z) = G(z)\eta_i \tag{2.17}$$

where $G(z)$ is the e-h pair generation rate at the depth z and η_i is the ratio of the radiative recombination rate to the total recombination rate. For a semiconductor G is given by:

$$G = \frac{EI_b}{qE_i}(1 - \eta) \quad (\text{s}^{-1}) \tag{2.18}$$

where E is the electron beam energy, I_b the electron beam current, η the electron

backscattering coefficient, q the electron charge and E_i the average energy required to create an e-h pair.

From the definition of electron beam current, charge per unit time, I_b can be expressed as:

$$I_b = C/t = nq/t \tag{2.19}$$

where n is the number of electrons used in simulating an energy loss profile. By substituting Equation 2.19 into Equation 2.18 G can be written as:

$$G = \frac{En(1-\eta)}{E_i t} \tag{2.20}$$

where the numerator gives the total energy loss in the interaction volume. The depth distribution of this total energy loss is known from the previously determined energy loss profile. The e-h generation rate can therefore be expressed as a function of the depth z:

$$G(z) = \frac{\Delta E(z)}{E_i t}. \tag{2.21}$$

When the non-luminescent ZnO layer forms on top of the ZnS bulk, only the e-h pairs generated in ZnS contribute to G. Thus the e-h pair generation rate in ZnS is given by:

$$G(z) = \frac{\Delta E_{ZnS}(z)}{E_i t} \tag{2.22}$$

where $\Delta E_{ZnS}(z) = \Delta E(z) F_{Zns}(z)$ and $F_{ZnS}(z)$ is atomic concentration of ZnS at depth z and is obtained from a simulated depth profile, similar to the one shown in Figure 2.7. Equation 2.17 therefore has the form:

$$Q(\lambda, z) = \frac{\Delta E_{ZnS}(z)}{E_i t} \eta_i. \tag{2.23}$$

The optical losses $A(\lambda, z)$ in the solid at depth z are given by [36]:

$$A(\lambda, z) \approx 1 - [(1-R)(1-\cos\theta_c)e^{-\alpha z}] \tag{2.24}$$

where (1-*R*) accounts for the normal reflection losses at the solid-vacuum interface, $(1-\cos\theta_c)$ describes the total internal reflection at a certain critical angle θ_c determined by the material's refractive indices. The expression $e^{\alpha z}$ is the optical self-absorption with α the absorption coefficient and *z* the optical path length. In the ZnO/ZnS system the photon must travel from its generation through the ZnS and ZnO layer to the surface. Because of the different optical characteristics and absorption of photons in ZnO and ZnS, the photon transmittance function $\alpha'(z)$ is used to accommodate for this and is defined as:

$$\alpha'(z) = e^{-\alpha_{ZnO} z} F_{ZnO}(z) + e^{-\alpha_{ZnS} z} F_{ZnS}(z) \tag{2.25}$$

where the expressions $e^{-\alpha_{ZnO} z}$ and $e^{-\alpha_{ZnS} z}$ are the transmittance factors for ZnS and ZnO respectively. The atomic concentrations of ZnO and ZnS at depth *z* are again obtained from the depth profile.

By substituting Equations 2.23 and 2.25 into Equation 2.16, the photon detection rate is given by:

$$N(\lambda, z) = \frac{\Delta E_{ZnS}(z)}{E_i t} \eta_i (1-R)(1-\cos\theta_c)\alpha'(z) D(\lambda)\,. \tag{2.26}$$

During the Monte Carlo simulation the time parameter in Equation 2.26 is constant if the same number of electrons is used. Other parameters, like the radiative quantum efficiency (η_i), the normal reflection losses at the solid-vacuum interface (1-*R*), the total internal reflection $(1-\cos\theta_c)$ and the detector efficiency D(λ), are independent of the energy loss in the solid. Consequently Equation 2.26 becomes:

$$N(\lambda, z) = \Delta E_{ZnS}(z)\alpha'(z)K \tag{2.27}$$

where *K* is a constant grouping together all parameters that are constant with respect to energy loss in Equation 2.26. In order to obtain the value for the total CL generated

in the volume, Equation 2.27 is then integrated along the entire path length of the interaction volume:

$$N(\lambda)_{total} = K\int_{-\infty}^{0} \Delta E_{ZnS}(z)\alpha'(z)dz \qquad (2.28)$$

where the constant K is removed by quantifying the CL intensity generated in the ZnS phosphor without the ZnO layer that gives a reference value $N_0(\lambda)_{total}$. The subsequent values are therefore normalised with respect to this reference value ($N(\lambda)_{total} / N_0(\lambda)_{total}$) leaving the absorption coefficients (see Equation 2.25) the only parameters left to be determined. For green and blue light with wavelengths between 450 to 500 nm the absorption coefficient has a value 0.5×10^{-4} A^{-1} for ZnO and 3×10^{-4} A^{-1} for ZnS [23]. These values are used in Equation 2.25 to quantify the CL intensity for both ZnS-based green and blue phosphor powder.

Chapter 3

Experimental techniques and procedures

This chapter gives a brief outline of the surface analysis techniques and experimental procedures followed in this study, as well as the computational details of the Monte Carlo simulation.

3.1 Experimental instruments and surface techniques

3.1.1 Vacuum Chamber

A PHI model 549 (see Figure 3.1) was used in this study for the Auger electron spectroscopy (AES) measurements. The unit fabricated from stainless steel consists of a chamber that is divided into two compartments by a moveable valve. The AES apparatus, which consists of the ionisation pressure gauge, the differential ion gun, the gas analyser and the sample carousel are situated in the top chamber. The bottom chamber houses the ion pump and titanium sublimation pump. In addition to these two high vacuum pumps, there is a turbo molecular pump and a rotary pump located outside the chamber. These pumps are used in helping to maintain an ultrahigh vacuum (UHV) in the chamber. There are numerous leaking valves attached to the top chamber enabling the inlet of various gases. There are three heating elements located around the bottom chamber that can be used to bake the UHV system in order to remove water vapour, promote outgassing of adsorbed gas species and increase the UHV condition.

3.1.2 Auger Electron Spectroscopy (AES)

When the phosphor powder is irradiated by an electron beam, CL is generated close to the surface of the phosphors. The surface chemistry therefore dramatically influences the efficiency of the phosphor. AES is capable of identifying individual elements in the first few monlayers of a sample and is therefore particularly suited for surface

Figure 3.1: A photograph of PHI Model 549 unit.

analysis.

3.1.2.1 The Auger effect

When a specimen is excited by an electron beam, inner shell electrons are removed from the atoms present in the specimen, with the resultant vacancy soon filled by an electron from one of the outer shells. As shown in Figure 3.2, the energy released in this transition is transferred to an adjacent electron, which is ejected from the atom. The ejected electron is called an Auger electron and this process is called the Auger effect.

The Auger electron moves through the solid and loses energy through inelastic collisions with bound electrons. However, if the Auger electron is released sufficiently close to the surface, it may escape from the surface with little or no energy loss and be detected by an electron spectrometer as an Auger electron. Due to the specific energy levels involved in the transition and the energy of the detected Auger electron, the atom from which the electron was ejected can be identified.

3.1.2.2 AES system

The AES system consists of a single pass cylindrical mirror analyser (CMA), an electron gun and an electron multiplier. The electron gun and the electron multiplier

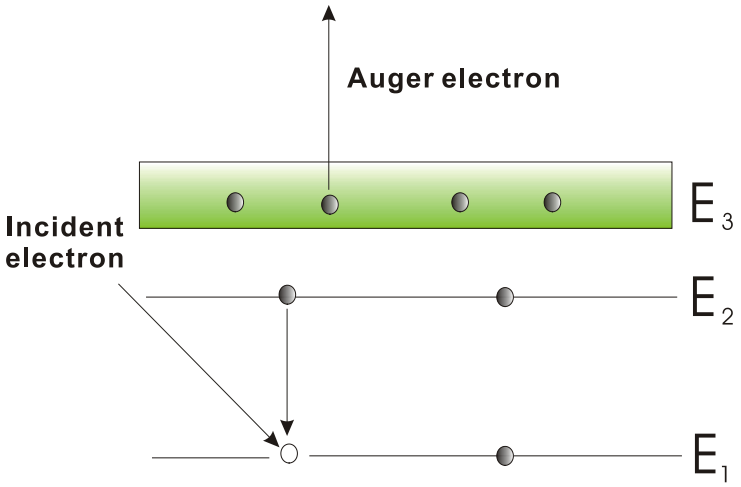

Figure 3.2: A sketch illustrating the Auger effect.

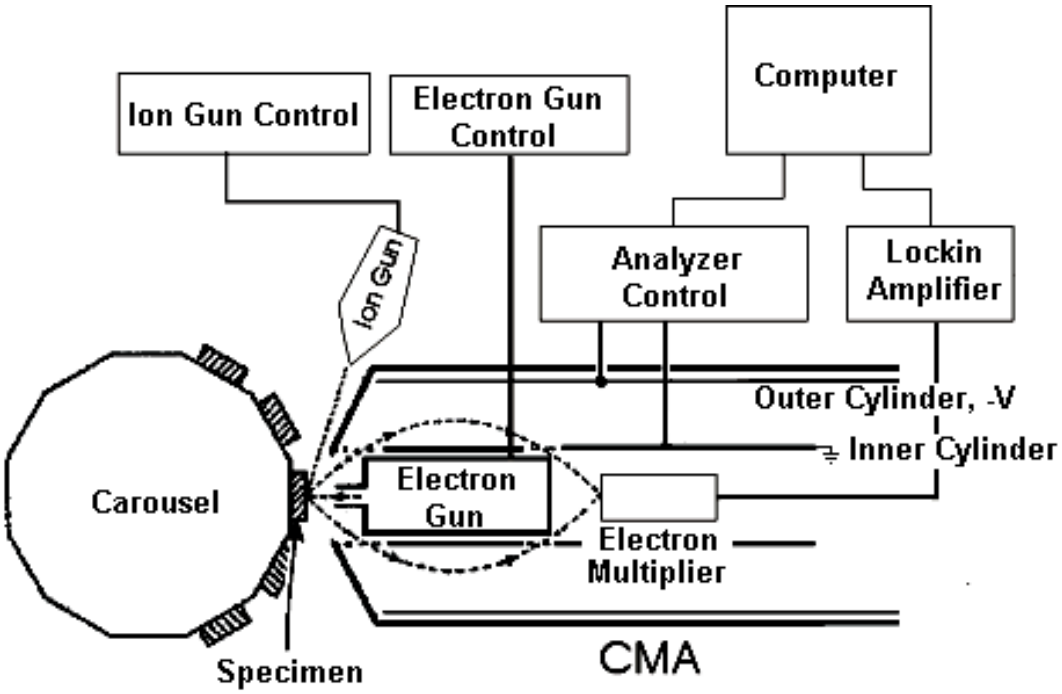

Figure 3.3: The schematic diagram of the AES system.

are incorporated in the CMA as shown in Figure 3.3. The carrousel with sample holders is located at the focus point of the CMA. Electrons generated by the electron gun are accelerated toward the specimen. As mentioned in the previous section, Auger electrons are emitted radially in a field-free space to pass through a mesh-covered slit in the wall of the earthed inner cylinder. The electron then experiences a repulsive field from the outer cylinder at potential $-V$, and are deflected to pass through a second mesh slit in the earthed inner cylinder, eventually focused on the channel electron multiplier (CEM) for detection purposes.

With the use of a differentially pumped ion gun, the Auger system can also be used to obtain a depth profile. As the ion gun sputters the material away, the electron probe is focused on the same spot (see Figure 3.4). The ejected Auger electrons are analysed and give information about the changes in element concentration layer by layer during sputtering. In this study the depth profile of the degraded sample was used to determine the thickness of the ZnO layer formed on top of the ZnS phosphor powder.

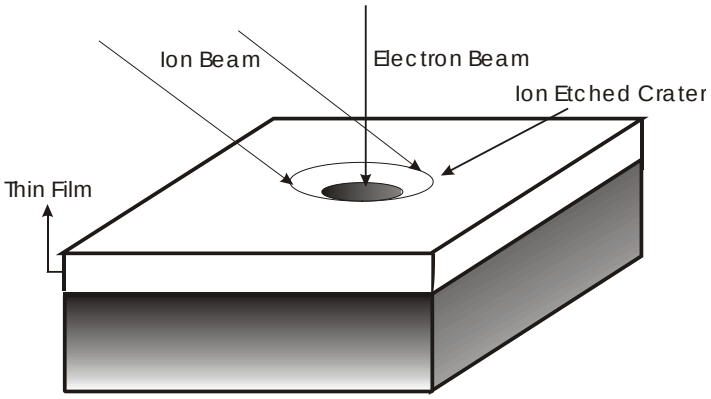

Figure 3.4: The schematic diagram of the simultaneous use of sputtering ion beam and AES to obtain a depth profile.

3.1.3 Optical spectrometer

The S2000 spectrometer [37] was used in this study to measure the CL intensity of the ZnS phosphor powder. It has a highly sensitive 2048-element linear CCD-array detector that accepts light energy transmitted through the optical fiber and disperses it via a fixed grating across the reflectors (see Figure 3.5.). Table 3.1 summarises some specifications of the Ocean Optics S2000 spectrometer.

The Ocean Optics S2000 controlled with OOIBase software, which is a basic acquisition and display software application that provides a real-time interface to a

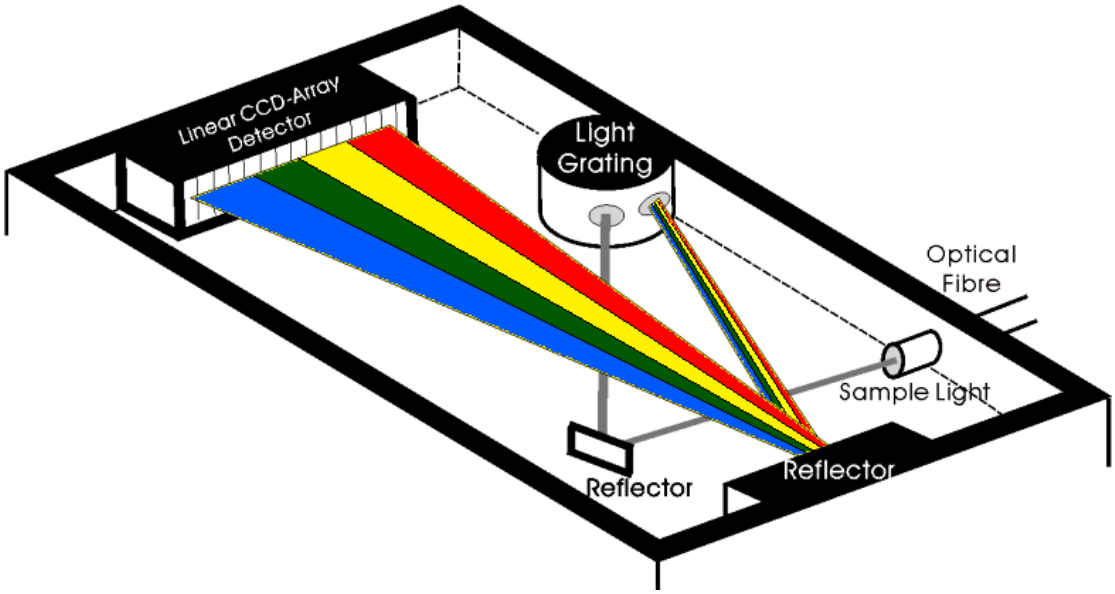

Figure 3.5: A diagram showing the inside of the optical spectrometer.

Dimensions	141.6mm×104.9mm×40.9mm
Detector range	200-1100 nm
Detector	2048-element linear silicon CCD array
Grating	14 Gratings : UV through Shortwave NIR
Optical resolution	~0.3-10 nm FWHM (depending on grating and size of entrance aperture)
Stray light	<0.05% at 600 nm; <0.10% at 435 nm; <0.10% at 250 nm
Sensitivity	86 photons/count (for 1 second integration)

Table 3.1: Some specifications of Ocean Optics S2000 spectrometer [38]. For more information see Ocean Optics website: http://www.oceanoptics.com.

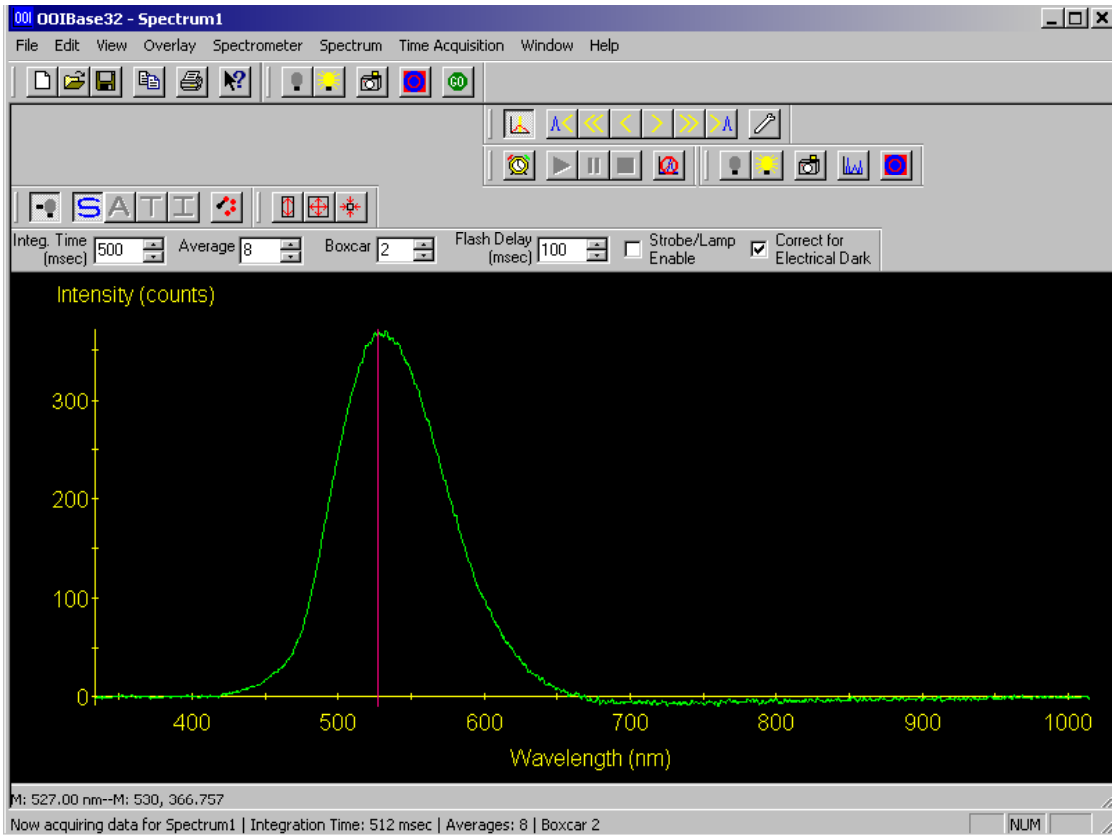

Figure 3.6: A screen shot of the interface of the OOIBase software taken while measuring the CL intensity.

variety of signal-processing functions. The real-time display of data allows the user to evaluate the effectiveness of experimental setup and data processing selection. OOIBase also allows the user to view spectral data from up to 8 spectrometer channels for multi-tasking purposes. In the experimental measurements of this study only one channel was chosen to measure the CL intensity of light generated by the ZnS:Cu,Al,Au phosphor powder during the electron beam irradiation. Figure 3.6 shows the screen shot of the interface of OOIBase while measuring the CL intensity of the ZnS:Cu,Al,Au phosphor powder. The spectrum shows that the standard P22G phosphor sample generates green light with the maximum peak height at 530 nm.

3.2 Experimental procedures

3.2.1 Degradation of ZnS:Cu,Al,Au phosphor in oxygen gas

Phosphor powders of standard ZnS are generally produced in a series of calcining, grinding and annealing steps. Activators and dopants are introduced and dispersed in the phosphors during high temperature solid reaction. The phosphor powders used in this study were standard ZnS:Cu,Al,Au (P22G) obtained from Osram Sylvania [39] and compacted into the small holes of the copper sample holders. Each sample holder has four holes drilled into it. Their dimensions are shown in Figure 3.7. The sample holders were cleaned with acetone before compacting the phosphor powders. The P22G ZnS phosphor consisted of particles with a bi-modal size distribution between 1.4 and 4.5 μm. The bigger particles were elongated in one direction up to 10 μm (see Figure 2.7).

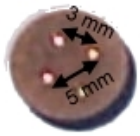

Figure 3.7: A photograph of a Cu sample holder with four 1 mm depth holes drilled into it. The specific separation distances are indicated on the photograph.

3.2.1.1 Degradation performed under minimised baking system

Figure 3.8 schematically depicts the experimental setup used for the degradation study. When a vacuum of at least 10^{-9} Torr was reached through a series of pumping

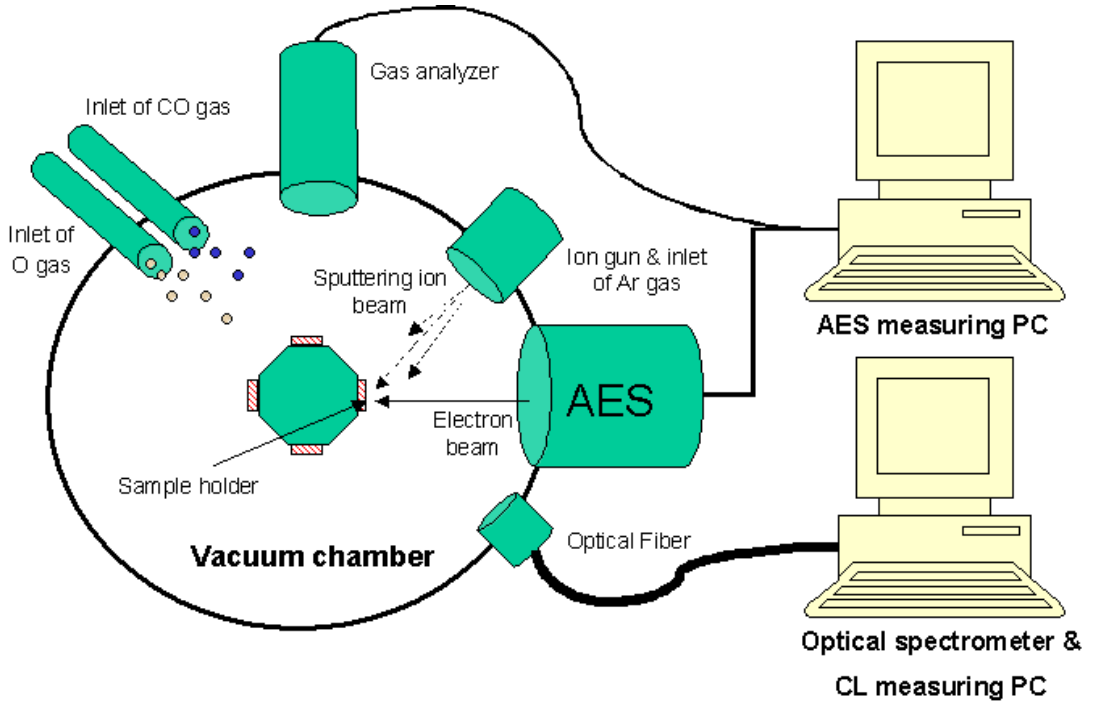

Figure 3.8: A schematic diagram of the experimental setup, including two data acquisition PC's – one for AES data and the other for data from the optical spectrometer.

procedures, the system was baked for 12 hrs. During this bake-out, the pressure dropped to below 3×10^{-9} Torr. In order to ensure that initial experimental conditions were the same each time, a base pressure of at least 3×10^{-9} Torr was achieved in the vacuum chamber each time before a phosphor degradation study was performed.

The sample of P22G phosphor was sputter-cleaned to remove any surface contaminants and then subjected to electron bombardment at an oxygen gas pressure of 1×10^{-6} Torr. The valve between the upper and lower chamber was only slightly opened and oxygen was admitted through a leak valve to maintain the required oxygen pressure and flow rate.

The AES spectra (25-1100 eV) were recorded in the dN/dE mode with a modulation voltage of 4 V peak to peak. The multiplexer was used to measure the Auger peak to peak heights (APPHs) in pre-selected energy intervals with time. The energy intervals used in the multiplexer setting for each selected element in this study are given in Table 3.2. The kinetic energy of the electron beam was 2 keV and the emission current was maintained at a value of 10 μA. The electron beam diameter and current density were determined as 128 μm and 78 mA/cm^2, respectively. The procedure for

Element	Lower limit	Upper limit
S	140	162
C	250	285
O	500	525
Zn	980	1005

Table 3.2: The multiplexer energy intervals for S, C, O and Zn.

determining the beam diameter and current density was explained in Appendix A.

The phosphor sample was degraded repeatedly to certain pre-selected chosen percentages. These were 20%, 40%, 60%, 80%, and almost 100%. For a 20% degradation, the phosphor powder was degraded until the S APPH dropped to 80% of its initial value. A similar approach was followed for the other four degradation percentages. After each degradation experiment, a depth profile was obtained by using an ion gun to sputter-clean the degraded surface as described in Section 3.1.2.2.

An ion beam voltage of 2 keV and emission current of 1.5 mA were used during sputtering at a backfilled Ar pressure of 1.5×10^{-4} Pa. The ion beam was rastered over an area of 6 mm × 6 mm. The sputtering rate at these conditions was determined as 3.9 Å/min. The determination of the sputtering rate is also explained in Appendix A. A summary of the experimental settings of several control units is given in Table 3.3. The samples were sputter-cleaned in order to make sure the initial condition of the surfaces were identical for the different degradation experiments.

3.2.1.2 Degradation performed simultaneously with CL measurement

The AES and CL, both excited by the same electron beam, were measured simultaneously (see Figure 3.8). The ion gun was rastered over an area of 6 mm×6 mm on previous work. This sputtering area may cover the adjacent phosphor samples (see Figure 3.7). As shown by Swart *et al.* [15], the damage effect incurred by ion sputtering is detrimental to the luminescence properties of phosphor powders. Thus, the second phosphor sample on the other sample holder was degraded without sputter-cleaning the surface. The degradation was performed under the same

Electron gun	
Beam energy	2 keV
Beam emission current	10 μA
Ion gun	
Beam energy	2 keV
Beam emission current	1.5 mA
Gas	1.5×10^{-4} Pa Ar gas
Raster (cleaning)	3 mm × 3 mm
Raster (depth profile)	6 mm × 6 mm
Spectrometer	
Scan rate	5 eV/s
Modulation voltage (peak to peak)	4 V
Time constant	0.3 s
Sensitivity	200×
Voltage of the multiplier	1750V

Table 3.3: A summary of the experimental settings of several control units that were used in this study.

experimental conditions as described in Section 3.2.1.1.

The CL measurements were done on the emitted light at an angle of 90° to the incident electron beam. The CL data were collected by the S2000 spectrometer through a quartz port and an optical fiber. Some procedures were followed before the collection of CL data. Firstly, the influence of the surrounding light from the environment on CL was minimised by covering the viewing ports with thin foil. Secondly, the instrumental light in the vacuum chamber was recorded by the OOIBase. The software OOIBase automatically deducted the intensity of the instrumental light from the measurements of the CL intensity that was generated from the phosphor. The instrumental light was generated by the filaments of the ionisation gauge and the electron gun. A typical spectral distribution curve of the CL is shown in Figure 3.6. The CL generated from ZnS:Cu,Al,Au phosphor has a maximum peak at

530 nm. The intensity of the maximum peak at 530nm wavelength was measured with time while the phosphor sample was degrading.

3.2.1.3 Degradation performed under maximised baking system

The vacuum chamber was baked for more than 72 hours at a base pressure of 3×10^{-9} Torr. It was believed that most of the water vapour in the chamber was removed after this long baking period. The sputter-cleaned phosphor sample was degraded in the same oxygen pressure with the same electron energy and emission current as described in Section 3.2.1.1. The sample was degraded again repeatedly to the five pre-selected percentages but the way in which the percentage degradation was determined here is different. This is explained in Section 4.2.2 and shown in Figure 4.17

3.2.2 Degradation of ZnS:Cu,Al,Au phosphor in gas mixtures

As before, the sputter-cleaned phosphor sample was subjected to 2 keV electron bombardment at an emission current 10 μA in two different mixture of gases and argon gas. The first gas mixture consisted of oxygen, carbon monoxide and argon gas. The second gas mixture consisted of oxygen and carbon monoxide gas. The sample was repeatedly degraded in these different mixtures of gases whose partial pressures were kept constant. The total pressure was maintained at 1×10^{-6} Torr. The valve between the chambers was again slightly opened and the various gases were admitted through the leak valves to maintain the required total pressure.

A gas analyser was used to monitor and record the ratios of these gases in the mixture. The gas analyser indicated that the partial pressures of the various leaked gases were stable after an hour. The degradation of the phosphor was therefore performed one hour after gas inlet was initiated.

3.3 Simulation procedures

The source code for the Monte Carlo electron trajectory and the CL intensity quantification simulations were written in the Matlab programming environment by Greeff and Swart [23]. The code was used to simulate the electron penetration into

and energy loss in the ZnS bulk covered by a ZnO layer with a certain thickness. The relative CL intensity was then quantified from the energy loss profile obtained during

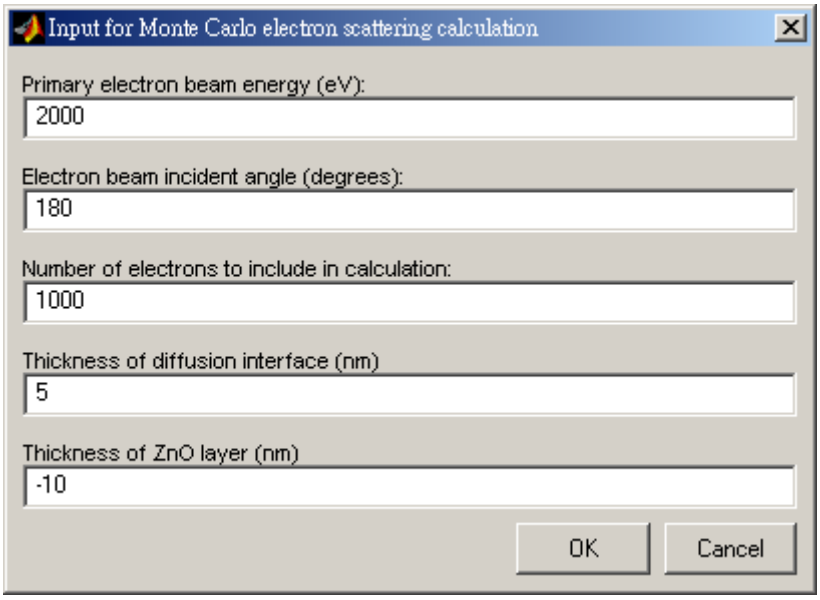

Figure 3.9: The interface window for the Monte Carlo trajectory simulation parameter inputs in Matlab.

the electron trajectory simulation. The details of the models and formulae used in the source codes were discussed in Section 2.3.

The program **gui.m** (version 1.0) modified from **energyloss.m** is the main program to simulate the low energy electron trajectories in ZnO/ZnS system using the Monte Carlo method. It is retrieved from within the Matlab command window and produces an interface window for the parameter inputs as shown in Figure 3.9.

The first input is the primary electron beam energy that represents the initial energy of the incident electrons expressed in eV. The second input is the electron beam incident angle and refers to the angle of incidence between the electron beam and the surface of the solid. If the electron beam incident angle is set to a value of 180, a distribution of the incident angles ranging from 0° to 90° is used for the electron beam to simulate the morphology of the phosphor surface as discussed in Section 2.3.1.1. The third input specifies the number of electrons representing the total number of simulated electron trajectories. The fourth input is the thickness of the diffusion interface between the ZnO layer and ZnS bulk. For example, the diffusion interface has a total width of 10 nm in Figure 2.9. The fifth and final input refers to the thickness of the

ZnO layer. This is taken from the surface to the depth where O decreased to 50% of its original concentration.

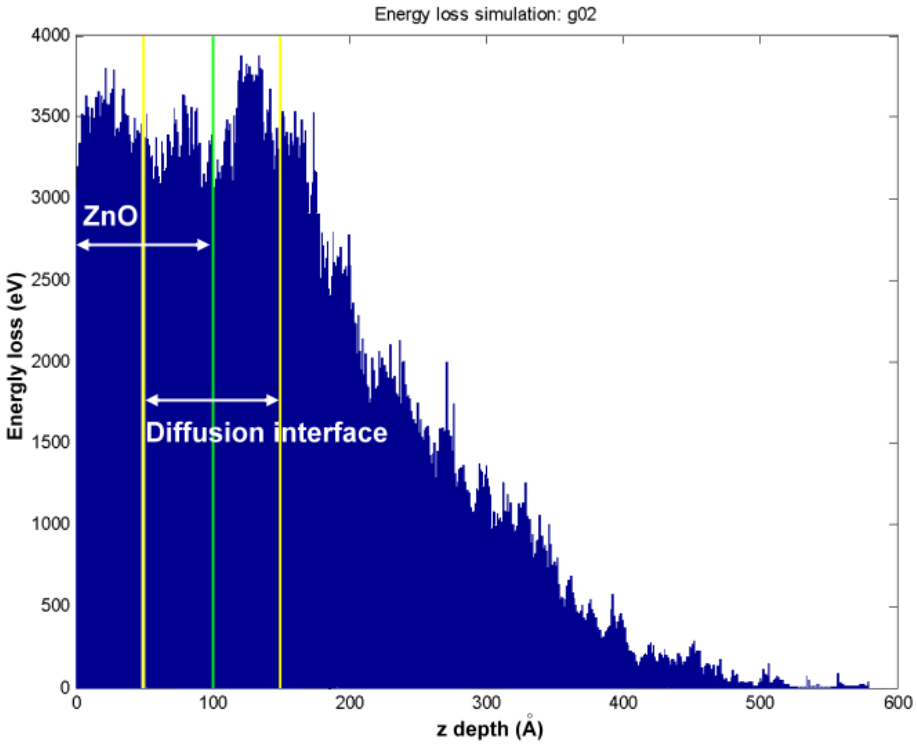

Figure 3.10: The energy loss profile of 1000 electron trajectories in the ZnS bulk with a 10 nm thick ZnO layer on top. A diffusion interface with a total width of 10 nm was used in the simulation. The initial electron beam was 2 keV with incident angles selected according to a distribution of incident angles [23].

After the calculation of the electron trajectories, an energy loss profile is produced as illustrated in Figure 3.10 and saved to a native Matlab data file, called **filename.mat**.

The code, **cl.m,** calculates the relative CL generated during the energy loss of electrons moving through a solid. Two parameters have to be keyed in. One is the previously generated energy loss profile, **filename.mat** that is needed to quantify the relative CL intensity. The other is a binary switch that either corrects for the luminescence of the diffusion interface or does not. The correction can be set to zero if the ZnS in the diffusion interface is luminescent, else a value of 1 assumes that the material in the interface is non-luminescent. Figure 3.11 illustrates the output screen of the Matlab function **cl.m** as retrieved from the command window.

3.3.1 CL simulation with different electron incident energy

The first set of simulations was performed to see the effect of the primary electron

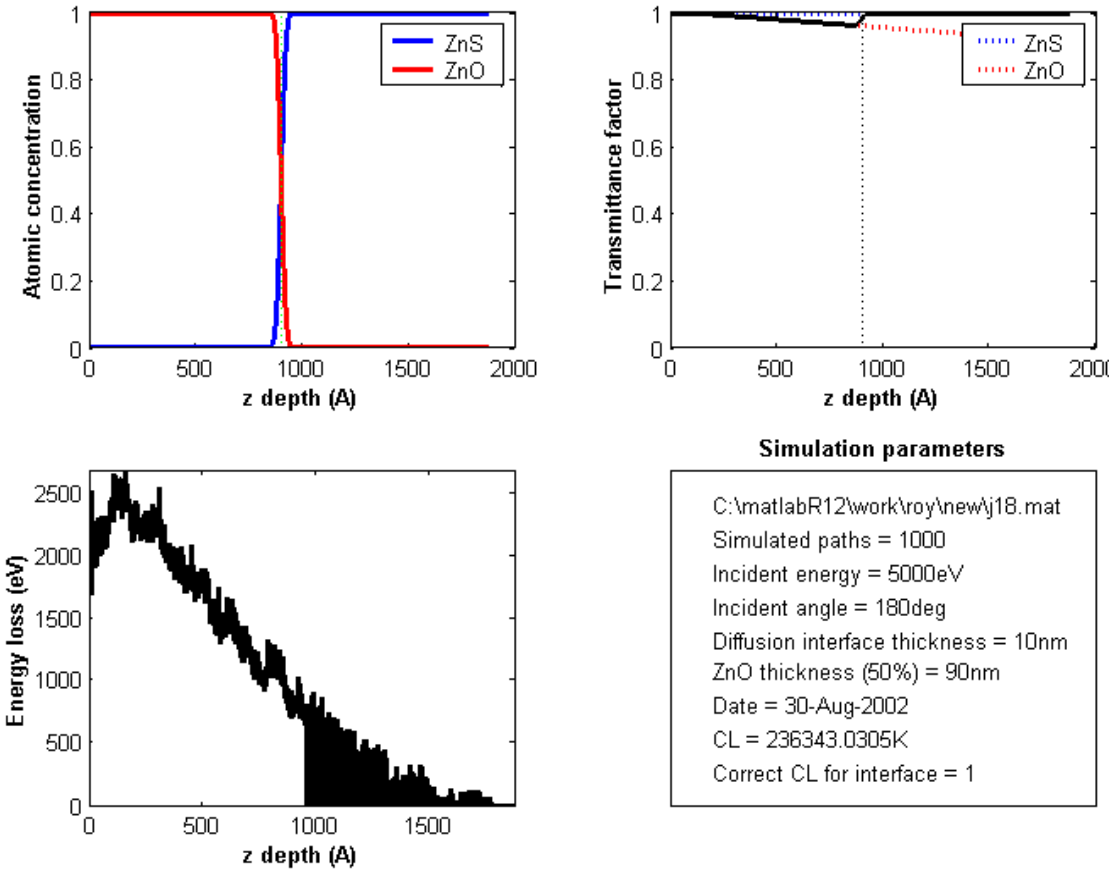

Figure 3.11: The output screen of the Matlab function **cl.m** retrieved from within the command window. In this case the data file containing the previously calculated energy loss profile is j15.mat while the correction "1" indicates that the diffusion interface is assumed to be non-luminescent. In the top left corner of the screen a ZnO/ZnS concentration profile is shown for a 75 nm thick ZnO layer and a 10 nm wide diffusion interface between the ZnO layer and ZnS bulk. The simulation parameters were obtained from the file j15.mat. In the top right window the photon transmittance profile for ZnO and ZnS is shown. The solid line represents the combined transmittance profile according to the ZnO/ZnS concentration profile. Applying the ZnS concentration profile to the energy loss profile shown, eliminates that part of the profile representing energy loss in the ZnO region and the diffusion interface. The remainder of the profile is represented by the shaded area. In the bottom right window the simulation parameters are displayed along with the calculated CL intensity [23].

beam energy on the intensity of the CL from the phosphor powders. With the **gui.m** code 1000 electron trajectories were simulated and the incident angle was set to a value of 180. The incident angle of the electron beam was therefore distributed according to the **distribution.m** [23] subroutine for each simulation performance. The thickness of the diffusion interface was kept at 10 nm between the ZnO and ZnS bulk. The primary electron beam energy was chosen to be 1, 2, 3, 4 and 5 keV. For each selected energy value of the electron beam, the electron trajectory simulation was started from a 5nm thick ZnO layer on the ZnS bulk and gradually increased by stepping up 5 nm each time until the relative CL intensity decreased to zero.

Previous degradation studies [40] showed that the simulated ZnO thickness was comparative to the experimentally measured one when the diffusion interface was set to be non-luminescent. In fact, the formation of the interface itself may lead to the dissociation of all or some of the ZnS and ZnO to their respective atomic species due to the diffusion process. This will result in the interface being totally or partially non-luminescent. The parameter correction was therefore chosen to be the value of 1.

3.3.2 CL simulation with different electron incident angle

The second set of simulations was performed in order to examine the effect of the incident angle of the electron beam on the intensity of the CL from the phosphor powder. Using the code **gui.m** again, 1000 electron trajectories were simulated with 2 keV primary electron beam energy for each simulation performance. The diffusion interface was kept constant at 10 nm. The incident angle was chosen to be 0º, 30º, 60º, 70º and 85º. For each chosen value of the incident angle, the electron trajectory simulation was started again from the 5 nm thick ZnO layer and gradually increased by stepping up 5 nm until the relative CL intensity decreased to zero.

Chapter 4

Degradation in the oxygen ambient

This chapter examines the degradation behavior of ZnS:Cu,Al,Au (P22G) phosphor powder in two types of oxygen ambients. Firstly, a description of the degradation behavior in a water-rich oxygen ambient will be given with a discussion on the change in the CL intensity of the P22G phosphor powder during degradation. Secondly, a description of the degradation behavior in a dry oxygen ambient will be given and will then be followed by a comparison between the degradations in different gas mixtures.

4.1 Degradation in the water-rich oxygen ambient

4.1.1 Degradation behavior

The vacuum chamber was baked for approximately 12 hours after a base pressure of 10^{-9} Torr was achieved by the ion pump. In Figure 4.24 the RGA spectrum shows that there was large amount of water vapour present in the chamber. This was due to the short baking time of the vacuum chamber. To examine the chemical composition of the surface of P22G phosphor, an AES spectrum was recorded and is shown in Figure 4.1.

The spectrum indicates that the surface of P22G phosphor was contaminated with carbon and oxygen layers. According to the ESSCR model, the carbon that is present on the surface influences the degradation behaviour and its role is discussed in more in Section 4.1.3. To remove the contaminants, the surface was sputter-cleaned for about 15 minutes using the argon ion gun whose parameters are given in Table 3.3. Small amounts of Cu were also detected. This is to be expected since the sample holders were fabricated from copper.

The AES spectrum of the sputter-cleaned P22G phosphor that was taken before the

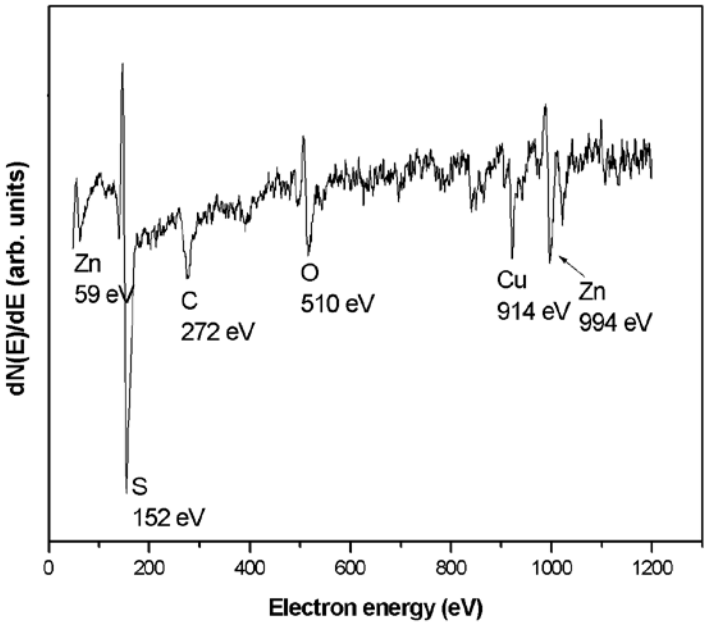

Figure 4.1: AES spectrum of the P22G phosphor sample before the sputter-cleaning.

degradation is shown in Figure 4.2 (a). The carbon and oxygen were almost entirely removed from the surface. The residue present after the sputtering was due to the morphology of the phosphor powder. Since the phosphor is in a powder form, some carbon and oxygen are screened from the sputtering ion beam, see the illustration in Figure 4.3. The Auger peak intensities of sulphur and zinc increase slightly due to the removal of the carbon and oxygen.

The sputter-cleaned P22G phosphor sample was then subjected to electron bombardment at an oxygen gas pressure of 1×10^{-6} Torr. A 2 keV electron beam and an emission current of 10 μA were used. The experimental procedures as mentioned in Section 3.2.1.1 were followed. Figure 4.2 (b) shows a typical AES spectrum after the degradation. The Auger peak-to-peak height (APPH) changes of the P22G phosphor surface during electron bombardment as a function of time is illustrated in Figure 4.4.

By comparing Figures 4.2 (a) and (b), it can be seen that the electron bombardment of the P22G phosphor sample resulted in a decrease in the sulphur Auger peak intensity and an increase in the oxygen peak intensity. The carbon Auger peak disappeared after the electron beam irradiation. The increase in the oxygen Auger peak intensity coincides with the drop in the sulphur peak intensity as shown in Figure 4.4. The

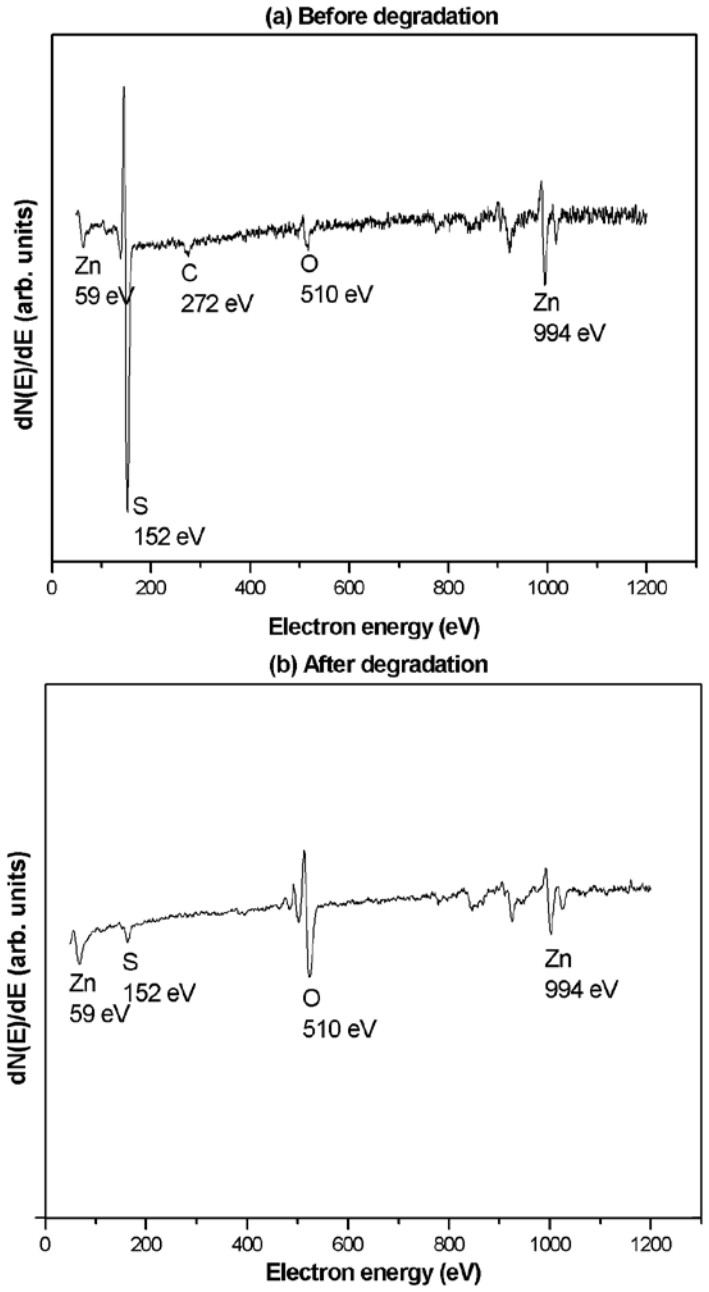

Figure 4.2: AES spectra of the sputter-cleaned P22G phosphor sample (a) before the degradation and (b) after the 100% degradation.

decrease in the sulphur Auger peak intensity was suspended when the electron beam was turned off. When the beam was turned back on again, the sulphur peak intensity started to decrease again. This confirms that the surface reaction of the phosphor is indeed stimulated by the electron beam. As described by the ESSCR model and the Knotek-Feibelman mechanism in Section 2.2, the surface reaction depends on the dissociation of the surface oxygen molecules and the desorption of positive sulphur ions. The number of dissociated oxygen molecules and desorbed positive sulphur ions

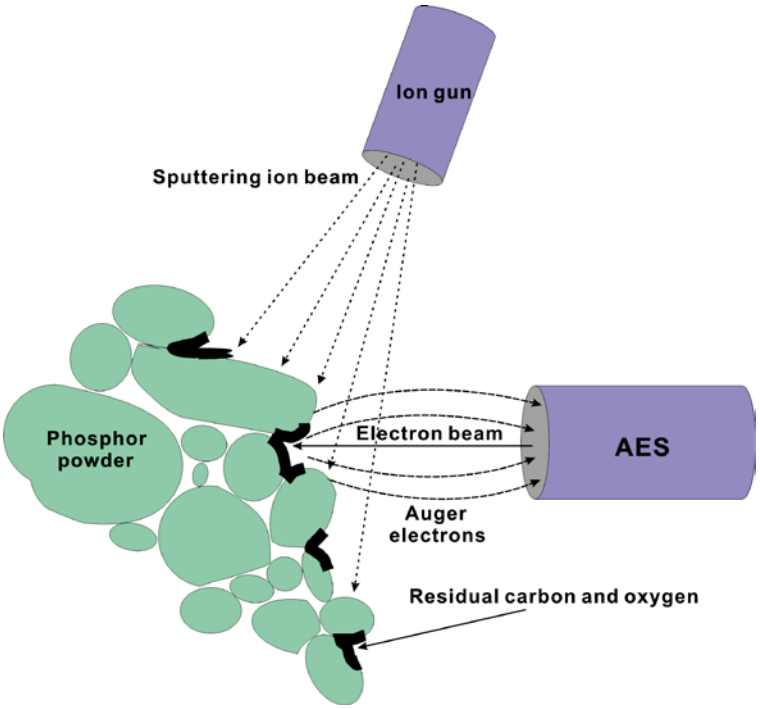

Figure 4.3: Due to the morphology of the phosphor powder, some carbon and oxygen were screened from the sputtering ion beam. Note the analysis area of the AES is much broader than the diameter of the P22G phosphor powder.

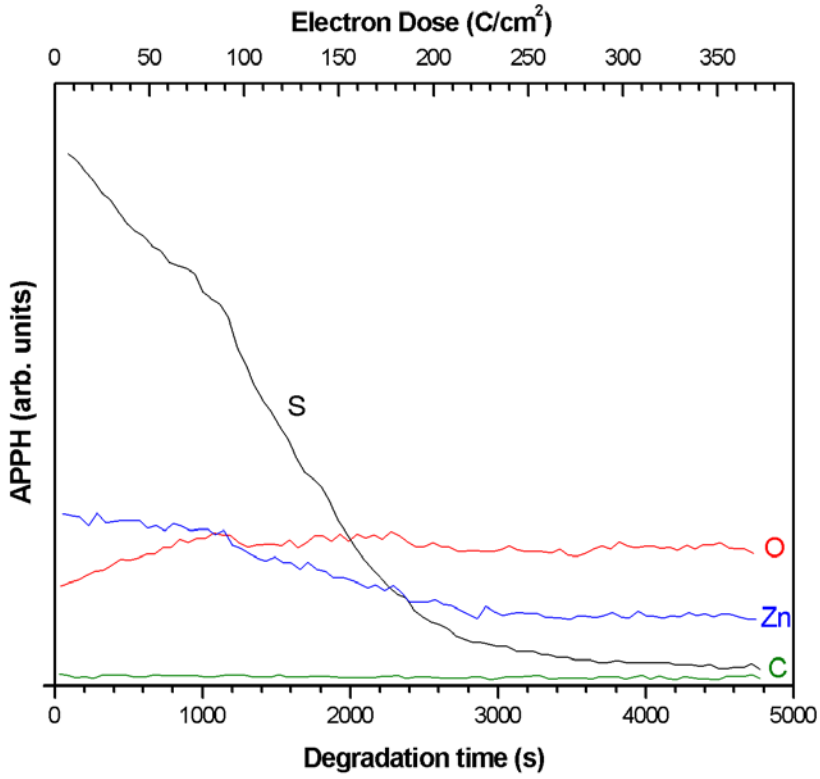

Figure 4.4: The degradation profile of the APPH changes during the electron bombardment as a function of the degradation time (bottom scale) and the electron dose (top scale).

are completely determined by the number of electrons arriving on the surface of the phosphor per unit area. This is called the electron dose (C/cm^2). The degradation profile of the APPHs shown in Figure 4.4 gives more insight if it is calibrated in the electron dose. The following equation can be used to convert degradation time to electron dose:

$$D = \frac{I_e}{A_e} t \tag{4.1}$$

where D is the electron dose, I_e the electron beam current, A_e the beam area and t the degradation time. The term I_e/A_e is the electron beam current density and was calculated to be 0.078 A/cm^2 (see Appendix A). The conversion is therefore simply the value of the beam current density (0.078 A/cm^2) multiplied by the degradation time. The degradation profile of APPHs as a function of the electron dose is also shown in Figure 4.4

According to the APPH changes shown in Figure 4.4, the ZnS phosphor surface was converted into either an oxide (ZnO) or a sulphate ($ZnSO_4$) layer during the electron bombardment as many studies have shown. Swart *et al*. [42] and Oosthuizen *et al* [16] demonstrated by using XPS that ZnO was formed on the ZnS surface when the phosphor was bombarded by an electron beam in oxygen environment. They also detected SO_2 gas generated from the phosphor during the electron exposure. Conversely, Itoh *et al* [19] showed that $ZnSO_4$ was formed on the surface when the ZnS phosphor was irradiated with an electron beam in a water vapor environment. The following are two possible reactions that might take place between the ZnS and oxygen along with the free energies of formation for reactants and products for ZnS [15]:

$$2ZnS + 3O_2 \rightarrow 2ZnO + 2SO_2$$
$$2(-46.04) + 3(0) \rightarrow 2(-83.24) + 2(-70.94), \quad \Delta H = -72.09 \text{ kcal/mol } O_2. \tag{4.2}$$

$$ZnS + 2O_2 \rightarrow ZnSO_4$$
$$(-46.04) + 2(0) \rightarrow (-234.9), \quad \Delta H = -94.43 \text{ kcal/mol } O_2 \tag{4.3}$$

Since ΔH is negative in both cases, it shows that both the formation of ZnO or $ZnSO_4$ is therefore thermodynamically possible.

Although there are two candidates, either a ZnO or $ZnSO_4$ layer, responsible for the formation of the layer on the P22G phosphor surface, it is supposed that the layer formed was ZnO in this instance. The reason for this assumption is that the sulphur Auger peak intensity completely disappeared during degradation as shown in Figure 4.4. Additionally, the decrease in the zinc Auger peak indicates that the ZnO layer formed on the surface might be non-stoichiometric [31]. The zinc concentration in the ZnO layer was lower than in the ZnS bulk.

4.1.2 Chemically-limited oxide formation

As mentioned in the experimental procedures, the P22G phosphor was degraded repeatedly to certain pre-selected percentages. For example, the 60% degradation of sulphur in the APPH implies that sulphur has been degraded to 40% of its initial intensity. Figure 4.5 illustrates these five chosen degradation percentages.

After each degradation was performed, a depth profile of the degraded P22G phosphor sample was obtained by using the ion gun to sputter-clean the degraded surface while measuring an APPH profile. Figure 4.6 show a typical depth profile of the P22G phosphor obtained at 100% degradation. The thickness of the ZnO layer on the surface of the degraded phosphor was measured from the position where sputtering was started to the sputtered depth at which the oxygen level decreased to 50%. The sputtering time through the ZnO layer was 416 seconds for the depth profile shown in Figure 4.6. Due to the removal of the non-stoichiometric ZnO layer from the surface the zinc Auger peak gradually increased in the profile. After the sputter-cleaning, the phosphor was ready for the next degradation study.

The sputtering rate of the ion gun was determined by timing the sputtering through a 400 Å ZnO thin film and was calculated to be 3.9 Å/min. Details of the determination of the sputtering rate are also explained in Appendix A. The thickness of the ZnO layer is therefore calculated by multiplying the sputtering rate with the sputtering time through the oxide. Using these values, it was calculated that a 2.71 nm thick ZnO

layer was formed on the surface of the P22G phosphor after 100% degradation.

For each pre-selected degradation percentage, the degradation was performed at least

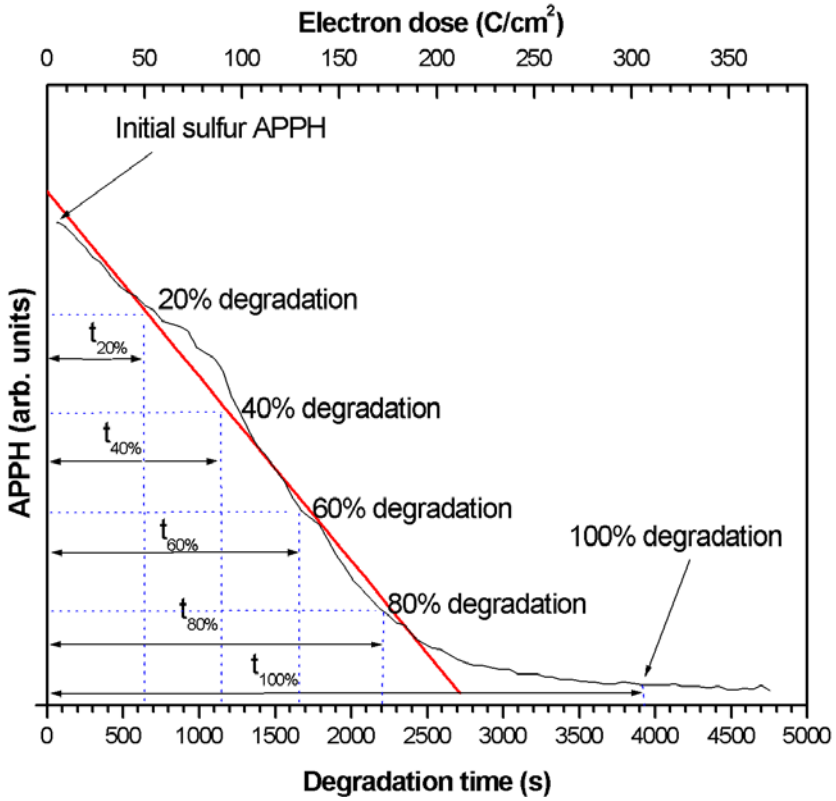

Figure 4.5: This diagram illustrates the degradation percentages and the time taken for each degradation percentage to be completed. The S APPH is the S APPH value of the degradation profile in Figure 4.4.

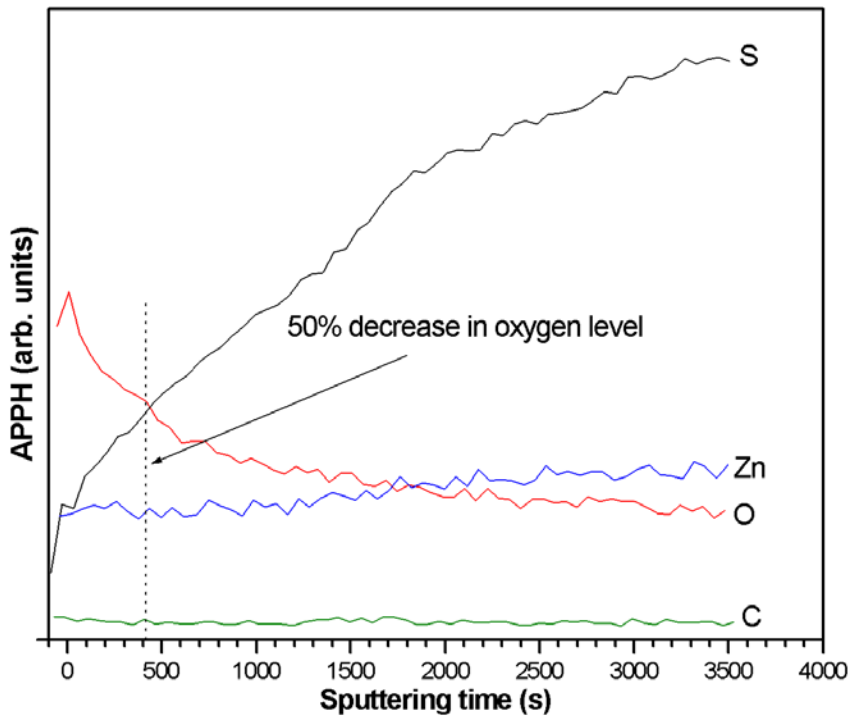

Figure 4.6: A depth profile of the P22G phosphor obtained at 100% degradation. The sputtering time through the ZnO layer was 416 s.

Degradation percentage (%)	***Degradation time (s)***	***ZnO thickness (nm)***	***Average ZnO thickness (nm)***
20	$t_{20\%}$ = 610	0.78	**1.01 ± 0.17**
		1.12	
		1.14	
40	$t_{40\%}$ = 1130	1.50	**1.22 ± 0.28**
		1.20	
		0.96	
60	$t_{60\%}$ = 1670	1.66	**1.51 ± 0.15**
		1.35	
80	$t_{80\%}$ = 2200	1.82	**1.82 ± 0.01**
		1.81	
100	$t_{100\%}$ = 3930	2.80	**2.76 ± 0.05**
		2.71	

Table 4.1: A summary of the experimental results.

twice in order to confirm experimental evidence. The thickness of the ZnO layer

formed on the surface of the P22G phosphor was determined after each degradation and the values are given in Table 4.1. The time taken to complete the degradation for each chosen percentage was determined as shown in Figure 4.5. Figure 4.7 shows the degradation percentage versus the average ZnO thickness, and Figure 4.8 shows the ZnO thickness versus the degradation time.

As is shown in Figure 4.7, the depletion of sulphur from the surface of the P22G phosphor was proportional to the growth of the ZnO until 80% degradation during electron bombardment. The deviation after 80% degradation can easily be explained if the limitation of the AES surface technique is understood. AES has an analysis depth of about 2nm [43] but a 1.82 nm thick ZnO layer was formed on the surface of the P22G phosphor after 80% degradation. Therefore when the 80% degradation was exceeded, AES only detected a weak sulphur Auger peak intensity that decayed exponentially from the surface (see Figure 4.5). The conversion of ZnS to ZnO was evident and continued linearly with time as illustrated in Figure 4.8.

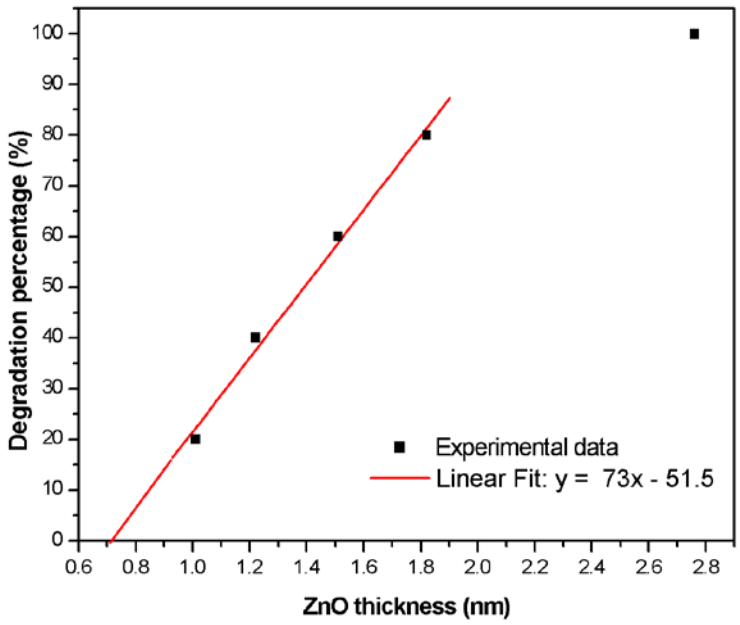

Figure 4.7: The graph of degradation percentage plotted against the thickness of the ZnO layer.

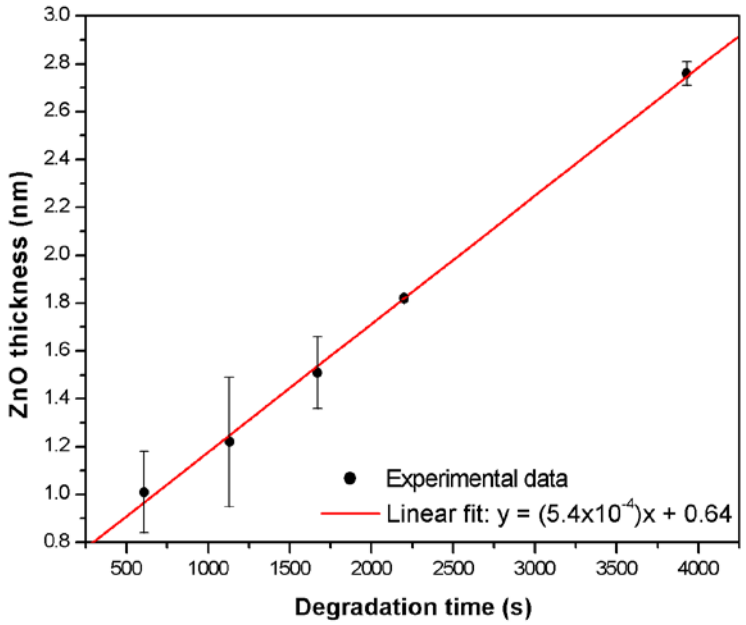

Figure 4.8: The graph of the ZnO thickness plotted against the degradation time.

The linear relationship in Figure 4.8 shows that the ZnO layer formed on the P22G phosphor in the water-rich oxygen ambient is a result of a chemically-limited reaction. In general, the chemically-limited surface reaction can be expressed as

$$X(t) = kt \tag{4.4}$$

where $X(t)$ is the thickness of the oxide layer, k the rate constant that depends on the experimental conditions, e.g. temperature of the phosphor surface [41] and oxygen pressure of the system [44,45], and t is the degradation time. The linear fit is also shown in Figure 4.8.

4.1.3 CL measurements

The AES and CL measurement were simultaneously collected from two personal computers as outlines in the experimental procedure in Section 3.2.1.2. The P22G phosphor was degraded at a water-rich oxygen pressure of 1×10^{-6} Torr without sputter-cleaning the surface since the ion sputtering severely influences the CL intensity [15]. Figure 4.9 shows the AES spectra of the P22G phosphor before and after the degradation. The degradation profile of the change in APPH of the phosphor surface and the CL spectrum are shown in Figure 4.10 and 4.11.

As shown in Figure 4.9, the sulphur Auger peak decreased during electron beam irradiation and this coincided with an increase in the height of the oxygen peak. The adventitious carbon present on the surface disappeared during electron irradiation. In

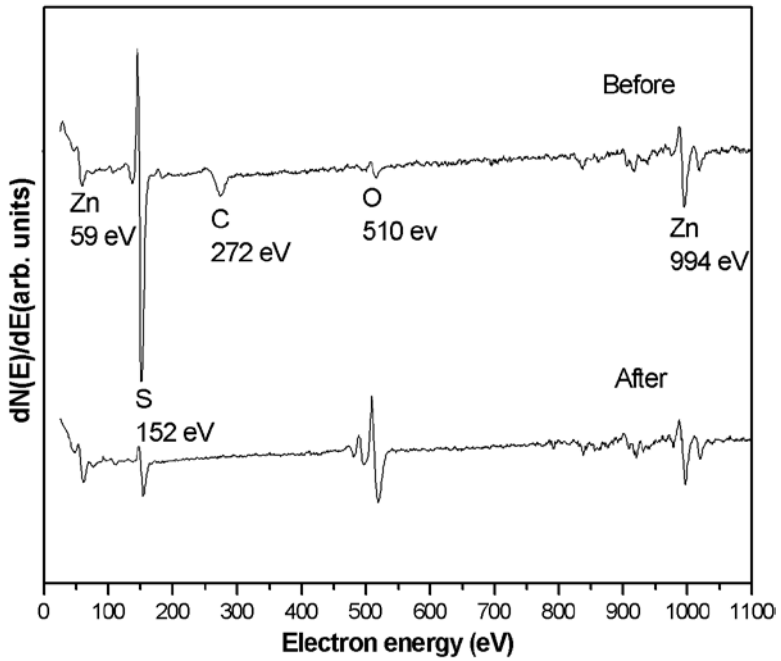

Figure 4.9: AES spectra before and after the degradation of the P22G phosphor that were not sputter-cleaned.

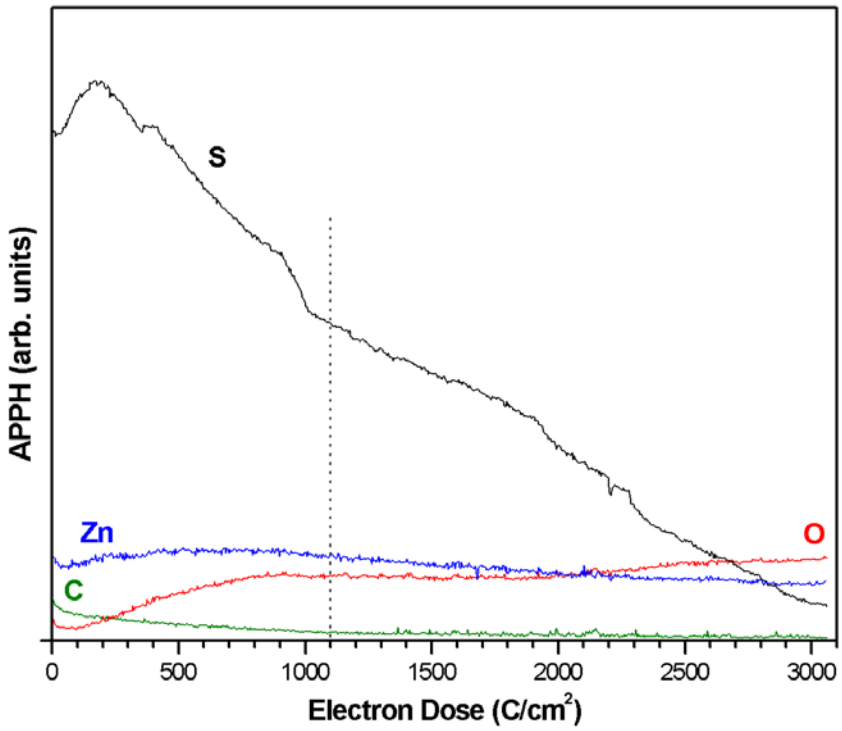

Figure 4.10: The degradation profile of the APPH changes on the surface of the P22G phosphor during the electron bombardment .

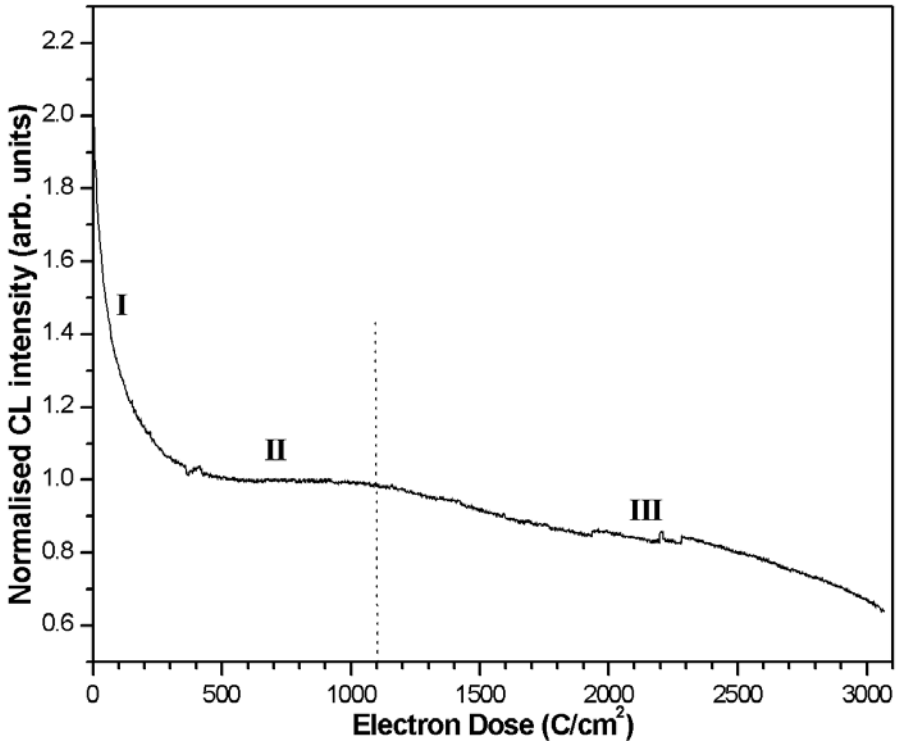

Figure 4.11: The CL intensity as a function of electron dose.

Figure 4.10 the carbon APPH decreased exponentially as soon as the surface was

exposed to the electron beam. Most of the carbon was removed from the surface at an electron dose of about 1100 C/cm^2. Initially the sulphur APPH increased to a certain maximum value due to the quick removal of carbon from the surface. After a while it decreased almost steadily once the carbon had been removed from the surface. The oxygen APPH increased during the electron beam irradiation.

The spectral distribution of the CL emission of the P22G phosphor is shown in Figure 3.6. The CL spectrum of the P22G phosphor is characterised by a Gaussian distribution with the maximum peak height at 530 nm. A graph of the relative CL intensity (530nm) plotted against the electron dose in a water-rich oxygen pressure of 1×10^{-6} Torr is shown in Figure 4.11. The CL intensity was normalised with respect to the intensity in region II. Initially, there was a rapid drop in CL intensity in region I. This was due to the initial surface charging by the electron beam as demonstrated by Swart *et al*. [42]. The surface charging would increase the probability for the electron-hole pair to be swept apart before recombination (see Figure A.1). Consequently, there would be a loss in the CL intensity. As indicated in Figure 4.9, there are no peak shifts between the AES spectra which implies that the charging effects on the phosphor surface disappeared at the end of the degradation. The charging effects gradually diminished in region II [42] and the CL intensity remained constant until the electron dose was about 1100 C/cm^2. By comparing Figures 4.10 and 4.11 it is apparent that the constant CL intensity in region II was due to the removal of the carbon from the surface by an electron stimulated process. After the removal of carbon from the surface, the CL intensity decreased again in region III but at a slower rate compared to region I.

Since there was no carbon present on the phosphor surface in region III, the degradation of the phosphor behaved like that of the sputter-cleaned sample. As discussed in Section 4.2 and shown in Figure 4.7, the rate at which the sulphur APPH decreased was proportional to the formation of the ZnO layer on the surface until the thickness of the growing ZnO layer exceeded the analysis depth of the AES. However, the CL intensity decreases linearly with the sulphur APPH in region III as indicated in Figure 4.12. Therefore the diminishing rate of the CL intensity in region III was also proportional to the thickness of the ZnO layer formed on the P22G phosphor surface

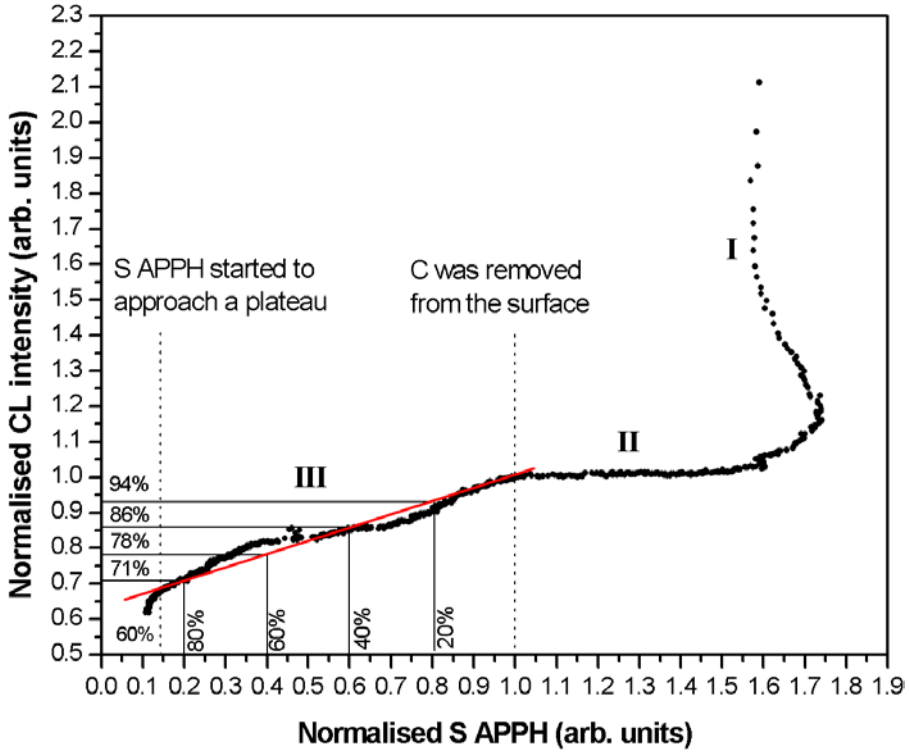

Figure 4.12: The graph of the normalised CL intensity plotted against normalised S APPH. S APPH is normalised with respect to the value where the surface carbon was removed. The graph shows a linear relationship between two dash lines. The degradation percentage of the S APPH corresponding to the decrease percentage in CL intensity is also shown.

during the electron beam bombardment. Due to the fact that electrons loose a fraction of their energy in the oxide layer during penetration, the fraction of energy loss in the phosphor bulk decreased. The CL is dependent upon the energy loss in the phosphor and therefore the growth of the oxide layer significantly decreases the CL intensity.

As indicated in Figure 4.12, the graph decreases rapidly after region III. This is because the thickness of the growing ZnO layer exceeded the analysis depth of the AES. The sulphur APPH started to approach a plateau, but the CL intensity continued to diminish due to the ZnO layer that was still growing.

4.2 Degradation in the dry oxygen ambient

4.2.1 Degradation behavior

The vacuum chamber was baked for more than 72 hours at the base pressure of

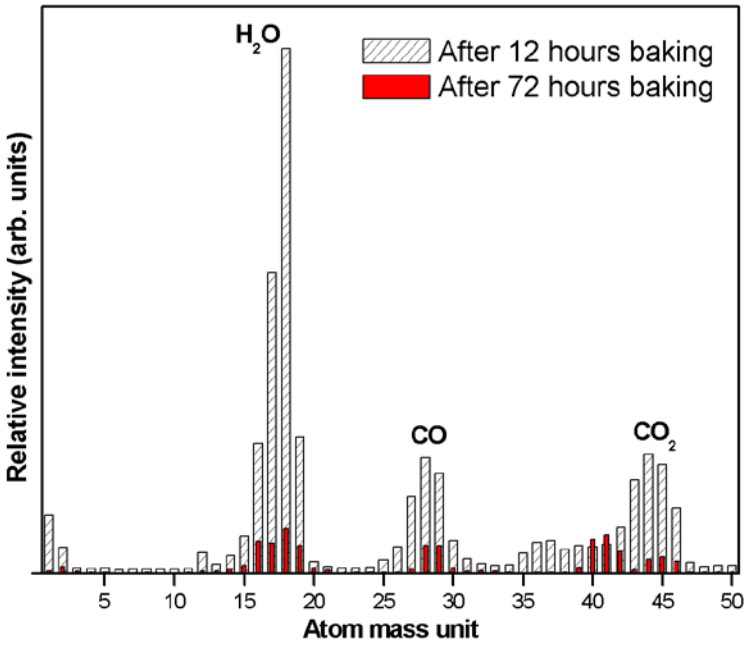

Figure 4.13: RGA spectra measured at base pressure after several hours of baking. The prolonged baking removed the various gases, e.g. water vapour, from the vacuum chamber.

3×10^{-9} Torr. This prolonged baking ensured that almost all water vapour was removed from the chamber. This is confirmed by the RGA spectra measured at base pressure in Figure 4.13. The P22G phosphor powder was again exposed to a 2 keV electron beam with a beam current density of 78 mA/cm^2 at the oxygen pressure of 1×10^{-6} Torr. A RGA spectrum measured at this oxygen pressure is shown in Figure 4.24 (d). The AES spectrum of the sputter-cleaned P22G phosphor sample before degradation is shown in Figure 4.14 (a) There was still some oxygen present on the surface of the phosphor but there were no significant signs of carbon. In Figure 4.14 (b) the P22G phosphor was degraded to 100% in the dry oxygen ambient. The electron irradiation of the P22G phosphor caused a decrease in the sulphur Auger peak and an increase in the oxygen peak.

Figure 4.15 shows the degradation profile of the change in APPH of the P22G phosphor surface during the electron bombardment in the dry oxygen ambient as a function of the degradation time (bottom scale) and the electron dose (top scale). The oxygen Auger peak intensity increased during the electron exposure, but the sulphur peak intensity decreased exponentially with time and started to approach a plateau at about 3300 C/cm^2 electron dose. At this plateau, the sulphur APPH dropped to 22% of

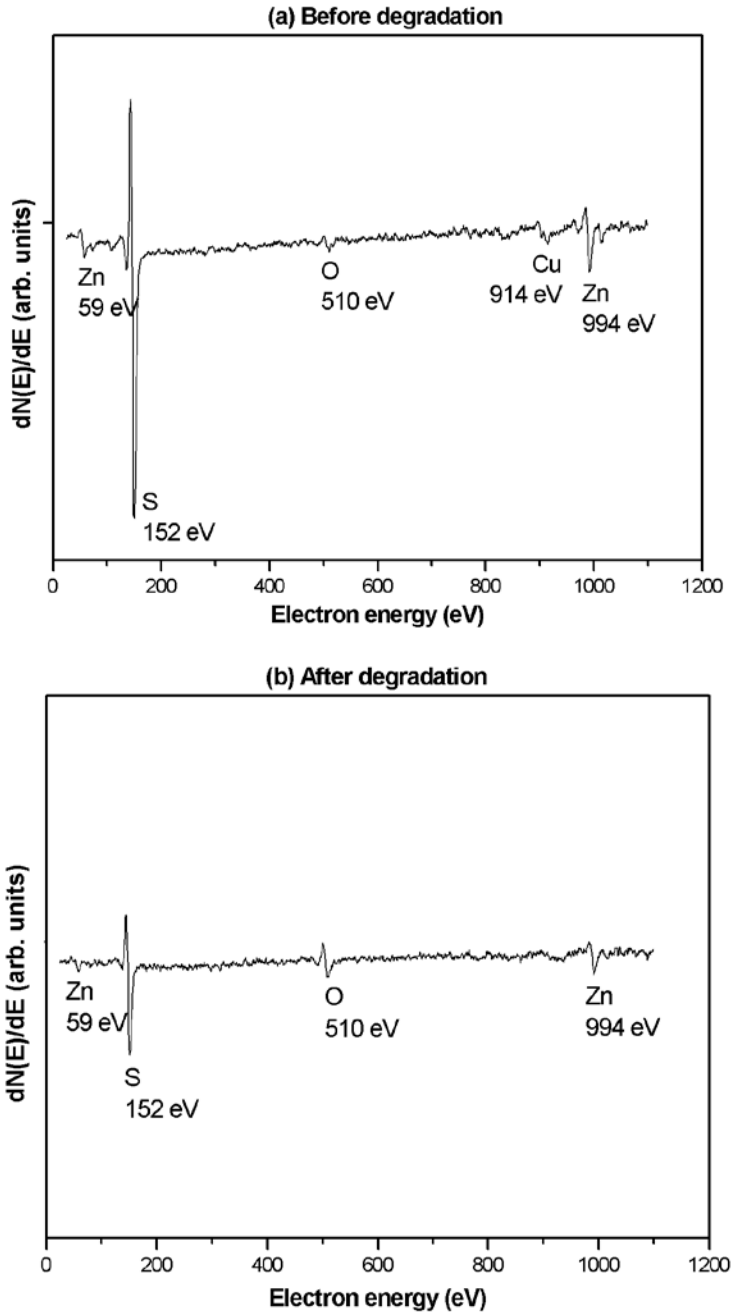

Figure 4.14: AES spectra of the P22G phosphor sample (a) before the degradation and (b) after 100% degradation in the dry oxygen ambient.

its initial APPH as indicated in Figure 4.16.

By comparing the AES spectra and APPH profiles of the degradations performed in the water-rich and dry oxygen ambient, the difference in the degradation mechanism is evident. Figure 4.16 shows the comparison of the APPH changes of the sulphur on the P22G phosphor surface the during electron bombardment in a water-rich and dry

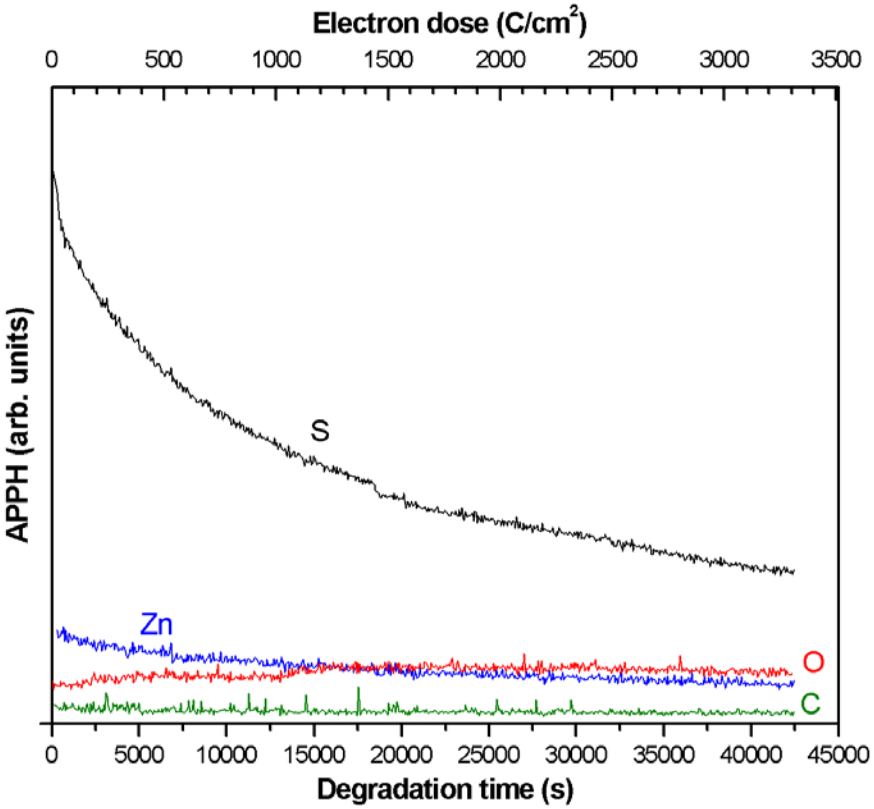

Figure 4.15: The degradation profile of the APPHs changes of S, O, Zn and C during the electron bombardment in the dry oxygen ambient as a function of time (bottom scale) and electron dose (top scale).

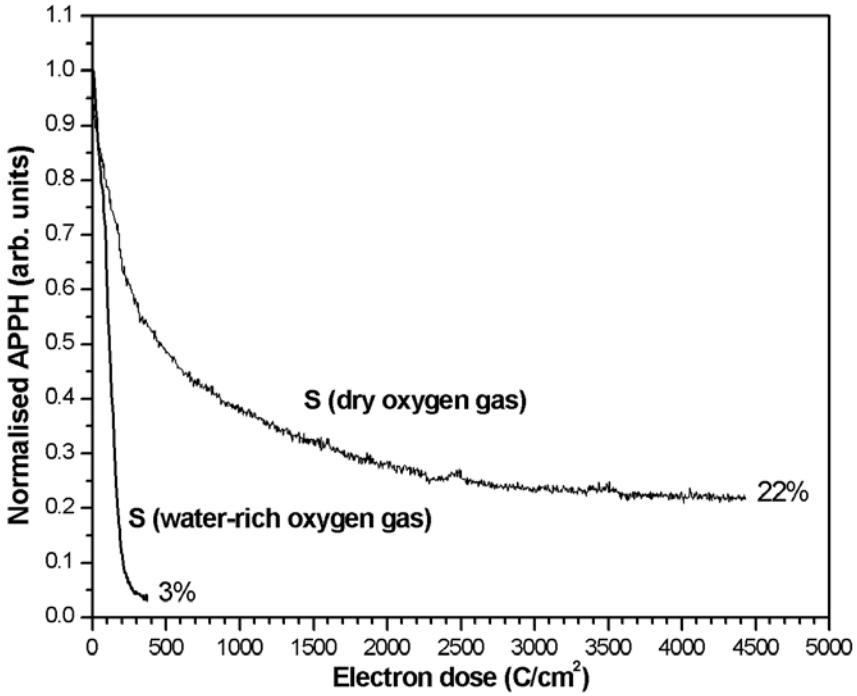

Figure 4.16: The APPH changes of S measured during the electron bombardment in the water-rich and dry oxygen ambient as a function of electron dose.

oxygen ambient. In the water-rich oxygen ambient, the sulphur APPH decreased linearly with time until a plateau was reached at which the sulphur APPH dropped to 3% of its initial APPH value. After the degradation, a small sulphur Auger peak appeared in the AES spectrum (see Figure 4.2 (b)). These results indicate that sulphur was almost absent from the P22G phosphor surface after the degradation in the water-rich oxygen ambient. In the dry oxygen gas the sulphur APPH decayed exponentially with time and eventually reached a plateau. Sulphur APPH was almost stable at the plateau at which it dropped to 22% of its initial APPH value. Therefore sulphur was still present on the P22G phosphor surface after the degradation in a dry oxygen ambient. The sulphur Auger peak in the AES spectrum (see Figure 4.14 (b)) measured after the degradation is the proof of this.

According to the degradation profile in Figure 4.15, a chemical reaction was taking place on the surface of the P22G phosphor during the electron bombardment in the dry oxygen ambient. As mentioned before, there are two types of layers that might be formed on the surface of the ZnS phosphors as suggested by many researchers, viz. ZnO and $ZnSO_4$. It has been deduced that the ZnO layer was formed on the P22G phosphor surface after the degradation in the water-rich oxygen ambient. Conversly, a $ZnSO_4$ layer was formed when degrading in the dry oxygen ambient because of the presence of sulphur on the surface of the P22G phosphor. It will be shown in the next section that the sulphur Auger peak originated from the $ZnSO_4$ layer, and not from the ZnS bulk.

4.2.2 Sulphate formation by diffusing charged particles

The P22G phosphor was again repeatedly degraded to the five pre-selected degradation percentages, namely, 20%, 40%, 60%, 80% and 100% degradation. The method for determining the degradation percentage differ slightly here from the previous one, since the degradation behavior of sulphur APPH is different from that degraded in the water-rich oxygen gas. The 100% degradation was defined as the decrease of the sulphur APPH from its initial value to the value just before the plateau, e.g. Figure 4.15. 80% degradation implies 80% decrease in the difference between the initial sulphur APPH value and the value just before the plateau was reached. Figure 4.17 illustrates these five chosen degradation percentages and the

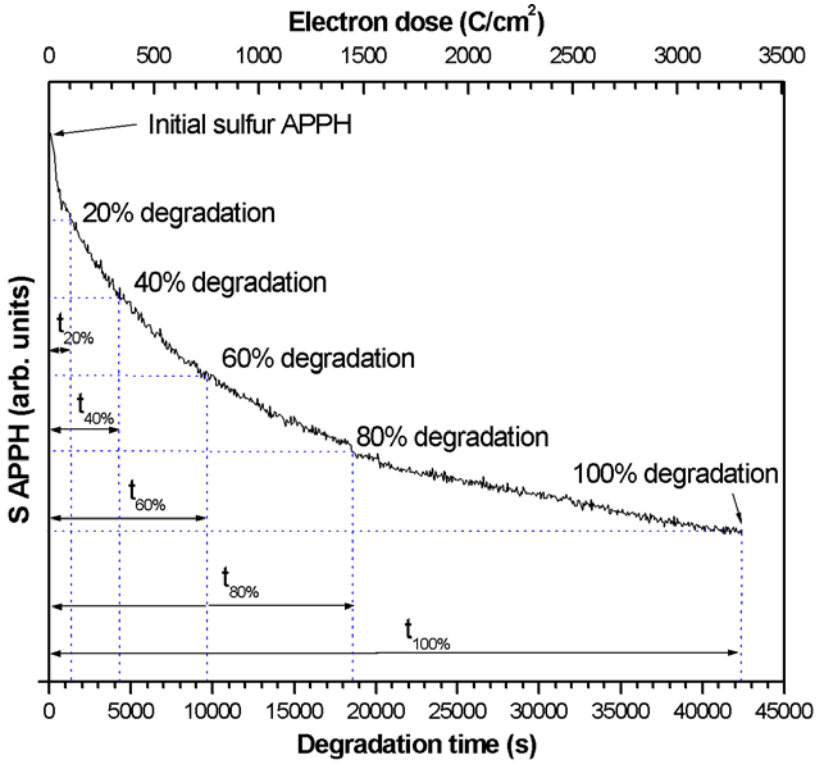

Figure 4.17: This sketch illustrates the degradation percentages and the degradation time taken for each degradation percentage to be completed. The S APPH is the S APPH value of the degradation profile of Figure 4.14.

degradation time.

The depth profile of the degraded P22G phosphor sample was obtained after each degradation was performed. The experimental parameters for the ion gun used were the same values as given in Table 3.3. The thickness of the sulphate layer on the surface of the degraded phosphor were measured again from the position where sputtering was started to the sputtered depth at which the oxygen level decreased to 50%. Figure 4.18 shows the depth profile of the P22G phosphor after 100% degradation. The sputtering time through the sulphate layer was measured to be 1460 seconds and the thickness of the layer was calculated to be 9.49 nm.

In the depth profile of Figure 4.6, the oxygen APPH decreased sharply at the beginning of the sputtering. The oxygen concentration was higher at the surface of the degraded P22G phosphor. However, the oxygen APPH in the depth profile of Figure 4.18 shows a gradual decrease. Similarly, the sulphur APPH increased gradually when

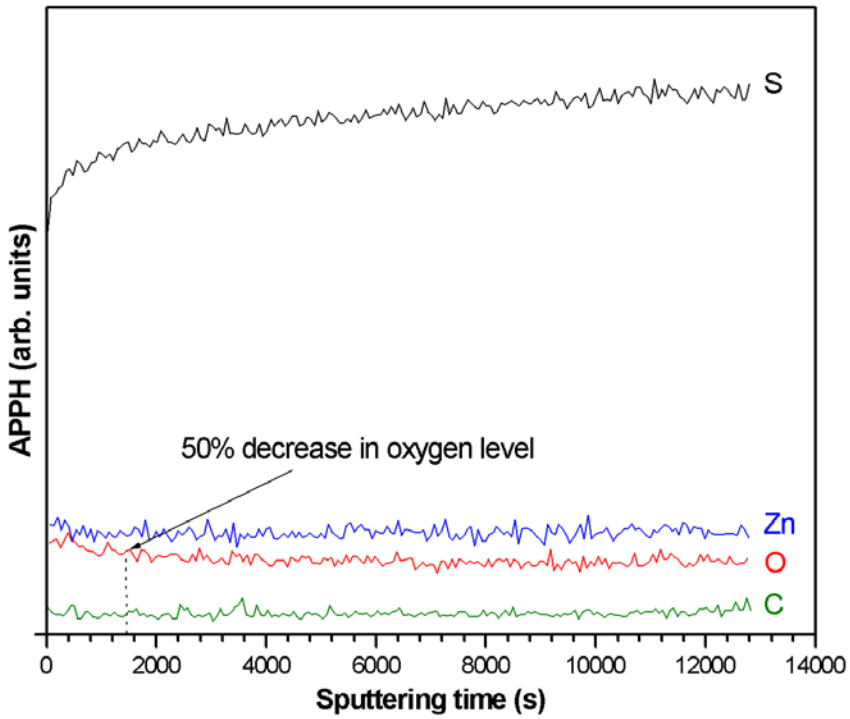

Figure 4.18: The depth profile of the P22G phosphor after 100% degradation in dry oxygen ambient. The sputtering time through the sulphate layer was 1460s.

Degradation percentage (%)	***Degradation time (s)***	***$ZnSO_4$ thickness (nm)***	
20	$t_{20\%}$ =1 200	**3.38**	
40	$t_{40\%}$ = 4200	**4.88**	
60	$t_{60\%}$ = 9800	6.50	**6.34 ± 0.16** (average)
		6.18	
80	$t_{80\%}$ = 18900	**7.67**	
100	$t_{100\%}$ = 42500	**9.49**	

Table 4.2: The summary of the experimentally measured thicknesses of the $ZnSO_4$ layer for the P22G phosphor exposed to different degrees of degradation in the dry oxygen ambient. The degradation time is determined as indicated in Figure 4.16. The same sputtering rate through the sulphate layer was used as for the ZnO case.

compared to the sulphur APPH in Figure 4.6.

The experimentally measured thicknesses of the growing layer of the P22G phosphor exposed to different degrees of the degradation in dry oxygen ambient are given in Table 4.2. All values for the thickness of each growing layer are over 3 nm in Table 4.2, but the AES technique has an analysis depth of about 2 nm as previously mentioned. Therefore, if there was a ZnO layer (>2nm) formed on the top of the phosphor, the sulphur Auger peak cannot originate from the ZnS bulk which was more than 2 nm deep under the surface. Hence, the sulphur Auger peak should be weak or absent from the AES spectrum. This is not the case and therefore it is insisted that the growing layer is $ZnSO_4$ and that the detected sulphur Auger peak originated from this layer. The presence of $ZnSO_4$, however, still has to be confirmed with XPS.

Figure 4.19 shows a plot of the degradation percentage against the thickness of the sulphate layer. It shows again the linear relationship as illustrated in Figure 4.7. The depletion of the sulphur from the surface of the P22G phosphor was proportional to the growth of the sulphate layer before the sulphur APPH reached the plateau. Figure 4.20 is a graph of the thickness of $ZnSO_4$ as a function of time. The growth of the sulphate layer shows an exponential decay with time and therefore the sulphate formation is not chemically-limited as in the case of the ZnO.

From Figure 4.20 one might intuitively expect that growth of the $ZnSO_4$ would be a diffusion-limited reaction. Initially, the chemical reaction took place on the phosphor surface to form a sulphate. When the sulphate layer becomes thicker, the diffusion of the reactants through the sulphate layer start to support the reaction at the reaction interface. If the chemical reaction at the surface is very rapid compared to the diffusion process, the formation of the sulphate will be diffusion-limited. Assume that the uncharged particles were involved in the diffusion through the sulphate layer to the reaction interfaces, the growth rate of the sulphate is predicted by the parabolic growth law:

$$X(t) = (\sqrt{2D})t^{1/2} \qquad (4.5)$$

where $X(t)$ is the thickness of the sulphate as a function of time, D is the diffusion

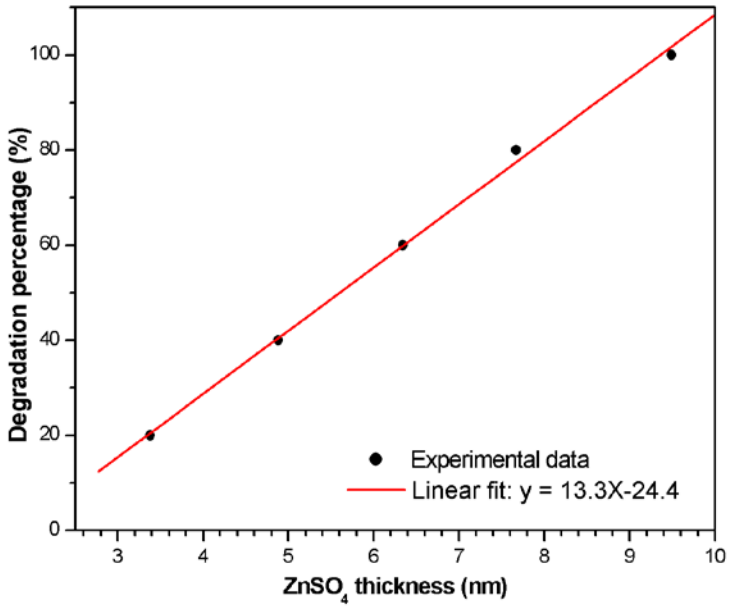

Figure 4.19: The graph of the degradation percentage plotted against the sulphate thickness.

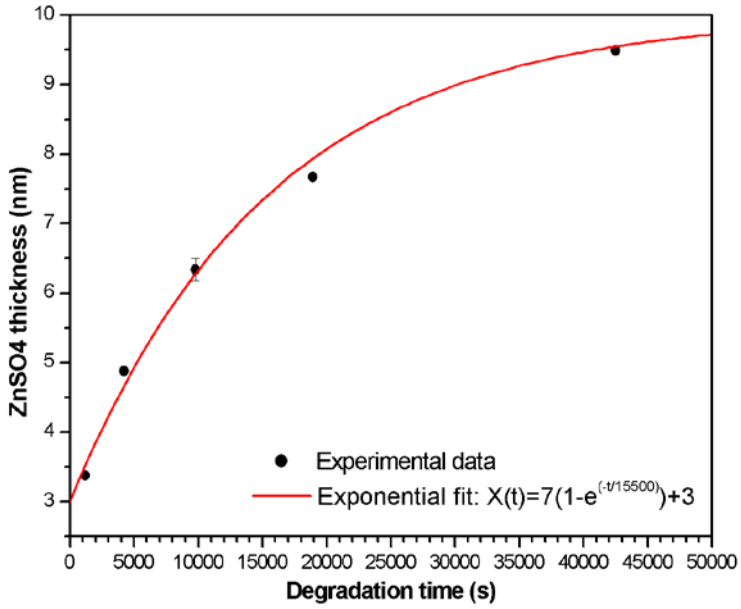

Figure 4.20: The graph of the $ZnSO_4$ thickness as a function of the degradation time.

coefficient and *t* is the time. Figure 4.21 shows a graph of the $ZnSO_4$ thickness against the square root of the degradation time. The result shows that the experimentally measured $ZnSO_4$ thickness does not fully obey the parabolic growth law.

According to the Knotek-Feibelman mechanism (see Figure 2.4), positive sulphur was continuously generated from the ZnS phosphor by the electron beam. This positive

sulphur weakened its partially ionic bonds to the surrounding positive zinc.

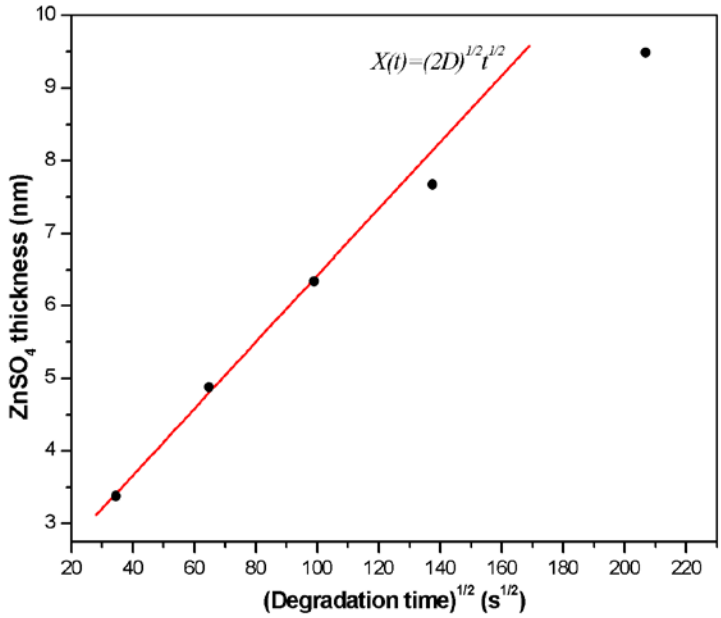

Figure 4.21: The graph of the $ZnSO_4$ thickness plotted against the square root of the degradation time.

Consequently, the positive sulphur could be easily desorbed and left surrounding cations. Both positive sulphur and zinc would therefore diffuse according to their concentration gradient in the $ZnSO_4$/ZnS system. As indicated in Table 5.1, a 2 keV electron beam has a maximum penetrating depth of about 65 nm, hence the Knotek-Feibelman mechanism would possibly take place underneath the sulphate layer. Secondly, the oxygen molecules near the phosphor surface were dissociated and ionised by the electron beam. These negative oxygen particles (O^-) at the surface would diffuse through the sulphate layer to the inner reaction interface. Figure 4.22 shows the possible charged particles involved in the diffusion process. The diffusion of the reactants through the sulphate film would therefore be charged particles, not neutral atoms.

Because of the diffusion of the charged species, a non-uniform charge distribution is established. This non-uniform charge distribution provides a force on the diffusing charged-species which is in addition to the net effect produced by the concentration gradient. This electrostatic force may enhance or retard the rate of diffusion, depending on the direction of the electric field and the sign of the charge of the diffusing species. As indicated in Figure 4.21, the thickness of the sulphate formed by

the diffusing charged particles has smaller values than the diffusing neutral atoms.

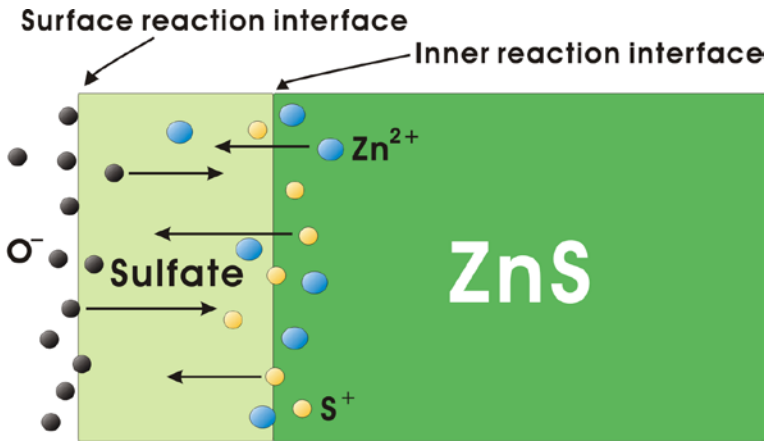

Figure 4.22: The formation of sulphate may happen at two reaction interfaces by either diffusing positive sulphur and zinc to the surface reaction interface or diffusing negative oxygen to the inner interface.

This implies that the averaged electrostatic force retards the diffusion of the charged particles.

As shown in Figure 4.20, the electron stimulated surface chemical degradation in dry oxygen ambient was predicted to be limiting-thickness exponential and described by the following formula [46]:

$$X(t) = X_{\infty}(1 - e^{(-t/\tau)}) \tag{4.6}$$

where X_{∞} is the maximum thickness of the $ZnSO_4$ layer formed on the phosphor surface, t the degradation time and τ the decay constant. The parameters in Equation 4.6 depend on the concentration of the charged particles that influence charge distribution in the system. Hence, the experimental parameters that affect the concentration of the charged particles, e.g. magnitude of the electron beam current density and the oxygen pressure, might vary the value of the parameters in Equation 4.6. The values of the parameters, that fit the data are shown in Figure 4.20. An additional value of 3 nm was added to the exponential curve in order to fit the data.

4.3 Comparison of the degradation in gas mixtures

The sputter-cleaned P22G phosphor sample was bombarded by an electron beam in two gas mixtures. The electron beam of the same energy 2 keV and beam current density 78 mA/cm^2 were used. Since the degradations were also performed in the dry environment of the vacuum chamber (>72 hours baking), the influence of water vapour on the degradation was minimal. The first gas mixture consisted of oxygen, carbon monoxide and argon. The second gas mixture consisted of oxygen and carbon monoxide. One of the degradation studies of P22G phosphor was performed in argon gas.

When the degradations were performed in the gas mixtures or in argon gas, the total pressure was maintained at 1×10^{-6} Torr and the partial pressures of the various gases were measured using the residual gas analyser. Both degradation performance and RGA measurement were done when the various gases in the mixture were stable. Figure 4.23 shows the comparison of the sulphur APPH changes on the surface of the P22G phosphor degraded by the electron beam in the different gas mixtures and argon gas. The sulphur APPH change of the P22G phosphor degraded in the dry oxygen

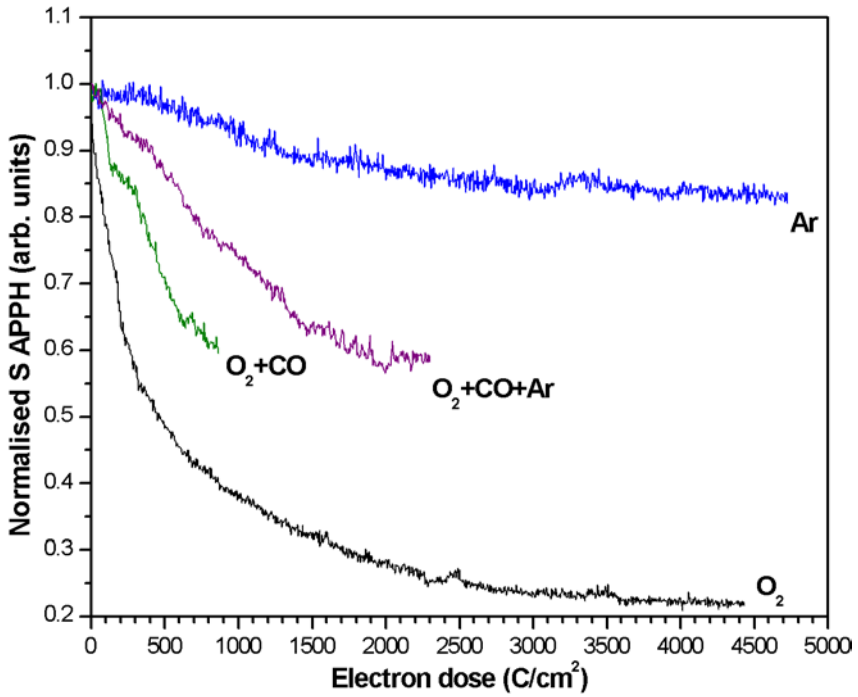

Figure 4.23: The S APPH changes on the surface of the P22G phosphor degraded by the

electron beam in the different gas mixtures, argon gas and oxygen gas.

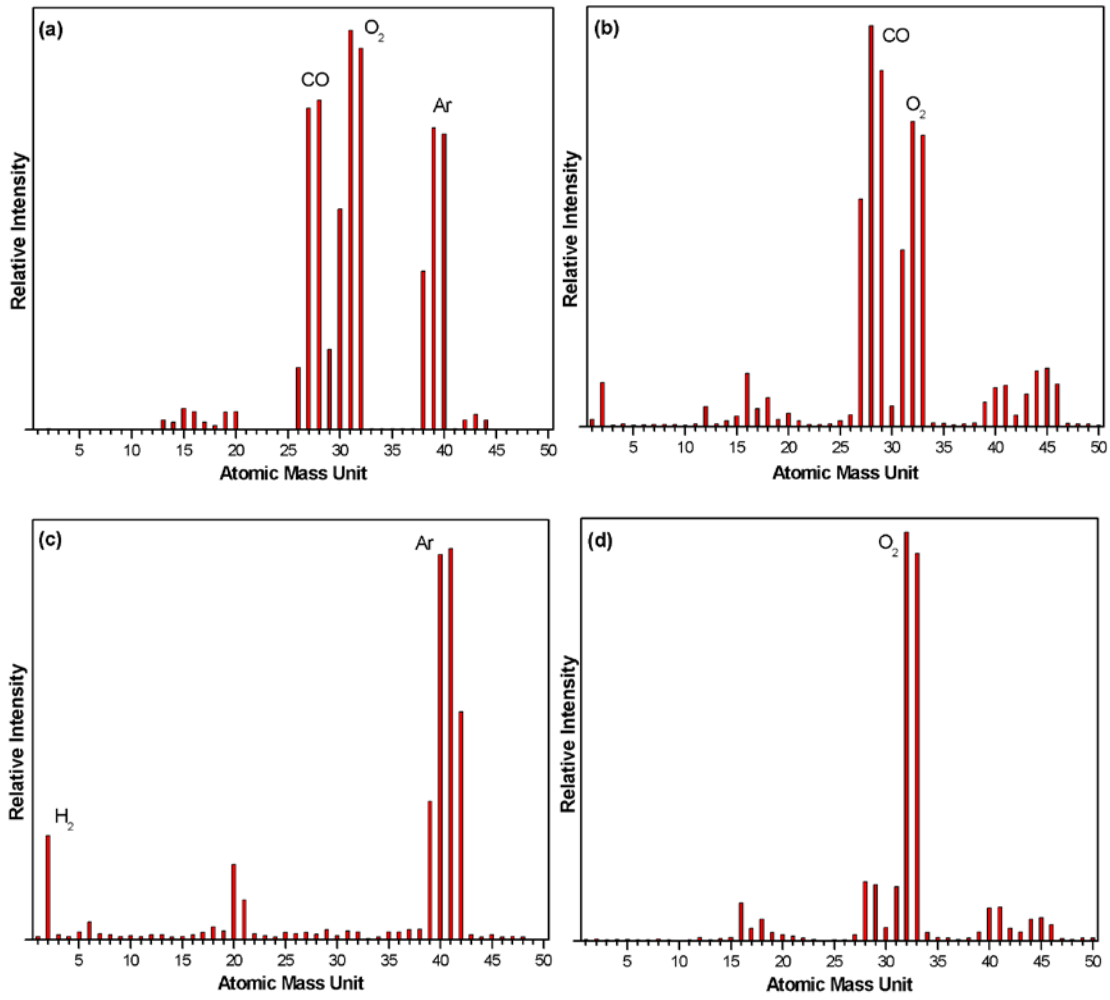

Figure 4.24: RGA spectra (0-50 atomic mass unit) of (a) the oxygen, carbon monoxide and argon gas mixture, (b) the oxygen and carbon monoxide gas mixture, (c) argon gas and (d) oxygen gas. As indicated in the spectra, the water peak is minimal as a result of prolonged baking.

ambient is also plotted in Figure 4.23. The RGA spectra for the gas mixtures, argon gas and oxygen gas are shown in Figure 4.24 (a)-(d).

The sulphur APPHs of the electron bombarded P22G phosphor decreased in four different ambients as shown in Figure 4.23. As discussed in the previous chapter, the decrease in the sulphur APPH during the electron bombardment was due to the conversion of the surface ZnS into the $ZnSO_4$ layer. The non-luminescent $ZnSO_4$ layer therefore degraded the efficiency of the phosphor. Hence, the decrease in the sulphur APPH can be the criterion for the degradation in the efficiency of the P22G phosphor. The P22G phosphor was degraded severely in the oxygen ambient because of the rapid decrease in the sulphur APPH. The degradation rate of the phosphor was slow in the argon ambient and intermediate in the two gas mixtures.

Hillie *et al.* [41] showed that the P22G phosphor was also degraded in the carbon dioxide ambient. Darici *et al.* [47] proposed that the elemental carbon is deposited on the phosphor surface during the degradation in the carbon dioxide gas. It is possible that this can also happen for the degradation performed in the carbon monoxide gas. According to the ESSCR model, the gas molecules near the phosphor surface are dissociated into atomic species by the electron beam. Thus the carbon monoxide molecules near the phosphor surface were split into its elemental atoms. Oxygen caused the surface chemical reaction and carbon was deposited on the surface as shown in Figure 4.25. As shown in the degradation profile of Figure 4.10, the degradation of the sulphur APPH was started after most of the surface carbon was removed. In the gas mixture of oxygen and carbon monoxide the surface carbon deposited by splitting carbon monoxide molecules therefore retarded the degradation.

In the gas mixture of oxygen, carbon monoxide and argon gas the sulphur APPH decreased even more slowly than in the previous mixture. Carbon was also detected by AES after the degradation. The depositing carbon layer led to a slow degradation rate. Secondly, additional argon gas was added into the chamber. Argon gas was competing with oxygen molecules to occupy the phosphor surface. The surface oxygen concentration was therefore lowered and caused a slower surface chemical

reaction.

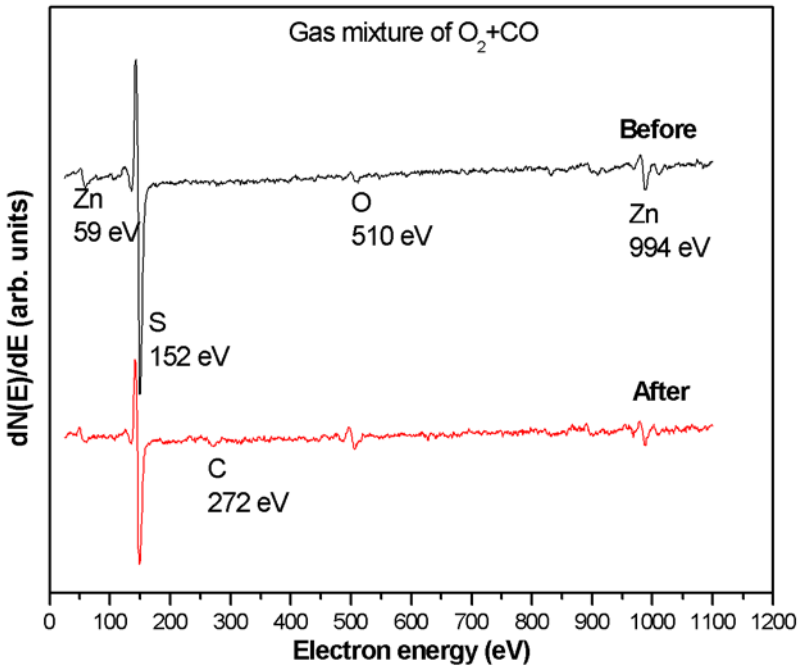

Figure 4.25: AES spectra of the surface sputter-cleaned P22G phosphor measured before and after the electron irradiation in the gas mixture of oxygen and carbon monoxide.

The P22G phosphor was also degraded in the argon ambient as shown in Figure 4.23. It is believed that the argon gas had no effect on the degradation due to its noble property. As indicated in the RGA spectrum (see Figure 4.24 (c)), there was some hydrogen gas present in the vacuum chamber. Sebastian *et al.* [48] showed that hydrogen caused the depletion of sulphur and proposed that volatile H_2S was formed during the electron irradiation. Therefore the degradation in the argon ambient should be due to the chemical reaction between hydrogen gas and the phosphor.

Chapter 5

Simulations

5.1 Comparison between experimental and simulation results

The Matlab source code for the simulation of the Monte Carlo electron trajectories and the quantification of the CL intensities [23] were used to simulate the electrons penetrating and losing energy in the ZnS bulk. By simulating various thicknesses of ZnO layer on top of the ZnS, the relative CL intensities were then quantified from the energy loss profiles. The details of these models and specific formulae are discussed in Section 2.3.

In Figure 5.1 the normalised CL intensity calculated as a function of the ZnO thickness is shown. The CL intensity decreases with an increase in the thickness of the ZnO and completely disappears when the ZnO layer increases to 65 nm with a 10 nm thick diffusion interface in between. Each data point in the figure represents one simulation that was performed using 1000 electron trajectories at the beam energy of 2 keV. For this simulation, the diffusion interface was set as non-luminescent. A distribution of incident angles was used to accommodate for the morphology of the phosphor powder. The calculated CL values were normalised with respect to the CL intensity calculated for an oxide free ZnS surface.

According to APPH profile shown in Figure 4.12, the CL intensity of the P22G phosphor was degraded to about 60% of the initial CL intensity when the phosphor was nearly 100% degraded (see Figure 4.10). The decrease in CL intensity to 60% of the initial intensity corresponds to a 8 nm thick ZnO layer with no diffusion interface, as indicated in Figure 5.1. From these results there is an apparent mismatch between the predicted and experimentally measured value of 2.76 nm given in Table 4.1. This suggests that more than just surface reactions are involved in the degradation process of the CL intensity. The excited electron responsible for the luminescent

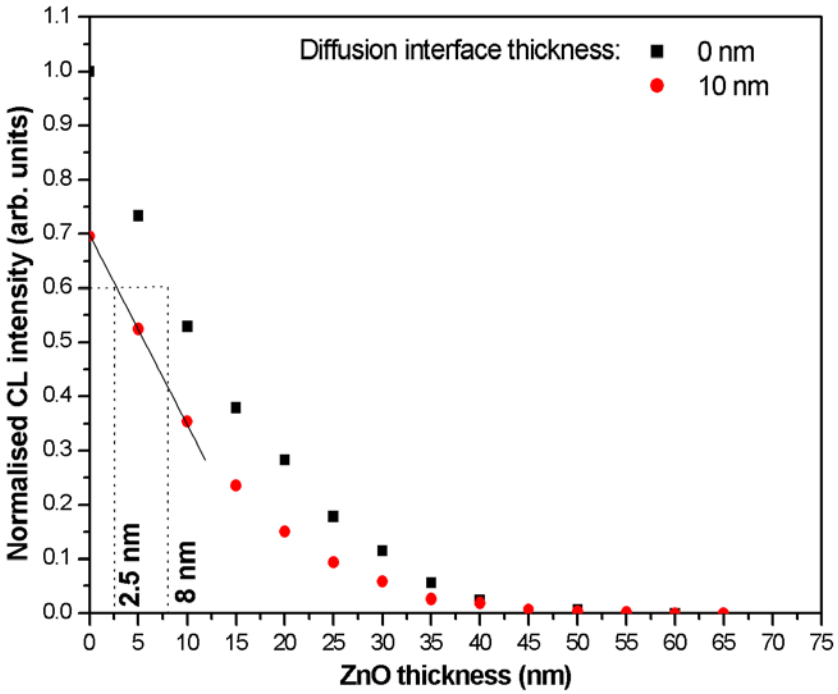

Figure 5.1: The normalised CL intensity as a function of the ZnO thickness calculated with a 10 nm thick diffusion interface between the ZnO layer and the ZnS bulk. The CL values are normalised with respect to the CL intensity for the oxide-free ZnS, having a 0 nm diffusion interface.

recombination in the P22G phosphor may travel many atomic distances before a recombination event takes place. Such energy transport is known to be sensitive to dislocations and vacancy or interstitial point defects, which may result from the electron bombardment, e.g. [48],

$$Zn + O \rightarrow ZnO + V_{Zn}. \qquad (5.1)$$

These defects may result in an increased probability of the radiationless recombination and consequently a decrease in the CL intensity. Non-stoichiometry near the interface would also disrupt the local crystal field around the luminescent centers in the phosphor, further reducing the optical emission. Hillie *et al.* [49] also demonstrated experimentally that oxygen atoms form iso-electronic impurities in the ZnS lattice during the electron beam bombardment in the oxygen ambient. The oxygen atoms have a higher electron affinity than the substituted sulphur atoms. The inclination to attract and trap excited electron responsible for the luminescent

recombination on these sites will increase. On the other hand the formation of a diffusion interface between two layers may lead to the dissociation of some of the ZnS and ZnO into their respective atomic species. Due to defects and the dissociation of ZnS at the interface, the diffusion interface may be totally non-luminescent. As indicated in Figure 5.1, the decrease in the CL intensity to 60% of the original intensity corresponds to a 2.5 nm thick ZnO layer with a 10 nm diffusion interface. The value compares well to the experimentally measured value of 2.76 nm.

Figure 5.2 shows the enlargement of the region of Figure 5.1 where the ZnO thickness is less than 5 nm. The trends in CL intensity due to the different widths of the diffusion interface are also shown. As indicated in Figure 4.12 and Table 4.1, a 20% degradation of the sulphur APPH corresponds to a decrease in CL intensity to 94% of the initial intensity due to a 1.01 nm oxide formation. Figure 5.2 shows this two values nearly intercept each other nearly at the curve of the 0 nm diffusion interface. This implies that the diffusion interface was narrow during the initial stages of the oxide formation. After a 40% degradation of the sulphur APPH, the phosphor was predicted to have a 2 nm thick diffusion interface. The thickness of the diffusion

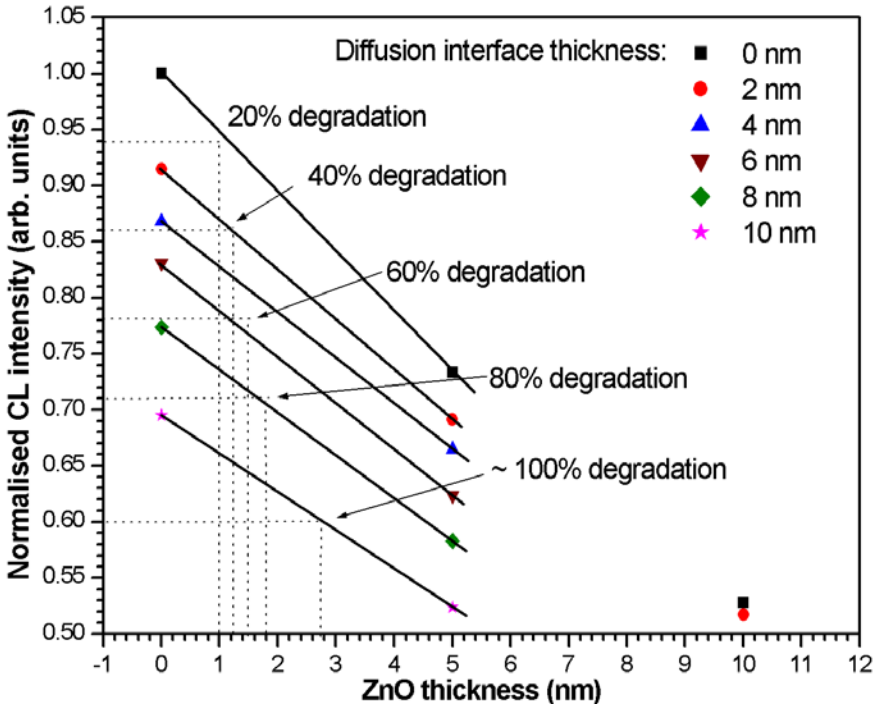

Figure 5.2: An enlargement of the region where the ZnO thickness is less than 5 nm in Figure 5.1. The trends of the different thickness for the diffusion interfaces are also

shown.

continued to spread out during the oxide formation. At 100% degradation of the sulphur APPH, the diffusion interface thickness was predicted to be about 10 nm thick.

As indicated in Figure 5.2, the thickness of the diffusion interface increased during the phosphor degradation. This implies that the diffusion process might be significant when the thickness of the oxide layer becomes thicker as in the case of the sulphate. By comparing the depth profiles in Figures 4.6 and 4.18, the sulphate has a much wider diffusion interface than the oxide.

In Figure 5.3 the normalised CL intensity as a function of the ZnO thickness calculated at 2 keV electron beam energy is compared to other energy values. The CL intensity is normalised with respect to the highest CL intensity of the 5 keV electron

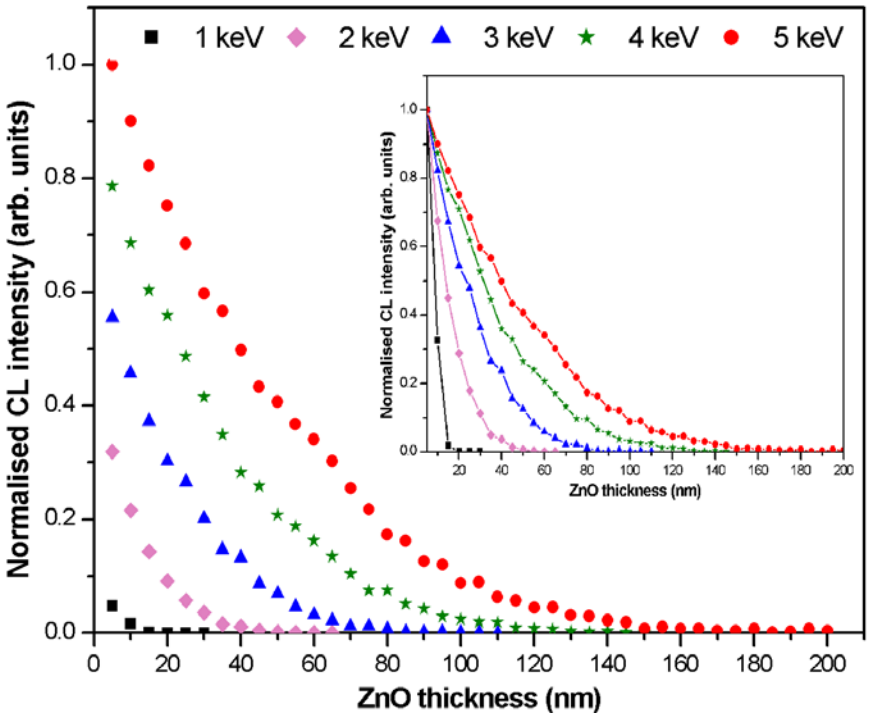

Figure 5.3: CL simulations for 1000 electron histories as a function of the ZnO thickness at different electron beam energies. A 10 nm non-luminescent diffusion interface between was present the ZnO and ZnS bulk. A distribution of the incident electron beam angles was used to simulate each incident angle of the electrons. The CL intensity is normalised with respect to the highest value in the trend of the 5 keV electron energy. In the inset the CL intensity for each electron beam energy is

normalised with respect to its highest value.

energy trend. As indicated in the figure, the non-luminescent ZnO layer on the ZnS phosphor powder has less effect on the luminescence for the higher energy electron beam. This is because the high energy electron beam has a deeper penetration depth and therefore a larger fraction of the energy can be deposited into the ZnS bulk to produce photons. The CRT displays use a typical beam energy of 15-30 keV but FEDs only use around 0.5-6 keV. That is why the surface condition of the phosphor in FED environment is critical, as opposed to CRTs that do not have the difficulty with the oxide layer.

The inset in Figure 5.3 shows the normalised CL intensity for each electron beam energy. It is normalised with respect to the highest CL intensity value. These results agree very well to the experimental results reported by Swart *et al.* [45]. They showed that the CL intensity of the P22G phosphor powder decreased slowly with an increase in the electron beam energy.

The maximum penetrating depth of the electron beam into the ZnO for the specific beam energy is also predicted from Figure 5.3. The maximum penetration is defined as the depth at which the CL intensity is completely diminished. The values are summarised in Table 5.1. Figure 5.4 shows the approximate depth of the interaction volume in the ZnO as a function of incident electron beam energy. The electron range was calculated using the Kanaya-Okayama range equation [50]:

$$R_{KO} = \frac{27.6AE_0^{1.67}}{Z^{0.89}\rho} \quad \text{(nm)} \qquad (5.2)$$

Electron beam energy (keV)	1	2	3	4	5
Maximum penetrating depth (nm)	15	45	90	145	170
Kanaya-Okayama range (nm)	15	45	90	150	215

Table 5.1: A summary of the predicted electron maximum penetrating depth and Kanaya-Okayama electron range in the ZnO for a given electron beam energy.

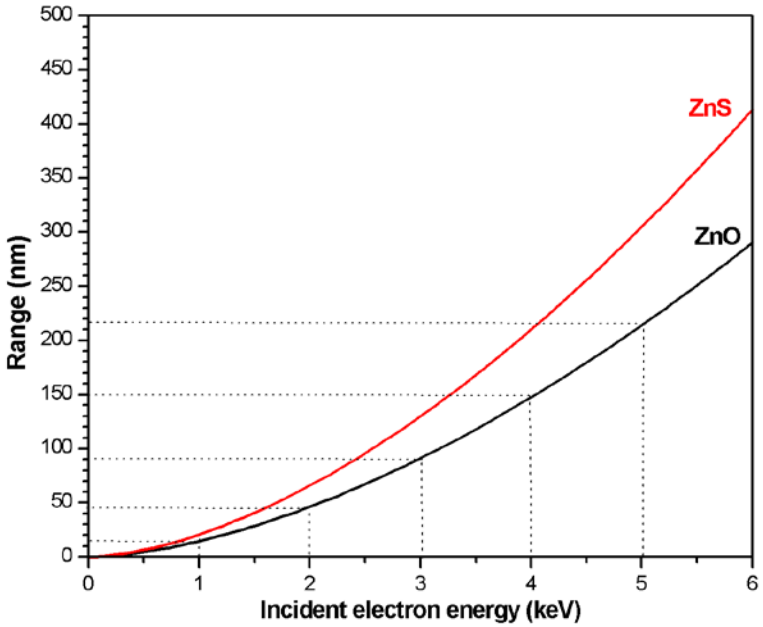

Figure 5.4: The Kanaya-Okayama electron range in the ZnO and ZnS as a function of electron beam energy.

where A is the atomic weight (48.72 g/mol), E_0 is the incident beam energy in keV, Z is the atomic number (19) and ρ is the density of the ZnO (5.61 g/cm^3). The average atomic weight and number of the zinc and oxygen were used for the calculations. The electron ranges in the ZnO for the specific beam energy are also summarised in Table 4.1. The Kanaya-Okayama ranges are comparative to the simulation results, especially in the case of the lower beam energies. The electron range in the ZnS as a function of incident beam energy is also shown in Figure 5.4. As shown in the figure, the electrons have shorter ranges in the ZnO than in the ZnS for a specific electron beam energy.

5.2 CL simulation with different electron incident angles

The second set of simulations was performed to see the effect of the electron beam's incident angle on the CL intensity of the phosphor powder. A total of 1000 electron trajectories were simulated for the ZnO/ZnS system. The electron beam energy was again set to 2 keV. The diffusion interface between the ZnO and ZnS was set to be 10 nm thick. Figure 5.5 shows the normalised CL intensity as a function of the ZnO

thickness, calculated at different incident angles of the electron beam.

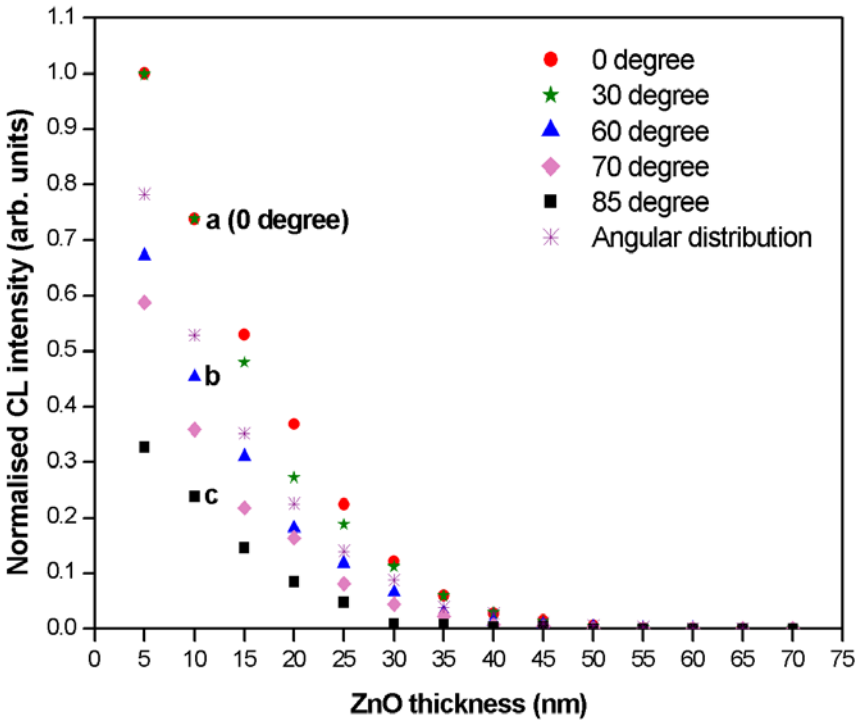

Figure 5.5: CL simulations of 1000 electron histories as a function of the ZnO thickness at 2 keV electron beam energy and different beam incident angles. A 10 nm thick diffusion interface was simulated between the ZnO layer and ZnS bulk.

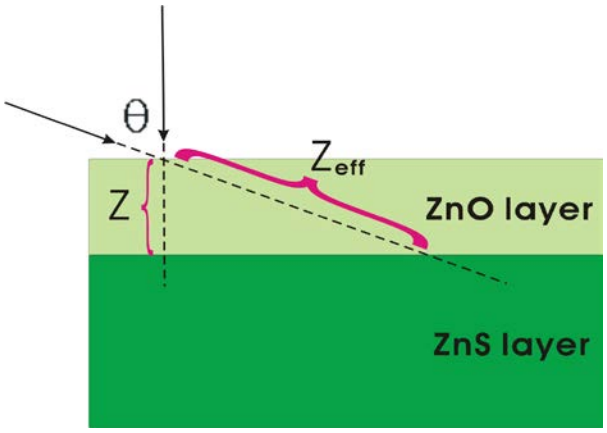

Figure 5.6: A large incident angle of the electron beam causes an increase in the effective thickness of ZnO layer in the thin film. More energy is therefore lost in the ZnO layer, which decreases the CL intensity generated in the bulk.

From the simulation result, the ZnS phosphor has the highest CL intensity generated by an electron beam having a 0° incident angle. The CL intensity decreases gradually from small to large incident angles for a specific ZnO thickness. The decrease in CL intensity was more pronounced at larger incident angles. As indicated in Figure 5.6, the effective thickness (Z_{eff}) of the ZnO layer on the ZnS bulk varies with the incident angle (θ) of the electron beam.

The electron energy loss profiles of point a, b and c in Figure 5.5 illustrates this effect in Figures 5.7 (a)-(c). The electrons having a 0° incident angle lost less energy in the shallow layers with a large fraction of the energy deposited into the ZnS bulk with the consequently higher CL generation as illustrated in Figure 5.7 (a). The energy loss increased along the depth and decreased after a maximum. At a 60° incident angle (Figure 5.7 (b)) a large fraction of electron energy was lost in the ZnO layer due to an increase in the effective thickness of the ZnO layer. Figure 5.7 (c) shows that the electron energy loss profile of which an electron beam has an incident angle of 85°. In this situation the electrons have to travel a wide effective ZnO thickness and therefore

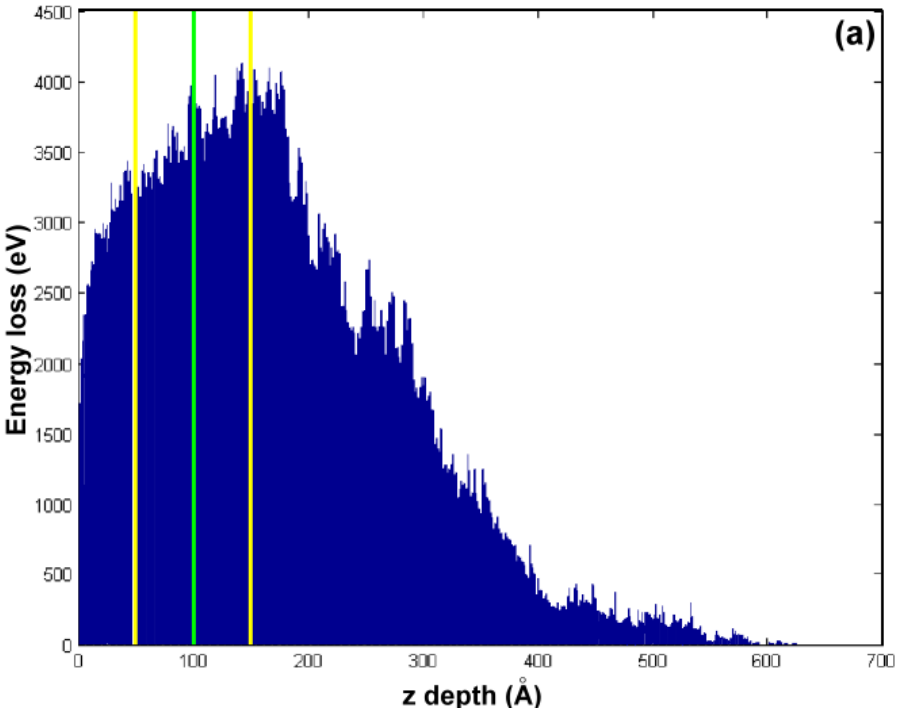

Figure 5.7: The electron energy loss profiles of the electron trajectory simulation with (a) a 0° incident angle.

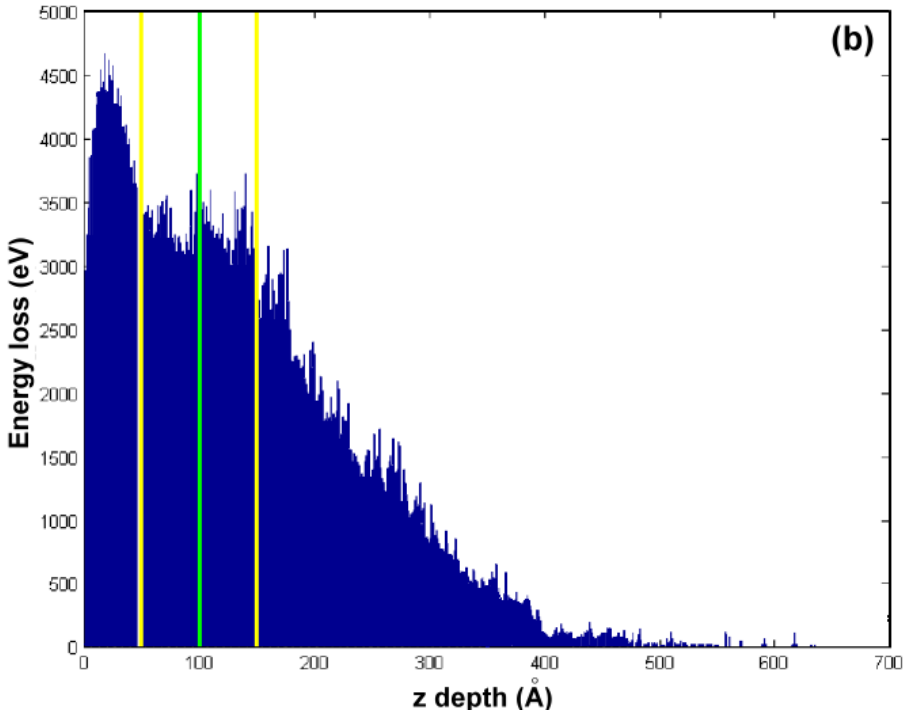

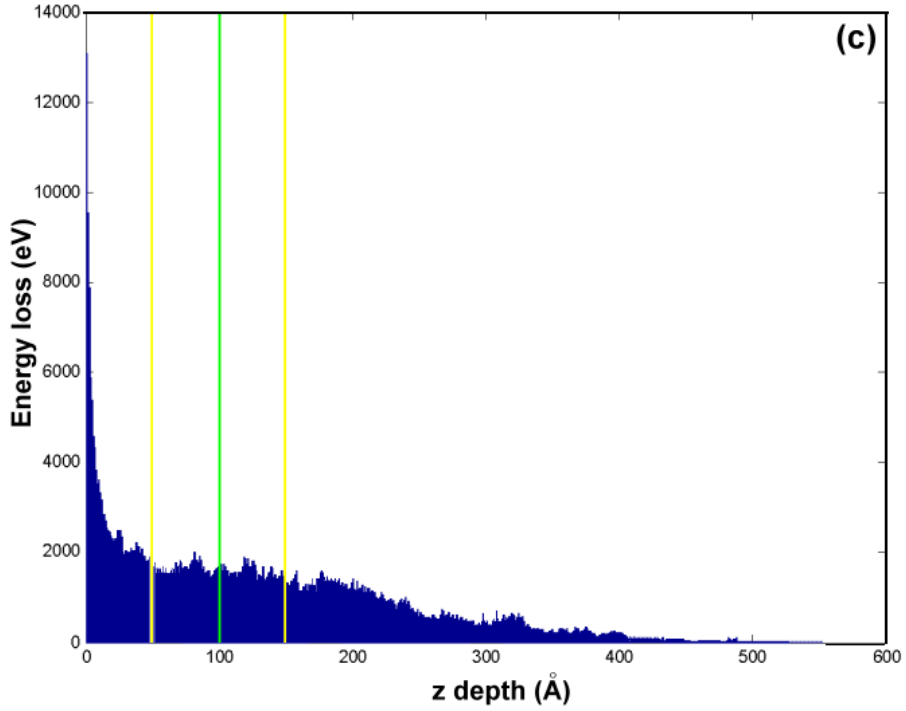

Figure 5.7: The electron energy loss profiles of the electron trajectory simulation with (b) a 60° and (c) 85° incident angle.

lose a considerable amount of the energy in the ZnO layer. Consequently a low CL intensity is generated in the ZnS phosphor due to the decreased energy deposition in the bulk.

The CL intensity generated by the 2 keV electrons, with incident angles according to an angular distribution, was also plotted as a function of the ZnO thickness in Figure 5.5. The CL trend is situated between the trends for the 30° and the 60° incident angle. This is due to the average incident angle of 45° for the angular distribution [24]. From the simulation considerations the use of a thin film ZnS phosphor is preferable to the current powder form, since normal incidence angles can be used to minimise the effect of the ZnO layer on the CL intensity at similar electron beam energies.

Chapter 6

Conclusion and future work

When ZnS:Cu,Al,Au (P22G) phosphor powder was exposed to an electron beam, the surface of the phosphor was converted to a layer of non-luminescent material with a consequent loss of the CL intensity. The formation of this non-luminescent layer was due to the electron stimulated reaction between the ZnS phosphor and the residual gases (e.g. oxygen, carbon monoxide and carbon dioxide) in the sealed vacuum.

During degradation of the P22G phosphor in the water-rich oxygen ambient, the non-luminescent layer was found to be ZnO. The formation of the ZnO layer was a chemically-limited reaction. CL intensity generated from P22G phosphor with a carbon free surface decreased linearly with the thickness of the oxide layer. The experimentally measured ZnO thickness was comparable to the calculated value of the Monte Carlo electron trajectory simulation. From simulation results, the effect of the ZnO layer on the CL was minimised by using a high accelerating energy electron beam with a smaller incident angle.

On the other hand, the electron beam exposure on the P22G phosphor in a dry oxygen ambient formed a layer of $ZnSO_4$ on the surface. This formation of sulfate decayed exponentially with time. It was postulated that the diffusion of charged species was involved in the sulfate formation. A non-uniform charge distribution was therefore established in the phosphor. Consequently, the charged reactants diffused in the $ZnSO_4$/ZnS system according to their concentration differences with an additional retarding electrostatic force.

The amount of water vapour in the sealed vacuum affected the degradation rate of the P22G phosphor and even changed the type of the non-luminescent layer formed on the phosphor surface. It was found that argon and carbon monoxide gas can suppress the degradation of P22G phosphor during electron bombardment. Argon gas competed

with oxygen molecules to stay on the phosphor surface. The oxygen concentration on the surface was reduced and caused a slower chemical reaction rate. Carbon monoxide molecules near the phosphor surface were dissociated by the electron beam into their elemental atoms. This constant generation of carbon caused a protective layer of carbon on top of the ZnS bulk and slowed the degradation down.

The overall studies showed that the lifetime of phosphor powders in the FED environment can be extended by improving the vacuum condition of FEDs. The vacuum can be baked for few hours to minimise the effects of water vapour and filled with argon and carbon monoxide before sealing. The design of the field emission array should also make use of higher accelerating energies at smaller average incident angles. If possible, a thin phosphor film should be used rather than the conventional phosphor powder.

The following aspects, touched on in this study should be investigated further in order to support the postulations and to acquire more information about the degradation of the P22G phosphor:

1. The ZnO thickness formed on the surface of P22G phosphor grew linearly with time during electron bombardment in the water-rich oxygen ambient. The ZnO layer continued to grow on the phosphor surface even when the AES technique could not detect sulphur. It is believed that the diffusion of the reactants would start to play a role in the oxide formation when the oxide become thicker. The diffusion species could be charged particles, as in the case of the formation of the $ZnSO_4$.

2. A different values for the electron beam current density, beam energy and oxygen pressure might vary the parameters in Equation 4.6. More work should be done on the degradation of P22G phosphor in the dry oxygen ambient with different experimental parameters to test the postulate. The amount of water vapour in the chamber changed the degradation mechanism and the type of non-luminescent layer formed on the P22G phosphor surface, but both formation of ZnO and $ZnSO_4$ still have to be proven with XPS.

3. The $ZnSO_4$ was formed on the surface of the P22G phosphor during electron bombardment in the dry oxygen ambient. The result seems to be contradictory to the result reported by Itoh *et al* [19]. They reported a $ZnSO_4$ layer was found on the ZnS:Zn surface after the degradation in H_2O pressure of 5×10^{-5} Torr. Therefore the degradation of the P22G phosphor must be studied in a water ambient. The chemical state of the non-luminescent layer must also be confirmed by the XPS technique.

Appendix A

Determination of the electron beam current density and the ion sputtering rate

A.1 Determination of the electron beam current density

It is important to determine the current density of the electron beam because its magnitude influences the degradation rate of phosphor powders. A lower beam current density (<32 mA/cm^2) generates less heat on the phosphor surface and this lower surface temperature leads to the the gas molecules spending more time on the surface [41]. Therefore a higher concentration of adsorbed molecules on the phosphor surface results in a faster degradation rate of S APPH. Secondly the lower surface temperature leads to a lower conductivity of the phosphor [41]. When the temperature of the phosphor decreases, less valence electron have sufficient energy to be excited to the conduction band. The number of charge carriers decreases and the resulting conductivity of the phosphor regresses. The prolonged electron irradiation of the phosphor results in the negative charging on the surface. This causes a band bending as indicated in Figure A.1 [42]. The excited electrons in the conduction band near the depletion layer will experience a repulsive force and be swept apart before combining with holes, resulting in a faster degradation rate of the CL intensity.

In order for these results to be comparable to other results, the electron beam current density should be determined and the APPHs should be plotted against electron dose (C/cm^2), which is calculated by multiplying the degradation time with the electron beam current density. However, the actual electron beam size must first be calculated.

The electron beam size was determined by using a Faraday cup. The beam current was measured while moving the edge of the Faraday cup perpendicular to the electron beam. The beam current as a function of the distance moved by the edge of the

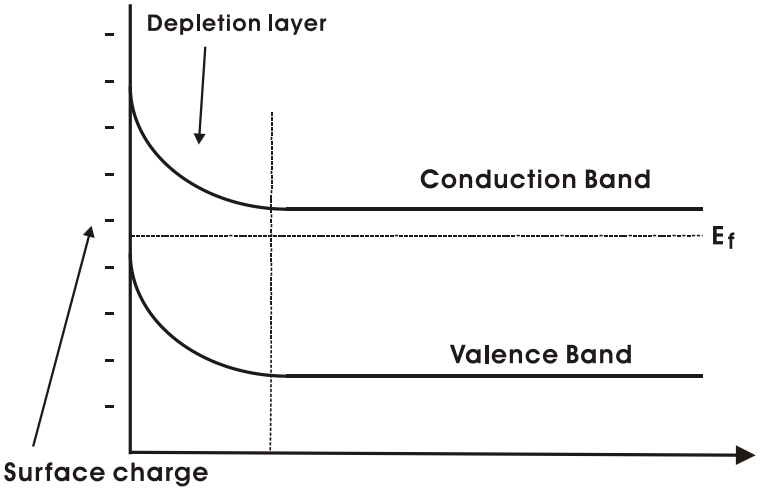

Figure A.1: The electron band diagram of a semiconductor whose surface is negatively charged.

Faraday cup (Figure A.2a) was differentiated and plotted (Figure A.2b). The diameter of the electron beam was taken as the width at the half-maximum (W) as shown in Figure A.2b. The diameter of the electron beam was 128 μm and the beam current density was therefore equal to 78mA/cm^2.

$$D_e = I_e / A_e \tag{A.1}$$

where D_e is the electron beam current density, I_e is the electron beam current maintained at 10 μA during the experiments and A_e is the beam area.

A.2 Determination of the ion sputtering rate

The ion gun was used to clean the surface of the phosphor and also to obtain depth profiles of the degraded phosphor during the experiments. The thickness of the oxide forming on the surface was then determined from the depth profiles.

An ion beam voltage of 2 keV and emission current of 1.5 mA were used during sputtering under a backfilled Ar pressure of 1.5×10^{-4} Pa. The ion beam was rastered over an area of 6 mm × 6 mm. The sputtering rate was determined by sputtering through a 400 Å ZnO thin film observing the above mentioned conditions. The ZnO thin film was pyrolytically deposited onto a clear float glass. The depth profile of the ZnO thin film is shown in Figure A.3 and the zinc APPH was smoothed by the

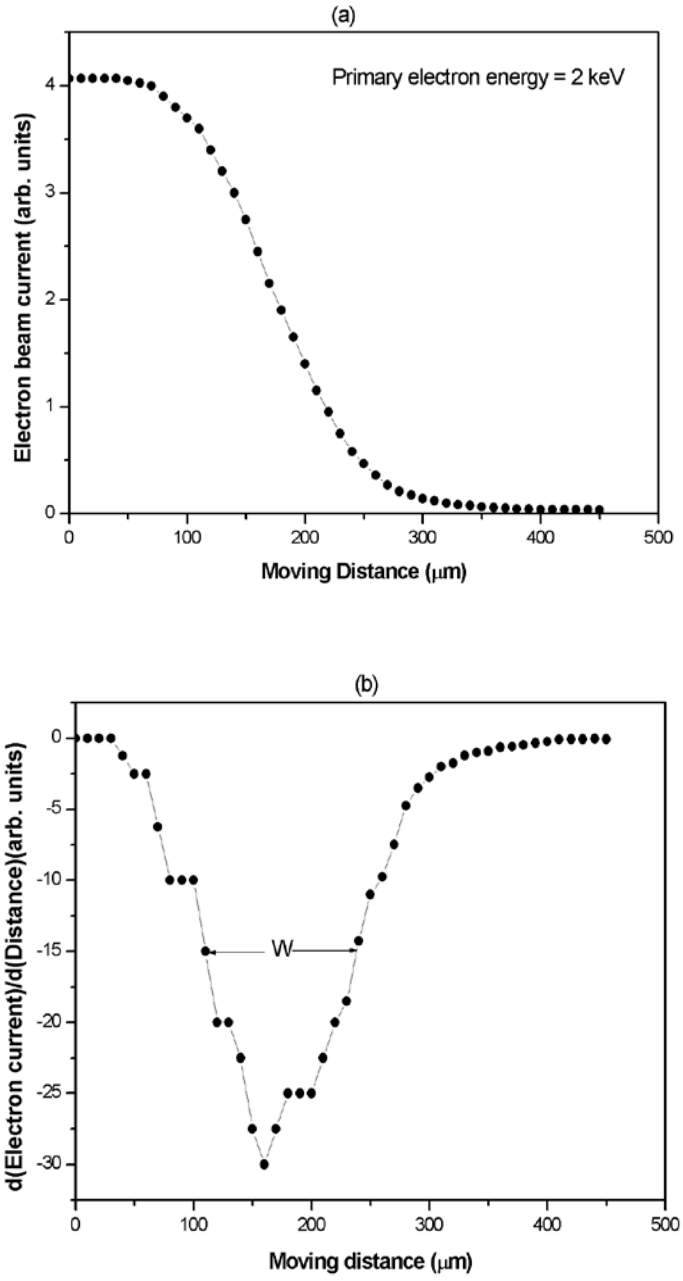

Figure A.2: The electron beam current (a) and the differentiated current (b) as a function of moving distance of the edge of the Faraday cup.

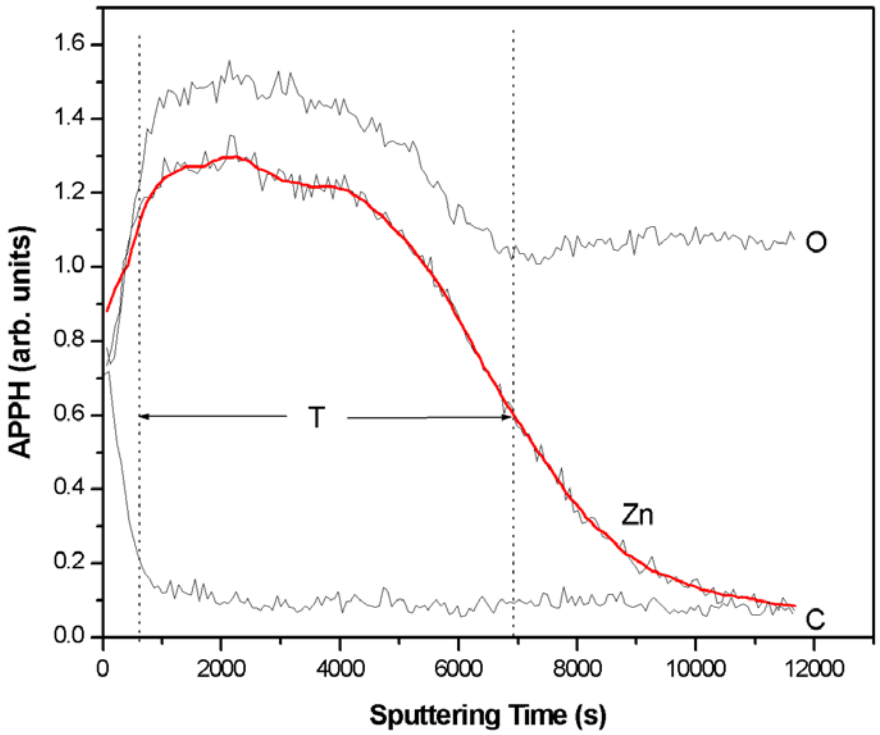

Figure A.3: The depth profile of the ZnO thin film with 400 Å thickness.

method called adjacent averaging. Each smoothed value (i) is the average of the data points in the interval [i-(n-1)/2, i+(n-1)/2] where n = 10 in this case.

As indicated in Figure A.3 carbon was present on the surface of the ZnO thin film from adventitious atmospheric contamination. The zinc and oxygen Auger peaks intensity increased initially as the carbon was removed from the surface. Both peak intensities decreased gradually after reaching the maximum. The sputtering time (T) through the ZnO was taken from the position where the zinc Auger peak intensity increased to 50% of the initial increase to the sputtered depth at which the zinc peak intensity decreased to 50% of the final decrease (see Figure A.3). The value of the sputtering time through the ZnO thin film was measured to be 6150 s and the sputtering rate was calculated as 3.9 Å/min.

$$Sputtering\ Rate = T_{ZnO} / t \qquad (A.2)$$

where T_{ZnO} is the thickness of the ZnO thin film (400 Å) and t is the sputtering time through the film.

Bibliography

[1] Industry Research and Statistics, Retrieved: November 2002, from http://www.semi.org/web/wsemi.nsf/url/0007wuirs.

[2] Cathode Ray Tube, Retrieved: March 2002, from http://whatis.techtarget.com/definition/0,,sid9_gci213839,00.html.

[3] Marshall Brain, How Television Works, Retrieved: March 2002, from http://www.howstuffworks.com/tv4.htm.

[4] What is TFT LCD, Retrieved: March 2002, from http://samsungelectronics.com/semiconductors/tft_lcd/technology/what_is_TFT/what_is_TFT.htm.

[5] Electroluminescence, Retrieved: March 2002, from http://www.planar.com/technology/el.asp.

[6] What is Flat Screen Plasma Technology, Retrieved: March 2002, from http://www.plasma-usa.com/about_plasma.html.

[7] Candescent Technologies Corporation, Retrieved: November 2002, from http://www.candescent.com http://www.candescent.com/Candescent/techprim.htm.

[8] FED, Retrieved: March 2002, from http://www.edtn.com/encyclopedia/search?term=FED.

[9] Advantages of Plasma Display, Retrieved: October 2002, from http://www.plasmapeople.com/plasma-advantages.asp.

[10] Ghis A, Meyer R, Rambaud P, Levy F, Leroux T. Sealed Vacuum devices: fluorescent microtip display. IEEE Trans Electron Dev 38 (1993) 2320.

[11] PixTech Inc., Retrieved: November 2002, from http://www.pixtech.com.

[12] Futaba, Retrieved: November 2002, from http://www.futaba-eu.com.

[13] Nanoata, Retrieved: October 2002, from http://www.nanosites.com/24nanotubesdisplay01.html.

[14] M. Ali Omar, *Elementary Solid State Physics*, (Addison Wesley Publishing Company, Inc., Philippines, 1975) p.266-268.

[15] H.C. Swart, J.S Sebastian, T.A. Trottier, S.L. Jones, P.H. Holloway, J. Vac. Sci. Technol. A 14 (1996) 1697.

[16] L. Oosthuizen, H.C. Swart, P.E. Viljoen, P.H. Holloway and G.L.P. Berning, Appl. Surf. Sci. 120 (1997) 9.

[17] P.H. Holloway, T.A. Trottier, J.S. Sebastian, S.L. Jones, X.-M. Zhang, J.-S. Bang, B. Abrams, W.J. Thomes and T.-J. Kim, J. Appl. Phys. 88 (2000) 483.
[18] B.L. Abrams, W.D. Roos, P.H. Holloway and H.C. Swart, Surf. Sci. 451 (2000) 174.
[19] S. Itoh, T. Kimizuka and T. Tanegawa, J. Electronchem. Soc. 136 (1989) 1819.
[20] M.I. Knotek, P.J. Feibelman, Surf. Sci. 90 (1979) 78.
[21] T.A. Trottier, H.C. Swart, S.L. Jones, J.S, Sebastian, P.H. Holloway, J. Soc. Inf. Disp. 4 (1996) 351.
[22] J.D. Kingsley, J.S. Prener, J. Appl. Phys. 43 (1972) 3073.
[23] A.P. Greeff, Ph.D. Thesis, University of the Free State, 2001.
[24] A.P. Greef and H.C. Swart, Surf. Int. Anal. 29 (2000) 807.
[25] F.W. Sears and G.L. Salinger, *Thermodynamics, Kinetic Theory, and Statistical Thermodynamics*, 3rd edition (Addison-Wesley Publishing Company, London, (1986) p.281.
[26] R. Shimizu and Z.-J. Ding, Rep. Prog. in Physics 55 (1992) 487.
[27] P. Hovington, D. Drouin, R. Gauvin, Scanning 19 (1997) 1.
[28] NIST Elastic Electron Scattering Cross Section Database, Standard Reference Data Program, Database 64. National Institute of Standards and Technology, Standard Reference Data Program, Gaithersburg (1996). www.nist.gov/srd/.
[29] R.H. Ritchie, F.W. Garber, M.Y. Nakai and R.D. Birkhoff 1969 Adv. Radiat. Biol. 3 1-28.
[30] D.C. Joy and S. Luo, Scaning 11 (1989)176.
[31] D.R Askeland, *The Science and Engineerig of Materials*, 3rd SI edition (Chapman and Hall, London, 1996) p.265, 643.
[32] P.G.T. Howell and A. Boyde, Scanning 20 (1998) 45.
[33] R. Browning, T. Eimori, E.P. Traut, B. Chui and F.W. Pease, J. Vac. Sci. Technol. B 9 (1991 p.135.
[34] M. Toth and M.R. Phillips, Scanning 20 (1998) 425.
[35] J.B. Steyn, P. Giles and D.B. Holt, J. Microsc. 107 (1976) 107.
[36] G. Pfefferkorn, W. Rocker and M.Hastenrath, Scan. Electron. Microsc. 251 (1980) 251.
[37] Operating Manual and User's Guide, S2000 Miniature Fiber Optic Spectrometers and Accessories, Ocean Optics, Inc.
[38] Ocean Optics Inc., Retrieved: November 2002, from http://www.oceanoptics.com.
[39] Osram Sylvania, Retrieved: November 2002, from http://www.sylvania.com.

[40] A.P. Greeff and H.C. Swart, Thin Solid Films 408 (2002) 206.

[41] K.T Hillie, Ph.D. Thesis, University of the Free State, 2001.
K.T. Hillie, H.C. Swart, Appl Surf. Sci. 183 (2001) 304.

[42] H.C Swart, A.P. Greeff, P.H Holloway, G.L.P. Berning, Appl. Surf. Sci. 140 (1999) 63.

[43] J.M. Walls, *Methods of surface analysis* (Cambridge University Press Publishing Company, 1989) p.13.

[44] H.C. Swart, T.A. Trottier, J.S. Sebastian, S.L. Jones, P.H. Holloway, J. Appl. Phys. 88 (1998) 4578.

[45] H.C. Swart, L. Oosthuizen, P.H. Holloway, G.L.P. Berning, Surf. Interface Anal. 26 (1998) 337.

[46] A.T. Fromhold, JR., *Theory of Metal Oxidation*, Volume II - Space Charge (North-Holland Publishing Company, 1980) p.68.

[47] Y. Darici, P.H. Holloway, J.S. Sebastian, T.A. Trottier, S.L. Jones, J. Rodriquez, J Vac. Sci. Technol. A 17(3) (1999) 692.

[48] J.S Sebastian, H.C. Swart, T.A. Trottier, S.L. Jones, P.H. Holloway, J. Vac. Sci. Thechnol. A 15(4), (1997) 2349.

[49] K.T. Hillie, H.C. Swart, Appl. Surf. Sci. 193 (2002) 77.

[50] J.I. Goldstein, A.D. Roming Jr, D.E. Newbury, C.E. Lyman, P. Echlin, C. Fiori, D.C. Joy, E. lifshin, *Scanning Electron Microscopy and X-Ray Microanalysis* (Plenum, New York, 1992).

Conference contributions

.

The results from this study has been presented at two local conferences.

1. S.H. Chen, A.P. Greeff, and H.C. Swart, *The effect of electron beam parameters on cathodoluminescence intensity during ZnS-based phosphor degradation: a Monte Carlo study*, South African Institute of Physics, Potchefstroom, South Afirca, 2002.
2. S.H. Chen, A.P. Greeff, and H.C. Swart, *Degradation behaviour of ZnS:Cu,Al,Au phosphor powder under different mixtures of gases*, South African Institute of Physics, Stellenbosch, South Africa, 2003.